Search for a Z' Boson in the Dimuon Channel in pp Collisions at $\sqrt{s} = 8$ TeV with the CMS Experiment at the LHC

by

Himali Kalakhety

Master of Science, Physics
Western Illinois University
Macomb, IL, USA
2007

A dissertation submitted to
Florida Institute of Technology
in partial fulfillment of the requirements
for the degree of

Doctor of Philosophy
in
Physics

Melbourne, Florida
December 2014

We, the undersigned committee, hereby recommend that the attached document be accepted as fulfilling in part the requirements for the degree of
Doctor of Philosophy in Physics.

"Search for a Z′ Boson in the Dimuon Channel in pp Collisions at $\sqrt{s} = 8$ TeV with the CMS Experiment at the LHC"
a dissertation by Himali Kalakhety

Marcus Hohlmann, Ph.D.
Associate Professor, Department of Physics and Space Sciences
Major Advisor

Debasis Mitra, Ph.D.
Professor, Department of Computer Sciences
External Committee Member

Hamid K. Rassoul, Ph.D.
Dean, College of Sciences
Professor, Department of Physics and Space Sciences
Committee Member

Samuel T. Durrance, Ph.D.
Professor, Department of Physics and Space Sciences
Committee Member

Francisco Yumiceva, Ph.D.
Assistant Professor, Department of Physics and Space Sciences
Committee Member

Abstract

Search for a Z′ Boson in the Dimuon Channel in pp Collisions at $\sqrt{s}$ = 8 TeV with the CMS Experiment at the LHC

by Himali Kalakhety

Dissertation Advisor: Marcus Hohlmann, Ph.D.

The Compact Muon Solenoid (CMS) experiment of the Large Hadron Collider (LHC) at the European Center for Nuclear Research (CERN) in Geneva, Switzerland has great physics potential in discovering many possible new particles beyond the standard model (SM) over a mass range around the TeV scale. Many extensions of the SM predict the existence of new heavy gauge bosons. Among these a simplest extension is the one that involves an additional U(1) gauge group with an associated neutral gauge boson, usually labeled as Z′. One of such extensions is called Sequential Standard Model (SSM) which includes a neutral gauge boson, Z'_{SSM} with the same couplings to quarks and leptons as the SM Z boson. Although this model is not gauge invariant but it has been traditionally considered by experiments studying high mass resonances. Other models, such as the superstring inspired E6 model, have a more complex gauge group structure with a corresponding neutral gauge boson denoted as Z'_{ψ}. In this dissertation, we report the results from the search of new heavy neutral gauge bosons, Z′, using pp collision data at center-of-mass energies $\sqrt{s} = 7$ TeV and 8 TeV collected with the CMS detector during the LHC Runs in 2011 and 2012 corresponding to an integrated luminosity of 5.3 fb^{-1} and 20.6 fb^{-1}, respectively. This dissertation describes a search for such a new heavy particles decaying into muon pairs. The search is performed by comparing the

reconstructed dimuon invariant mass spectrum to that of the SM expectations. Since no significant excess is found, we set upper limit on the ratio of the cross section times branching ratio for the decay of a new boson (Z') to the Z boson at the 95% confidence level (CL) using a Bayesian approach. For the dimoun channel, Z'_{SSM} can be excluded below 2.77 TeV and Z'_{ψ} below 2.43 TeV. This limit is combined with the limit obtained in the dielectron channel and used as a combined (dilepton) limit, so that Z'_{SSM} can be excluded below 2.96 TeV and Z'_{ψ} below 2.6 TeV and converted into lower limit on the masses of SSM Z' boson and E6 Z' boson.

The task of the Muon Endcap Alignment is to provide absolute positions of Cathode Strip Chambers (CSCs) in rϕ and Z coordinates of CMS. The Muon endcap hardware alignment system is designed to continuously monitor the actual positions of the CSCs relative to the tracking system. The Muon endcap alignment system is required to monitor chamber positions with 75-200 μm accuracy in rϕ, 400 μm in the radial direction and $\sim$1 mm in Z direction. In this dissertation, we also study the alignment performance for the rϕ coordinates in terms of resolution and precision achieved with full optical sensor systems.

Table of Contents

List of Figures

List of Tables

Acknowledgements

First and foremost, I would like to acknowledge my advisor and dissertation supervisor, Prof. Marcus Hohlmann, for his guidance and all possible support throughout my graduate study and research. Without his support, I would not be at my present position. I am very thankful to my dissertation committee members, Professors Hamid K. Rassoul; Samuel T. Durrance; Francisco Yumiceva and Debasis Mitra, for their comments and suggestions for this dissertation. My special thanks go to Prof. Marc Baarmand for his continuous support for the administrative work related to CERN.

I am thankful to my friends, Drs. Samir Guragain; Robert Michael Ralich; Kondo Gnanvo and Pramod Lamichhane, for their valuable suggestions and help throughout my research work. I would also like to acknowledge all of my CMS collaborators whose indirect support and help made this work possible. In particular, I would like to thank Drs. Oleg Prokofiev; James Bellinger; James Pivarski; Gervasio Gomez; Celso Rivero; Jordan Tucker; Slava Valuev; Adam Everett; Nick Kypreos; Alexander Lanyov; Gena Kukarstev and Steve Mrenna for their technical assistance and advice during the various stages of this work.

I would like to thank all the people in the Department of Physics at Western Illinois University, where I have completed my masters in physics. My special thanks go to Professors Vivian Incera; Mark Boley and James Rabchuk whose support, encouragement helped me to complete this work.

I would like to thank all the people in the Department of Physics and Space Sciences (PSS) at Florida Tech. My special thanks go to former department head, Dr. Terry Oswalt and Dr. Joseph Dwyer for always being supportive and helpful to the

graduate students. I would like to thank the Office of Graduate Programs for providing me an opportunity as an undergraduate lab teaching assistant. I am thankful to James Gering, director of undergraduate lab, for his guidance and support in the teaching lab. I am greatful to the PSS administrative staff, the late Irene Nash; Elaine Carlyle; Heather Talley and Leslie Smith for their support in all the administrative work.

I would like to remember Professors Lok Narayan Jha; Shekhar Gurung; Devi Dutta Paudyal; Kedar Lal Shrestha; Devendra Raj Mishra and Udaya Raj Khanal from Central Department of Physics (CDP), Tribhuwan University, Nepal and other Professors who taught me physics at my undergraduate level. I am thankful to my friends, Dr. Binil Aryal (Professor, Head, CDP) and Dr. Raju Khanal (Associate Professor, CDP) for their friendship, encouragement and best wishes during this research.

Last but not the least, I would like to thank my parents Ganesh and Mina, without whom I would not be here. I am greatly indebted to them who always took special interest in my education and encouraged me in all my career decisions. I am deeply grateful to my wonderful wife, Kabita, for her encouragement and support in every step of my life. Without her love, support and encouragement none of this would have been possible. I am proud of my son, Suyog, for being so good and cooperative during all the busy times of my work.

Dedication

This dissertation is specially dedicated to my parents Ganesh and Mina, wife Kabita, son Suyog and all the members of my family.

CHAPTER 1

Introduction

The goal of particle physics is to understand what the elementary particles are and how they interact with each other. The Standard Model (SM) of particle physics is a very successful model, which explains the structure of matter and forces acting between the fundamental particles. The SM has not only been confirmed in many precision measurements, but it has also been able to predict observations like the discovery of the W and Z boson at the LHC, and the top and bottom quarks at the Tevatron of the Fermi National Accelarator Laboratory (FNAL).

Although the SM successfully explains many of the elementary processes that we observe in nature, there are some predictions that still remain unconfirmed by experiments. The SM fails to explain phenomena such as gravity, dark matter, matter-antimatter asymmetry, neutrino masses and the number of quark/lepton families. These important shortcomings motivate particle physicists to develop theories and design experiments to explore physics beyond the standard model (BSM).

The SM is not the final theory of nature. Many BSM theories have been developed over the last century. Many have implemented the SM making it a part of a bigger picture. They are all consistent with experiments up to this date and the only way to support the theory is by exploring higher energy regimes. This is one of the main reasons why the LHC exists. It was built to explore new frontiers and to dig deeper into the

true nature of the universe. In some of the BSM theories, a new massive and electrically neutral gauge boson appears. Searching this boson is therefore, one way of exploring the physics beyond the SM. Z' properties vary greatly depending on what theory is used. Because of this, a model in experimental searches was developed as a method to compare results easliy. This Z' is known as the Sequential Standard Model (SSM) Z' and its search is the main theme of this dissertation.

This dissertation describes a search for a heavy electrically-neutral particle, which is produced in proton-proton (pp) collisions at the LHC and decays into two oppositely-charged muons. We select collision events resulting in muons because it decays too fast to be observed and the CMS detector can only record its decayed products. The invariant mass of the two muons corresponds to the mass of the new particle and its unique signature is a narrow resonance peak in the dimuon mass spectrum. The position of this peak depends on the mass of the new particle, its size on the production cross section and the branching ratio with which it decays into muons. A high mass dimuon resonance is not predicted by the SM, but by some of its extensions like the E6 model [1], which is one of the Grand Unified Theories (GUTs), which suggests that all fundamental forces except gravity are the same at very high energies. In this study, the search for a new theoretically-predicted gauge boson, Z', has been performed using the pp collision data collected with the CMS detector at $\sqrt{s} = 7$ TeV accumulated in the LHC runs in 2011 and in 2012 at 8 TeV.

This dissertation is organized as follows: Chapter 2 gives a brief overview of the SM and the electroweak theory. It also describes the theoretical framework for the search of Z' decaying to muons in the CMS experiment at the LHC. The physics motivation

behind the search of a Z' gauge boson decaying to muon pair final states is also presented. Chapter 3 gives a brief overview of the LHC and the various experiments conducted there. The main emphasis is given on the CMS detector as present work utilizes the data collected with it. A brief overview of various subdetectors of the CMS detector is also presented. Chapter 4 describes the muon endcap system and its alignment. It also decribes the alignment procedure to produce the alignment constants in rϕ plane used for the track reconstruction. Chapter 5 covers the analysis workflow for the search of $Z' \to \mu^+\mu^-$ using the data of LHC's 2011 run at $\sqrt{s}$=7 TeV, collected with the CMS detector. Chapter 6 describes the same search of Z' using the data of LHC's 2012 run at $\sqrt{s} = 8$ TeV. Chapter 7 describes the analysis of $t\bar{t}$ samples produced by the CMS Monte Carlo (MC) production for the 2012 run. It also describes the MC production of $t\bar{t}$ samples decaying to muons applying forced decay method using the Pythia MC generator and the results of the analysis. Chapter 8 summarizes the observations and experimental results of the analyses presented in this dissertation.

CHAPTER 2

Theoretical Overview

In this chapter, an overview of the SM and the properties of the fundamental particles and forces acting among them is presented. In order to understand observations not explained by the SM, many models have been suggested some of which predict a new heavy particle decaying into leptons. The physics and motivation for the search of a theoretically-predicted gauge boson, Z', decaying into a muon pair is presented. More information on the basic particle physics described in this chapter can be found in [2–4] and the review of the Z' phenomenology in [5–7].

2.1 Standard model of particle physics

The SM [2,3] of particle physics is the successful theory that describes the current understanding of fundamental particles and their interactions. Developed in the early 1970s, the SM has successfully explained most of the experimental results and precisely predicted wide varieties of phenomena. The foundation of SM is a quantum field theory, which describes the fundamental principles of quantum mechanics and special relativity. All matter is made up of elementary particles, the building blocks of matter. The fundamental particles are classified into fermions and bosons. Fermions have half-integer spin and make up all known matter in the universe. Each fermion has a corresponding

antiparticle, which has the same mass and spin as the opposite sign of all internal quantum numbers. The fermions are further classified into two basic types called quarks and leptons.

There are six quarks (up, down, charm, strange, top, bottom), and six leptons (electron, muon, tau, and their corresponding neutrinos), which are arranged in three generations. The first generation of leptons consists of the electron and the electron-neutrino, the muon and the muon-neutrino in the second, and the tau and the tau-neutrino in the third. Each of these leptons carry an electric charge and has a distinct mass. Each charged lepton has an associated neutral partner called neutrino which has no electric charge and possess a non-zero mass. The mass of the antileptons is identical to that of the leptons, but all of the other properties are reversed. Like the leptons, quarks are also divided into three generations. The up and down quarks are in the first generation of quarks, the charm and strange quarks are in the second and the top and bottom quarks are in the third. The most significant difference between generations of leptons and quarks is their mass. Figure 2.1 [8] shows the three generations of quarks and leptons and the force mediators with their mass and electric charge. Table 2.1 summarizes the three generation of fermions with their charge and mass.

There are four known fundamental interactions in the universe: the strong, the weak, the electromagnetic and the gravitational. These interactions are characterized on the basis of following criteria: the types of particles that experience the force, the relative strength, the range over which the force is effective, and the nature of particles that mediate the interaction. The fundamental interactions result from the exchange

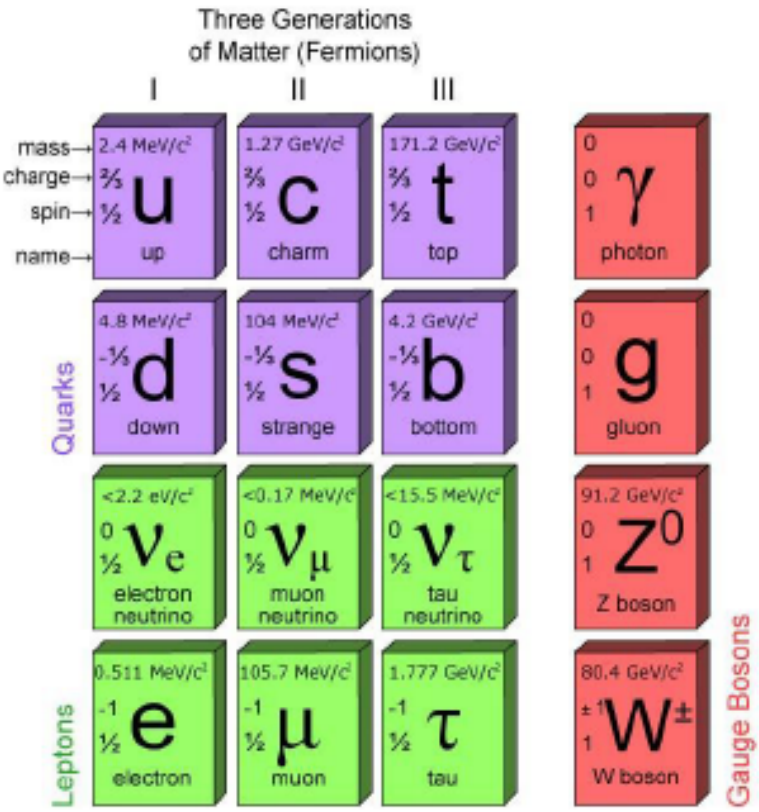

Figure 2.1: The standard model of elementary particles [8].

of particles called gauge bosons. So far, the quantum theory of gravitation is not formulated; therefore, the SM excludes gravity in its framework. An overview of all four fundamental interactions of the SM with increasing strength are summarized in Table 2.2, where the relative strength is normalized to unity for the strong force.

In the SM, gauge bosons are defined as force carriers. They mediate the strong, weak, and electromagnetic interactions. Photons, which are massless, mediate the electromagnetic force between electrically-charged particles. The photon and their interactions are described by quantum electrodynamics (QED). The $W^{\pm}$ and Z bosons mediate the weak interactions between particles of different flavors (all quarks and leptons) and

Generations	Name	Symbol	Antiparticle	Charge(e)	Mass(GeV)
I	up quark	u	$\bar{u}$	2/3	2.4×10^{-3}
	down quark	d	$\bar{d}$	-1/3	4.8×10^{-3}
	electron	e^-	e^+	-1	0.51×10^{-3}
	electron neutrino	ν_e	$\bar{\nu_e}$	0	$< 2.2 \times 10^{-9}$
II	charm quark	c	$\bar{c}$	2/3	1.27
	strange quark	s	$\bar{s}$	-1/3	0.104
	muon	μ^-	μ^+	-1	0.105
	muon neutrino	ν_μ	$\bar{\nu_\mu}$	0	$< 0.17 \times 10^{-3}$
III	top	t	$\bar{t}$	2/3	171.2
	bottom	b	$\bar{b}$	-1/3	4.2
	tau	τ^-	τ^+	-1	1.7776
	tau neutrino	ν_τ	$\bar{\nu_\tau}$	0	$< 15.5 \times 10^{-3}$

Table 2.1: Fundamental fermions of the standard model, spin $\frac{1}{2}$ particles.

Interaction	Strength	Range	Mediator	Acts On
Gravitational	10^{-39}	∞	Graviton	Mass
Weak	10^{-5}	10^{-18}	W, Z	Leptons, Hadrons
Electromagnetic	10^{-2}	∞	Photon	Electric Charges
Strong	1	10^{-15}	Gluon	Hadrons

Table 2.2: Fundamental interactions of the standard model.

are massive. The gluons mediate the strong interactions between the quarks and are massless. The gluons and their interactions are described by quantum chromodynamics (QCD). All fundamental SM bosons are listed in Table 2.3.

Interaction	Name	Symbol	Charge(e)	Mass (GeV)
Weak	Z Boson	Z^0	0	91.2
Weak	W Boson	$W^\pm$	± 1	80.4
Electromangnetic	Photon	γ	0	0
Strong	Gluon	g	0	0

Table 2.3: Fundamental bosons of the standard model, spin 1 particles.

The quarks carry fractional electrical charges ($\frac{2}{3}$,-$\frac{1}{3}$) and half integral ($\frac{1}{2}$) spin quantum numbers. The combination of the quarks produce a particle called hadrons. The quark and antiquark ($q\bar{q}$) combination produce a particle known as mesons. Mesons

have an integral spin and are bosons. A combination of three quarks (qqq) produce a particle known as baryons. There are three color charges: blue (B), red (R) and green (G). The quarks carry one of these colors and antiquarks carry the corresponding anti-colors: anti-blue($\bar{\mathrm{B}}$), anti-red ($\bar{\mathrm{R}}$) and anti-green($\bar{\mathrm{G}}$). Gluons also carry color and can interact with themselves. At large distances, the binding force strengthens as the color field becomes stressed and more and more gluons are spontaneously created. This is known as color confinement [9] and is the reason why quarks do not exist independently and grouped together to form hadrons. Experimentally, there is no color asymmetry and all observed particle states are colorless. The quarks form colorless states by combining into groups of baryons and mesons.

A gauge theory is a field theory in which the Lagrangian is invariant under local (gauge) transformations. Gauge theory explains the fundamental interactions. The transformations between possible gauges called gauge transformations form a group called symmetry group, or the gauge group. For each group, there is a corresponding vector field called the gauge field. The underlying symmetry group of the SM is $\mathrm{SU(3)_C \times SU(2)_L \times U(1)_Y}$. All these terms are gauge theories that couple fermions to the intermediate bosons. The gauge symmetries are related to the gauge bosons, the particles which mediate the fundamental interactions in the SM. The number of the mediator bosons for an interaction is determined by the symmetry group associated with it. The $\mathrm{SU(3)_C}$ symmetry group describes QCD, a theory of the strong interactions. It has eight generators called gluons which are massless and carry a color charge. The weak interaction is described in the form of SU(2) group with three gauge bosons ($\mathrm{W^{\pm}}$, Z). The electromagnetic interactions are described by a unitary group U(1) where interaction is

mediated by a massless particle photon; the corresponding theory is QED.

The Higgs boson is responsible for the electroweak symmetry breaking via the Higgs mechanism. The mechanism of the electroweak symmetry breaking causes the gauge groups $SU(2)_L \times U(1)_Y$ of the electroweak force to break into the electromagnetic and weak forces. The resulting group, $U(1)_{EM}$, controls the forces felt by the electromagnetic force. Photons mediate the electromagnetic force between electrically-charged particles, whereas other gauge bosons of $SU(2)_L \times U(1)_Y$ form the gauge bosons $W^{\pm}$, Z that govern the weak interaction.

Weak interaction takes place between all the known fermions. The large masses of the W and Z bosons account for the very short range of the weak interaction. It is called weak because of its field strength is far less than that of both the electromagnetic and the strong nuclear force. In the SM, the weak interaction is theorized as being caused by the exchange of the W and Z bosons and is considered a non-contact force like the other three forces. The well known example is β decay, where the weak interaction converts the neutron into a proton and electron by the emission of the W^- boson.

All charged particles undergo the electromagnetic (EM) interactions, mediated by the photons, which carry no electrical charge. Furthermore, the photons have zero mass. As a result, the EM force is effective over the long range extending to infinity. The EM coupling constant specifying the strength of the interaction between charged particles and the photons is given by the fine structure constant $\alpha \simeq \frac{1}{137}$ (in units of $\hbar = c = 1$). The EM interaction is controlled by the theory of QED and is responsible for holding the electrons and protons together inside the atom.

The strong interactions take place between the constituent quarks that make up

the hadrons and are described by the theory of QCD. The strong force acts between the particles carrying color charge (quarks). It is the strongest of all the four fundamental forces with a very short range of the order of 1 fm (10^{-15} m). All the quarks and gluons in QCD interact with each other through the strong force. The strength of the interaction is parameterized by the strong coupling constant. The strong coupling constant $\alpha_s \simeq 1$ (in units of $\hbar = \mathrm{c} = 1$), which is 100 times stronger than that of the EM coupling constant α. The strong interaction is observable in two scales. On a larger scale, about 1 to 3 fm, it is the force that binds the protons and neutrons (nucleons) together to form the nucleus of an atom. On the smaller scale, less than about 0.8 fm, the radius of a nucleon, it is the force (carried by gluons) that holds quarks together to form the protons, neutrons, and other hadron particles. Unlike all other forces (EM, weak, and gravitational), the strong force does not diminish in strength with the increasing distance.

The gravitational interaction is the weakest of all the four interactions and has an infinite range. This force is supposed to be mediated by a gauge boson called graviton which has not been experimentally observed yet. This force is extremely weak, having a relative strength of 10^{-39} with respect to the strong force at the atomic scale. It is a purely attractive force, which can travel even through the empty space to attract the two masses towards each other. This force is responsible for the attraction of objects towards the earth and elliptical motion of the planets around the sun.

2.2 The electroweak theory

The SM of particle physics describes the EM interaction and the weak interaction as two different aspects of a single interaction called the electroweak (EWK) interaction. The theory was developed by Sheldon Glashow, Abdus Salam and Steven Weinberg.

At very short distances, the strength of the weak interaction is comparable to that of the EM interaction. Glashow found a way to unify the EM and weak interactions [10]. He postulated that the EM and weak forces are manifestations of a single "electroweak force". The EM interaction is represented by the $U(1)_Y$ gauge group, with weak hypercharge Y, as the generator of the group. The weak interaction is described by the $SU(2)_L$ group, which is generated by the weak isospin I and interacting only with the left-handed particles as indicated by the subscript L.

Glashow's electroweak theory unifies the above two gauge groups into a single gauge group $SU(2)_L \times U(1)_Y$. The electroweak symmetry is well behaved above the electroweak scale where all the particles are predicted to be massless. Below this scale, some other mechanism is needed to give the weak gauge bosons mass, by breaking the $SU(2)_L \times U(1)_Y$ symmetry. This was achieved by incorporating the Higgs mechanism into Glashow's electroweak theory giving rise to what is known as the SM today. The spontaneous symmetry breaking by the Higgs mechanism, postulated by Steven Weinberg [11] and Abdus Salam [12] gives mass to the gauge bosons and all other massive particles in the SM.

The Higgs mechanism provides an explanation for the presence of three massive gauge bosons (the three carriers of the weak interaction) and the massless photon of the EM interaction. According to the electroweak theory, the universe has four massless gauge boson fields at very high energy similar to the photon and a complex scalar Higgs field doublet. However, gauge symmetry is spontaneously broken down to the U(1) symmetry of electromagnetism at low energies. This symmetry breaking would produce three massless bosons, but they become integrated by three photon like fields through

the Higgs mechanism, giving them mass. These three fields become the W^+, W^- and Z bosons of the weak interaction while the fourth gauge field, which remains massless, is the photon of the electromagnetism.

2.3 Motivation for Z′ search

The existence of additional gauge bosons beyond the ones associated with the SM gauge group remains an open question in particle physics. After the introduction of the unified electroweak theory described by the symmetry groups $SU(2)_L \times U(1)_Y$, theories containing additional symmetry groups were also proposed. Just like the Higgs mechanism that was introduced to account for the $SU(2)_L \times U(1)_Y$ symmetry breaking, it is possible to construct theoretical models by incorporating additional gauge fields that can lead to the new heavy gauge bosons. Although there are several ways in which new heavy gauge bosons can appear, the simplest one is the extension of the SM gauge structure in which the new heavy gauge bosons are simply the gauge field of a new local broken symmetry.

The simplest way of extending the SM gauge structure is to include an additional U(1) group. The underlying effective gauge group at low energies then becomes $SU(3)_C \times SU(2)_L \times U(1)_Y \times U(1)'$. This addition gives rise to an associated gauge boson, usually labeled as Z′, that is an electrically-neutral spin-1 particle. In most of the extended gauge theories, the symmetry breaking scale is at sufficiently high energies that the associated extra bosons are beyond the reach of current experiments. However, there exist several models that allow a relatively light Z′.

Regardless of the mechanism through which the Z′ is added to the SM, the particle itself is defined by two sets of parameters: the couplings to the SM particles and

the scale at which the $U(1)'$ symmetry is broken. The simplest example of Z' is known as the Sequential Standard Model Z' and written as Z'_{SSM}. In this model, the Z' has the same couplings as the SM Z and has a mass at the TeV scale.

2.4 Z' models

To overcome the shortcomings of the SM, several extensions have been proposed beyond the SM. In many of the BSM theories, new gauge bosons are postulated. The existence of heavy neutral bosons is a feature of many extensions of the SM. They arise in extended gauge theories including Grand Unified Theory (GUT), superstring theory, and Left-Right symmetric models and in other models of composite gauge bosons. The name given to these bosons are W' for electrically-charged and Z' for neutral ones. The most familiar models that predict the extra gauge boson are briefly explained below.

2.4.1 Grand unified theory

GUT [13, 14] is a general approach of extending the SM, which aim to unify the four fundamental forces. The basic idea is to find an extended symmetry group that naturally embeds the SM gauge group of symmetry $SU(3)_C \times SU(2)_L \times U(1)_Y$ as a low energy approximation. In GUTs, the strong and electroweak interactions are merged into a single interaction and they have a single coupling at a unification scale.

Two popular examples of GUTs originate from the groups SO(10) and E_6. The SO(10) contains an extra U(1) subgroup. SO(10) is decomposed in the subgroup as $SO(10) \rightarrow SU(5) \times U(1)_\chi$. Similarly, GUTs that originate from the E6 group decompose in terms of the chain $E_6 \rightarrow SO(10) \times U(1)_\psi \rightarrow SU(5) \times U(1)_\chi \times U(1)_\psi \rightarrow SM \times U(1)_{\theta E6}$

where $U(1)_{\theta E6}$ remains unbroken at low energies [1]. The corresponding neutral gauge bosons are denoted by Z'_{ψ}, Z'_{χ}.

2.4.2 Sequential Standard Model

Additional neutral gauge bosons are also predicted by the Sequential Standard Model (SSM), which serves as a standard model for experimentalists. The SSM is the simplest extension of the SM, which assumes that the Z' gauge boson has the same couplings as that of the SM Z gauge boson and decay only to the three known families of fermions. The new neutral gauge boson is assumed to be a heavy version of the SM Z gauge boson. This model is not a gauge invariant [1] and therefore, not a very realistic model, but it is a useful reference model. If a Z' gauge boson is created in the pp collisions at the LHC, it can decay into any of the known fermion antifermion pair.

The Z' search through the decay in lepton pairs is particularly interesting for experimentalists for several reasons. The study of high p_T leptons is a fundamental step to calibrate and align the detectors especially in lepton pairs from the Z resonance, which gives precious information to set up the detector (e.g. energy and momentum scales). The case of dimuon final state is particularly interesting for the CMS; muons are easily identified and their parameters can be measured with high precision given the robust and highly redundant tracking system. The muon identification and reconstruction algorithms involve all the CMS subdetectors; the interplay of the inner tracking system, the muon chambers and the calorimeters is fundamental in measuring the muon track parameters and the relative energy deposits.

The muon analysis is hence a fundamental step in understanding the detector

and in refining the commissioning. As a consequence, physics analysis involving muons is strategic in the period of the LHC collisions. As Tevatron is unable to find a signal for heavy neutral gauge boson Z', the LHC could be the option for its dicovery in a high mass significantly larger than 1 TeV/c^2. Experimentally, $Z' \to \mu^+\mu^-$ channel is one of the most promising for the discovery of Z' because it has a clean signature, low background and sizable branching ratio. It is also a good benchmark channel for muon detectors as it allows one to reconstruct high p_T muons, detector misalignment, etc.

With all the different Z' models available, two particular models are chosen as benchmarks: the SSM Z'_{SSM} [15, 16], which has the same coupling to quarks and leptons as the SM Z, but with arbitrary high mass; and the Z'_{ψ}, which corresponds to one of the U(1) from the E6 theory [17, 18].

2.5 Previous Z' searches

Experimentally, there are two ways of searching for the existence of a Z'. With hadron colliders, one usually performs direct searches, with the goal to produce an on-shell new particle. This is the idea behind the Z' search at the LHC. The new particle is produced many times and shows up in an invariant mass plot of its decay products. Indirect searches look for deviations from the SM that might be associated with the existence of a Z'. Due to the presence of extra gauge groups, a mixing between the SM Z and the Z' can occur. Changes in some of the measured values of the SM parameters and observables result from this Z - Z' mixing. We do not explore such Z - Z' mixing further in this dissertation. Direct searches rely on the explicit production of the Z' and are categorized in terms of the initial state, how a Z' is produced and the final state into which it decays. In e^+e^- colliders, the process for Z' production is $e^+e^- \to Z' \to \ell^+\ell^-$

(ℓ = e, μ) and for hadron colliders the Z′ production process is $pp \to Z' \to \ell^+\ell^-$ (ℓ = e, μ, τ). The common final states examined are those involving two oppositely-charged leptons such as dielectrons or dimuons. Other decay channels as dijet, $t\bar{t}$, $e\mu$, or $\tau^+\tau^-$ are also possible, but are experimentally less distinct.

Direct experimental limits are determined at hadron colliders by searching for resonances in the dielectron or the dimuon invariant mass spectra. The Tevatron collider at Fermilab was shut down in the fall of 2011. Until then it collided protons and antiprotons with $\sqrt{s} = 1.96$ TeV while the LHC data used in this analysis were produced by pp collisons at $\sqrt{s} = 7$ TeV and 8 TeV. Higher collision energies increase the accessible search region in the invariant mass spectrum allowing A Toroidal LHC Apparatus (ATLAS) and the CMS collaborations at the LHC to obtain mass limits higher than the Tevatron collaborations (CDF and D0) with only a fraction of the number of recorded collisions. The limits obtained by the ATLAS, the CMS, and the Tevatron collaborations for the Z'_{SSM} before the summer of 2011 were all of the order of 1 TeV [19–22], the highest being the limit by the CMS with 40 pb^{-1} of data, which excluded the Z'_{SSM} boson at the 95% CL for masses below 1.140 TeV [20]. The limits for the E6 Z′ bosons were also determined by several collaborations [19–21, 23].

CHAPTER 3

The Large Hadron Collider and Compact Muon Solenoid Experiment

This chapter introduces the LHC and one of its experiments, the CMS, located at the CERN. A brief description of various subdetectors of the CMS detector is given with an emphasis on the muon spectrometer.

3.1 Large Hadron Collider (LHC)

The LHC [24] is the world's largest and highest energy accelerator built at the CERN. Located about 100 meters underground in the former Large Electron Proton (LEP) collider tunnel spanning 27 km in circumference, The LHC is a circular machine built to recreate the conditions that existed just after the Big Bang and to probe new physics. It has been designed to collide proton beams at 14 TeV center-of-mass energy with a peak luminosity of $10^{34}\text{cm}^{-2}\text{s}^{-1}$, for the discovery of the Higgs boson and the physics beyond the SM. To study the quark-gluon plasma, it also collides lead ions at 2.76 TeV per nucleon at a peak luminosity of $10^{27}\text{cm}^{-2}\text{s}^{-1}$.

The LHC consists of eight arcs and two adjacent parallel beam pipes that intersect at four beam crossing points as shown in Figure 3.1. The two main detectors, the ATLAS and the CMS, are located at point 1 and 5 at the opposite side of the LHC ring. The other two detectors, A Large Ion Collider Experiment (ALICE) and the Large Hadron

Collider beauty (LHCb), are located at point 2 and 8. The LHC is a synchrotron machine that accelerates two counter rotating proton beams in the separate beam pipes. Protons are grouped into the ellipsoidal bunches to form a proton beam. Each proton beam is separated into 1.15×10^{11} protons per bunch with a bunch spacing of 25 ns. This corresponds to a collision frequency of 40 MHz. The design value for the number of bunches per beam is 2808. This corresponds to a design luminosity of $10^{34}\text{cm}^{-2}\text{s}^{-1}$. The LHC uses a large number of magnets for circulating the proton beams around the entire LHC ring. It comprises of 1232 superconductiong dipole magnets to keep proton beams in a circular trajectory and 392 quadrupole magnets to keep the beams focused. The superconducting dipole magnets are cooled with super fluid helium down to temperatures of 1.9 K, which makes the LHC the largest cryogenic facility in the world.

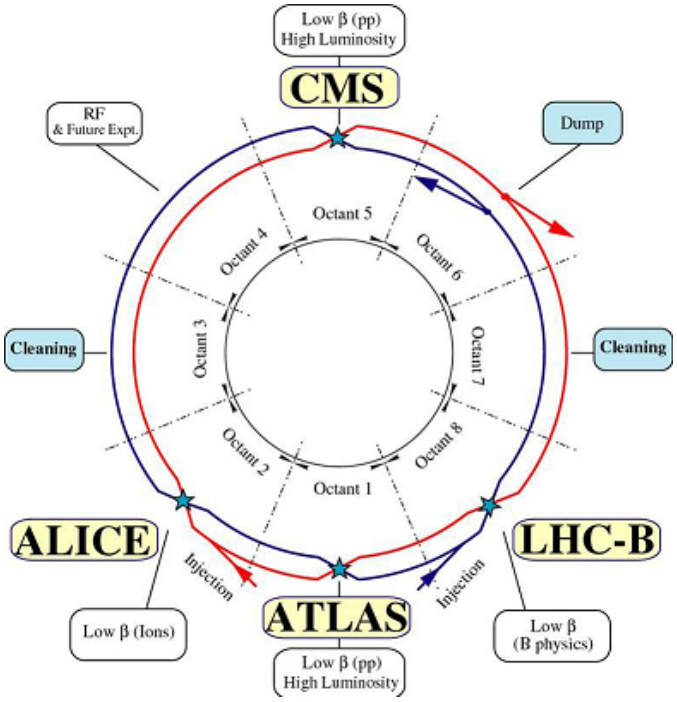

Figure 3.1: Schematic layout of the LHC [24].

3.1.1 LHC accelerator system

Before two proton beams collide in the LHC at the desired center-of-mass energy, the beams have to be accelerated by several steps. The accelerator complex at the CERN consists of a number of machines that accelerate particles to increasingly higher energies. A schematic view of the accelerator complex with the injection chain is shown in Figure 3.2. Each machine boosts the energy of a beam of particles before injecting the beam into the next machine in the sequence. In the LHC, particle beams, the last element in this chain are accelerated up to the record energy of 7 TeV per beam. Most of the other accelerators in the chain have their own experimental halls where beams are used for experiments at lower energies. The proton source is hydrogen gas. An electric field is used to strip hydrogen atoms of their electrons to yield protons.

The first accelerator in the chain is LINAC2, which accelerates the protons to the energy of 50 MeV. The beam is then injected into the Proton Synchrotron Booster (PSB) and accelerated to 1.4 GeV. Then the proton beams are accelerated up to 25 GeV in the Proton Synchotron (PS). Protons are then sent to the Super Proton Synchrotron (SPS) where they are accelerated to 450 GeV before they are injected into the LHC ring. Finally, the protons at 450 GeV are injected into the LHC where two proton beams reach their nominal energy of 7 TeV at full operation resulting in the collision at a center-of-mass energy, $\sqrt{s} = 14$ TeV. The collision energy is not yet at the nominal 14 TeV with the highest achieved being 7 TeV for the 2010 and 2011 runs and 8 TeV for the 2012 run.

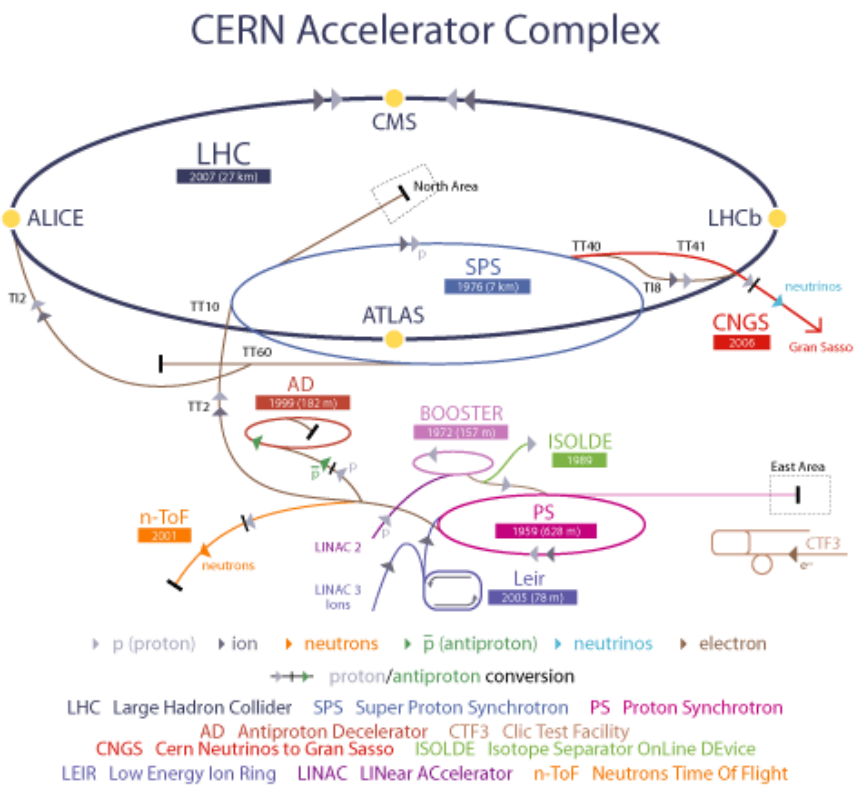

Figure 3.2: The LHC accelarator complex with its components [25].

3.1.2 LHC parameters

The LHC experiments aim at identifying interesting collisions at the different interaction points (IP) around the ring. Most of these events are very rare due to a very small production cross section, σ. The cross section is a measure for the probability to observe a desired interaction with respect to the all events generated by the accelerator. The event rate (R) for a certain process ($q\bar{q} \rightarrow \mathrm{Z}' + \mathrm{X} \rightarrow \ell^+\ell^- + \mathrm{X}$, where ℓ is either an electron or a muon) is proportional to the luminosity L,

$$\frac{dN}{dt} = R \quad = \sigma \, \mathrm{L} \tag{3.1}$$

where σ is the cross section of the physical process and L is the instantaneous luminosity of the collider. Integrating the above equation gives the expected number of events as $N = \sigma \int Ldt$, where $\int Ldt$ is instantaneous luminosity integrated over time and is known as the integrated luminosity, which is used to quantify the amount of data collected in the LHC. One of the most important parameters of the LHC or any such other accelerator is its capability of producing the expected or any new phenomena. This parameter is called the luminosity (L) and characterizes the number of collisions in a collider. Mathematically, luminosity can be expressed as:

$$L = \frac{f N_1 N_2 n_b \gamma F(\theta)}{4\pi \epsilon_n \beta^*} \tag{3.2}$$

where

- f is the frequency of interaction of the proton beams with each other.
- $N_{1,2}$ are the number of particles per bunch in two colliding beams.
- n_b is the number of bunches per beam.
- γ is the relativistic gamma factor.
- ϵ_n is the normalized transverse beam emittance.
- β^* is the beta function at the collision point.
- $F(\theta)$ is the factor accounting for reduction in luminosity due to the crossing angle $\theta = 285$ mrad of the two beams in the circular ring.

The nominal energy 7 TeV of each proton beam and the design luminosity of L $= 10^{34}\text{cm}^{-2}\text{s}^{-1}$ lead to around one billion pp interactions per second. The values for

some of the most significant parameters of the LHC are summarized in Table 3.1 where they are compared with the values used in 2012.

Parameter	Design	June 2012
Beam energy	7 TeV	4 TeV
Peak Luminosity	$10^{34}\text{cm}^{-2}\text{s}^{-1}$	$6.8 \times 10^{33}\text{cm}^{-2}\text{s}^{-1}$
Number of bunches	2808	1380
Number of particle per bunch	1.15×10^{11}	1.48×10^{11}
Bunch spacing (ns)	25	50
RMS bunch length	7.55 cm	$\geq$9 cm
Beam current	0.582 A	0.369 A
Luminosity/bunch	$3.6 \times 10^{30}\text{cm}^{-2}\text{s}^{-1}$	$1.1 \times 10^{30}\text{cm}^{-2}\text{s}^{-1}$
IP beam size	16.7 μm	19 μm
β^* at IP	0.55 mm	0.6 mm
Transverse Norm. Emmitance	3.75 μm	2.6 μm
Crossing angle at IP	285 μrad	290 μrad

Table 3.1: Actual parameters of the LHC in 2012 vs. design values.

3.1.3 Experiments at the LHC

There are four main experiments at the LHC. The experiments are located at points where the two beams of the LHC traveling in opposite directions collide head on. The two large experiments, ATLAS [26] and CMS [27] are general purpose detectors that are built to study both the pp and lead ion (Pb-Pb) collisions. The main goal of these two experiments is to search for the Higgs boson, to explore physics beyond the SM and to study the quark-gluon plasma. These detectors are located at the beam crossing point 1 and 5 in the LHC ring, respectively (Figure 3.1). These two independently designed detectors are vital for confirmation of any new discovery made.

The LHCb experiment [28] is especially designed to investigate the matter-antimatter asymmetry by studying the properties of the bottom quark. It is located at beam crossing point 8 (Figure 3.1). The ALICE detector [29] is a dedicated heavy

ion detector. It is built mainly to study the quark-gluon plasma, the hadronic matter in extreme temperature and density conditions, which probably existed just after the Big Bang when the universe was still extremely hot. The ALICE detector is located at beam crossing point 2 (Figure 3.1). The Total Elastic and diffractive cross section Measurement (TOTEM) [30] and Large Hadron Collider forward (LHCf) [31] experiments are especially designed to study the physics processes in the forward region, the region very close to the particle beam of pp or Pb-Pb collisions. The LHCf experiment was built close to the ATLAS experiment to explore the origin of the high energy cosmic rays, whereas the TOTEM experiment was built close to the CMS detector to precisely measure the pp interaction cross section and for an in-depth study of the proton structure.

3.1.4 LHC operation and performance in 2010-2012

For the first time on November 20, 2009, low energy proton beams (with 450 GeV energy per beam) circulated in the LHC tunnel. Soon after increasing the energy of the beam on November 30, the LHC became the world's highest energy particle accelerator achieving collisions with 1.18 TeV energy per beam. Later on March 30, 2010, the LHC broke its own record by colliding proton beams with 3.5 TeV energy per beam at a center-of-mass energy of 7 TeV. In 2011, the LHC resumed its operation on March 13, 2011, colliding proton beams similar to the 2010 run with 3.5 TeV energy per beam at a center-of-mass energy of 7 TeV. Figure 3.3 shows the first pp collision recorded by the CMS detector at center-of-mass energy of 7 TeV.

In 2012, the LHC collided proton beams at an increased center-of-mass energy of 8 TeV (with 4 TeV energy per beam) making new physics searches even more sensitive.

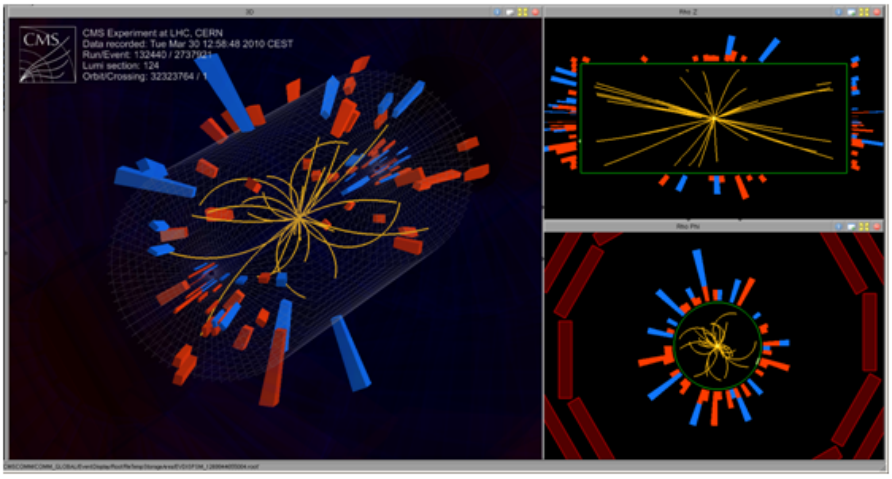

Figure 3.3: First collision recorded by the CMS at center-of-mass energy of 7 TeV. Yellow points represent hits in the central silicon tracker while red and blue bars represent the energy deposited in the hadronic and electromagnetic calorimeters, respectively [32].

The LHC has shown excellent performance during the years 2010 and 2011. On April 22, 2011, it set a new world record for the beam intensity at a hadron collider by colliding proton beams with a luminosity of $4.67 \times 10^{32}\text{cm}^{-2}\text{s}^{-1}$. This exceeds the previous world record of $4.024 \times 10^{32}\text{cm}^{-2}\text{s}^{-1}$ set by FNAL's Tevatron collider in the year 2010.

The instantaneous luminosity delivered depends on the LHC filling scheme, which corresponds to a specific mode of operation for the machine. A fill is characterized by many variants, the important one being the total number of proton bunches per beam, bunch spacing, and the expected number of colliding bunches at various interaction points. In 2010, the peak instantaneous luminosity reached $\text{L} = 2 \times 10^{32}\text{cm}^{-2}\text{s}^{-1}$ with 368 bunches per proton beam and accumulated about 40 pb^{-1} of collision data. In 2011, the LHC recorded a peak luminosity of $\text{L} = 3.5 \times 10^{33}\text{cm}^{-2}\text{s}^{-1}$, which is a ten-fold increase compared to that in 2010, with 1380 bunches of protons per beam. The data accumulated in 2011 is ~ 6 fb^{-1}, which is more than 100 times of what was accumulated in 2010. In 2012, with 8 TeV center-of-mass energy, it delivered ~ 23 fb^{-1} of data as

shown in Figure 3.4. Figure 3.5 shows the total integrated luminosity delivered by the LHC in the years 2010, 2011, and 2012. This analysis uses the full 2011 and 2012 pp collison data as recorded by the CMS experiment.

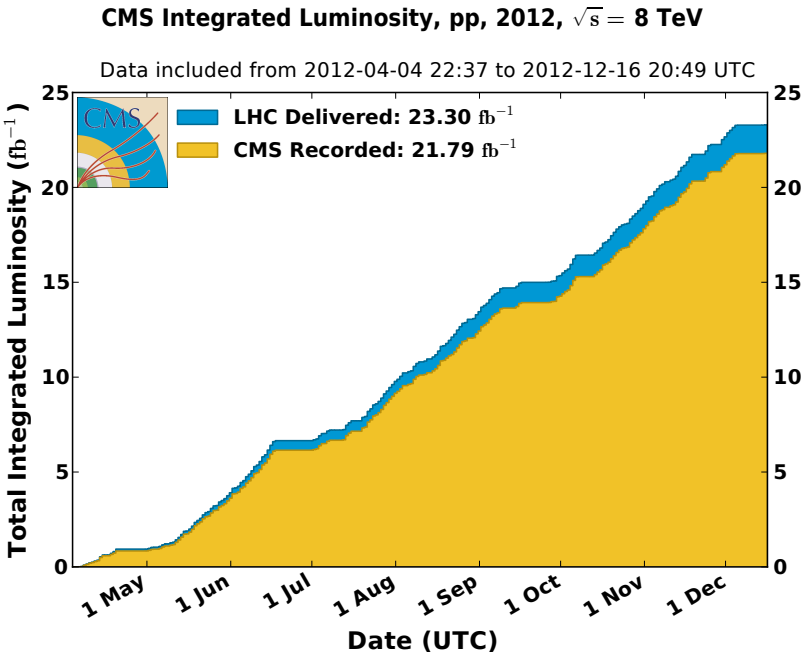

Figure 3.4: Total integrated luminosity delivered by the LHC in 2012 [33].

3.2 Compact Muon Solenoid (CMS) detector

The CMS [27, 34] detector is one of the two large general purpose detectors operated at the LHC capable of studying both the pp and heavy ion collsions. It is located 100 m underground at point 5 of the LHC. The main feature of the CMS detector is the superconducting solenoid, the largest solenoid ever built, which allows for an excellent momentum resolution of the reconstructed charged particles. The overall structure of the CMS consists of several cylindrical layers coaxial to the beam axis (the barrel layers), closed at both ends by detector disks orthogonal to the beam direction (the endcaps).

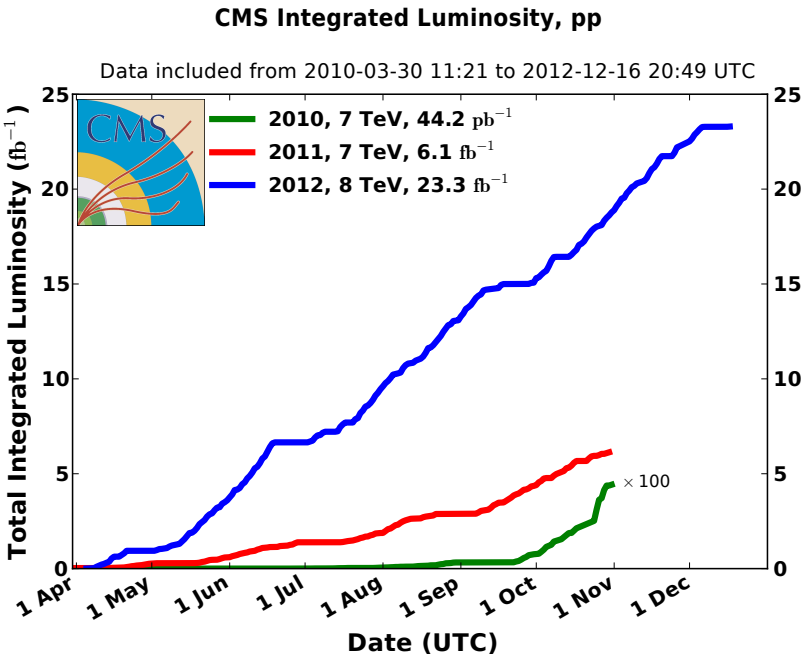

Figure 3.5: Total integrated luminosity delivered by the LHC in the years 2010, 2011, and 2012 [33].

The CMS detector is 21.6 m long with a diameter of 14.6 m and weighs 14500 tons. The 4 T superconducting magnet (13 m long and 6 m inner diameter) sits at the heart of the CMS detector providing a uniform magnetic field of 3.8 T during collsions. It is designed around the solenoidal magnet and is comprised of multiple subdetectors: a pixel detector, a silicon tracker, EM and hadronic calorimeters, and muon detectors. The bore of the magnet is large enough to accommodate both the inner tracker and the calorimeters inside it. The magnetic field is closed by iron return yoke comprising of five barrel wheels to cover the length of the solenoid and the two endcaps, one on each end, which are composed of three layers each. Figure 3.6 shows the overall layout of the CMS detector.

The CMS muon detectors are divided into two main sections: the CMS Barrel and the CMS Endcap Muon (EMU) system. The barrel muon detector is composed

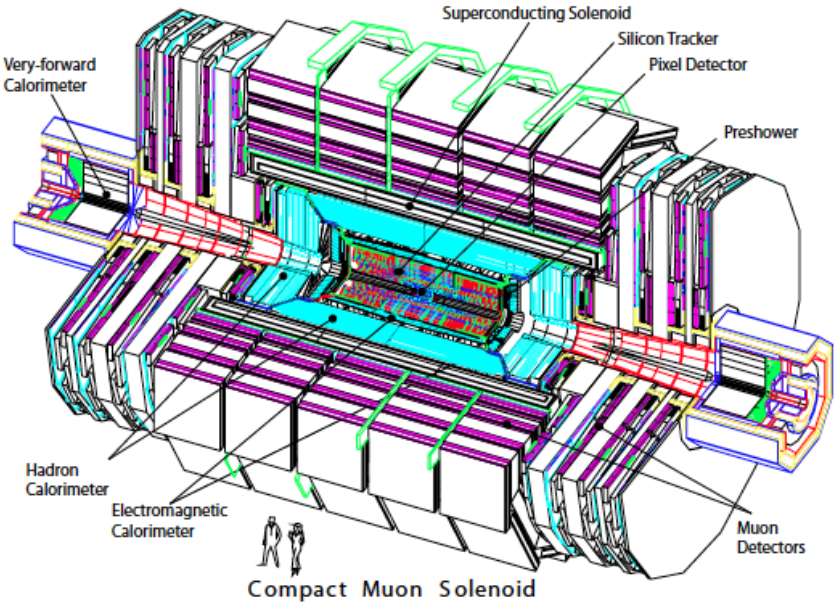

Figure 3.6: Schematic view of the CMS detector [24].

of Drift Tubes (DTs) while the EMU system is composed of Cathode Strip Chambers (CSCs), with Resistive Parallel Plate Chambers (RPCs) in both the barrel and endcap muon detectors. Each endcap is subdivided into four discs called stations, each denoted by MEn, where n refers to the station number. There are four stations, namely ME1, ME2, ME3 and ME4; similar stations on the other side are denoted by a negative sign. The detector layers are designed in such a way that exploit the different properties of particles and measure their energy or momentum. Because the muons can penetrate several meters of iron without interacting, they are not stopped by any of the CMS's calorimeters unlike most particles. Therefore, chambers to detect the muons are placed at the very edge of the experiment where they are the only particles likely to register a signal. Figure 3.7 below shows the whole CMS detector with its subdetectors.

The innermost layer closest to the interaction point is the silicon tracker, which

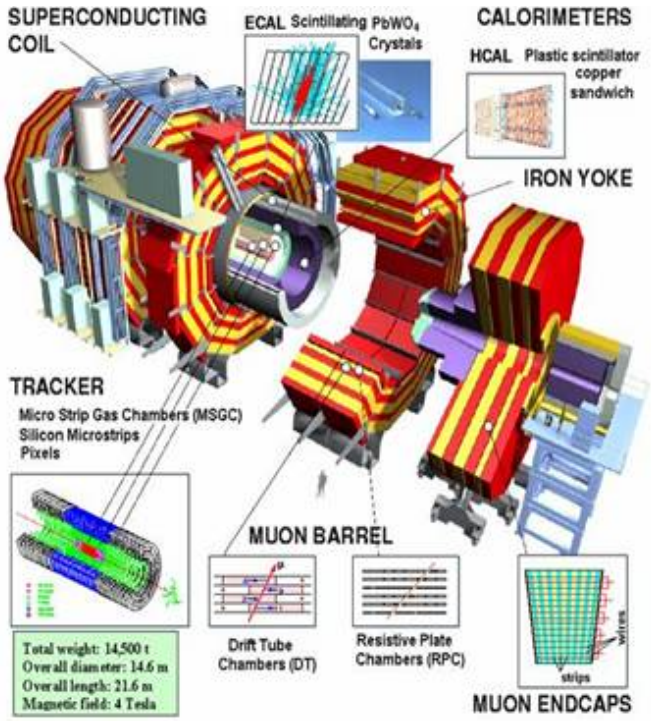

Figure 3.7: Schematic view of the CMS detector showing all the subdetector components [35].

is comprised of silicon pixel and strip detectors that identify charged particle tracks by recording their positions. The magnetic field bends charged particles allowing one to measure the charge and momentum of a particle based on the curvature of its tracks. The next layer of the detector, the EM calorimeter (ECAL), measures the energy of the electrons and photons with high precision. Surrounding the ECAL is the hadron calorimeter (HCAL), which measures the energy of the hadrons and also the missing transverse energy in an event.

The muon detectors, which form the final layer of the CMS detector are dedicated to identify particles that penetrate beyond the HCAL. In general, these are the muons and weakly interacting particles such as neutrinos. Since the muons are charged particles, their charge and momentum can be measured based on the curvature of their

tracks. However, neutrinos are neutral particles and hardly interact with the detector. Nevertheless, their presence can be inferred by adding up all the transverse momenta of the detected particles and assigning the missing transverse momentum to the neutrinos. As the name "Compact Muon Solenoid" suggests, detecting the muons is one of the CMS's most important tasks. We expect them to be produced in the decay of a number of potential new particles; for instance, one of the cleanest signatures of the Higgs boson is its decay into four muons. Figure 3.8 shows a transverse slice of the CMS detector, which demonstrates how different particles interact with the various layers of the detector leaving behind the characteristic patterns or signatures allowing them to be identified.

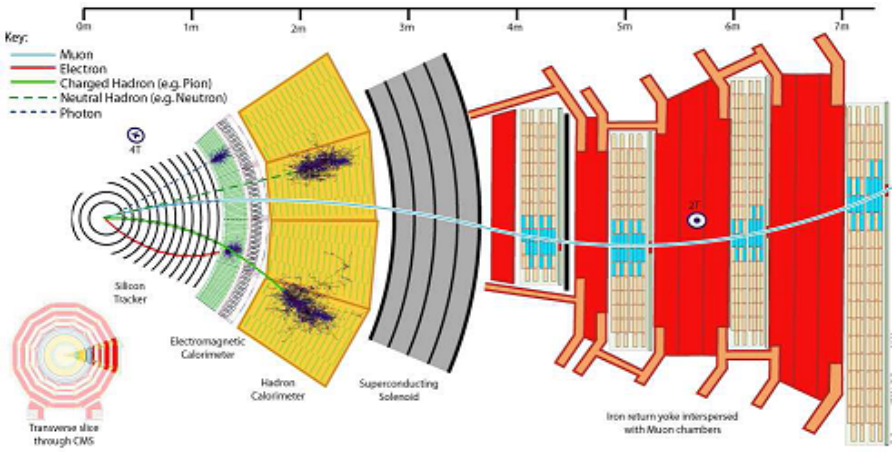

Figure 3.8: A transverse slice of the CMS detector showing the subdetectors and the path of the particles through it [36].

3.3 CMS coordinate system

The CMS uses a right-handed coordinate system with the origin at the nominal interaction point located in the center of the detector. The y-axis points upwards (perpendicular to the LHC plane), the x-axis points radially inward (towards the center of

the LHC). The z-axis points along the anticlockwise beam direction (towards the Jura Mountains from point 5). The polar angle θ is measured from the positive z-axis. θ ranges from 0 to π. $\theta = 0$ is + z-axis and $\theta = \pi$ is - z-axis. The azimuthal angle ϕ is measured from the x-axis in the xy plane. $\phi = 0$ is + x-axis and $\frac{\pi}{2}$ is + y-axis.

In experimental particle physics, rapidity (y) is commonly used to describe the geometrical coverage of the detector. In the relativistic limit, rapidity can be approximated by pseudorapidity (η). The rapidity is defined as:

$$y = \frac{1}{2} \ln \left(\frac{E + p_z}{E - p_z} \right) \tag{3.3}$$

where E is the relativistic energy of the particle and p_z is the particle's momentum along the beam direction (z-axis). η is a spatial coordinate describing the angle of a particle relative to the beam axis. It is defined as:

$$\eta = -\ln \left[\tan \left(\frac{\theta}{2} \right) \right] \tag{3.4}$$

where θ is the angle between the particle's momentum P and the beam axis. The momentum and energy measured transverse to the beam direction, are computed from the x and y components and are denoted by $p_T = psin\theta$ and $E_T = Esin\theta$ respectively.

3.4 Inner tracking system

The inner tracking system [34, 37, 38] of the CMS detector is designed to provide a precise and efficient measurement of the trajectories of the charged particles from the interaction point. The tracker is used to reconstruct the paths of high energy muons, electrons and charged hadrons. It is situated around the center of the detector inside

the solenoid and records hits from the passage of charged particles from which the tracks can be reconstructed. This provides an estimate of the particles charge, momenta and the production vertices. It surrounds the interaction point and has a length of 5.8 m with a diameter of 2.5 m. The CMS solenoid provides a homogeneous magnetic field of 3.8 T over the full volume of the tracker. The CMS tracker consists of about 200 m^2 of active silicon area making it the largest silicon tracker ever built.

The inner tracker is composed of silicon pixel and strip subdetectors, both laid out in a barrel plus endcaps arrangement with full coverage in ϕ and in $|\eta|$ up to 2.5. The pixels are closest to the interaction point, with the strips located just outside them. The inner tracker measures the transverse momentum (p_T) and provides the primary contribution to the momentum resolution for muons and for those with momenta up to a few hundred GeV. Using the tracks reconstructed by the inner tracker, primary vertices can be reconstructed in order to associate the tracks from the same pp interaction with each other. Figure 3.9. below shows the CMS tracker with all its components.

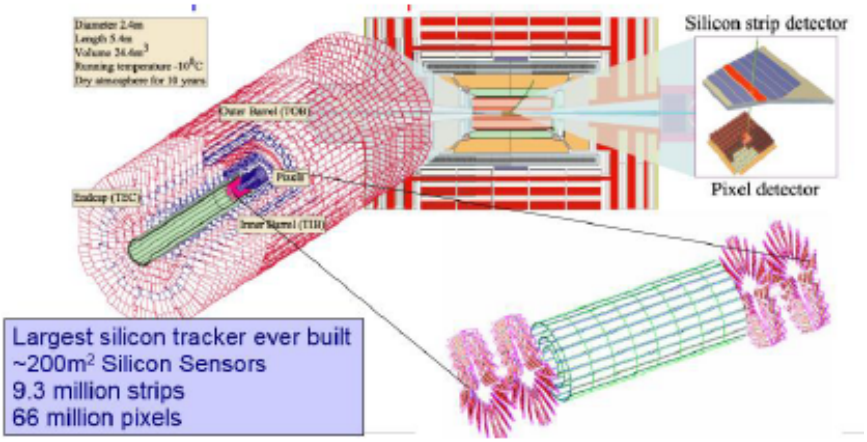

Figure 3.9: Schematic view of the CMS tracking system [39].

3.5 Calorimetry

A calorimeter measures the energy of particles. When particles enter the calorimeter, they initiate a particle shower and the particle's energy that is deposited in the calorimeter is measured. A shower is a cascade of secondary particles produced by a high energy particle interacting with the matter. The incoming particle interacts producing multiple new particles with lesser energy; each of these then interacts in the same way, a process that continues until an avalanche of low energy particles are produced. These are then stopped in the matter and is absorbed. There are two basic types of showers: EM and hadronic. EM showers are produced by a particle that interacts primarily via the EM force, usually a photon or electron. Hadronic showers are produced by the hadrons (i.e. nucleons and other particles made of quarks) and proceed mostly via the strong nuclear force. The CMS calorimeter is comprised of two types: the ECAL and HCAL.

3.5.1 Electromagnetic calorimeter

The ECAL of CMS is designed to measure the energies of electrons and photons with high accuracy. The ECAL [40] is a hermetic homogeneous calorimeter with a total coverage in pseudorapidity, $|\eta| < 3.0$. It is constructed from lead tungstate ($PbWO_4$), an extremely dense but optically transparent material, which is ideal for stopping high energy particles. When electron and photons pass through it, it scintillates and produces light in proportion to the particle's energy. As the calorimeter measurements are not used in the dimuon analysis, we do not discuss these subdetectors further. A basic layout of the ECAL is shown in Figure 3.10.

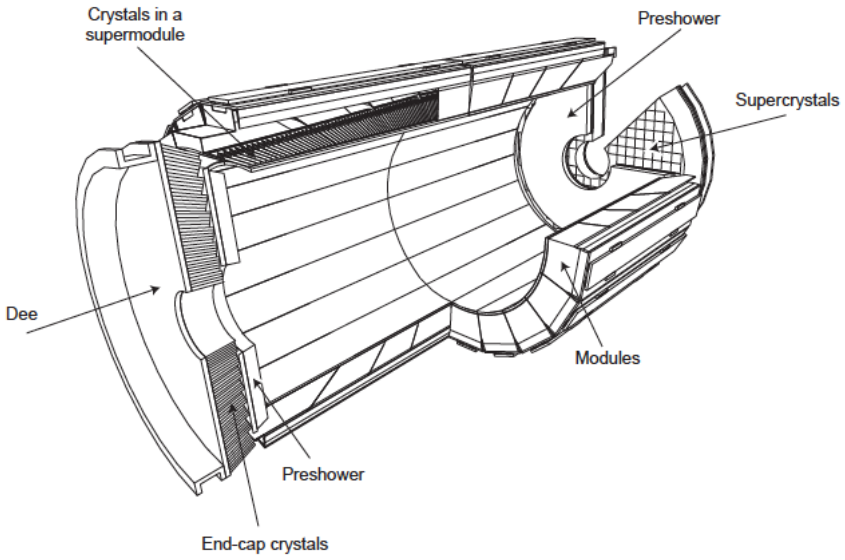

Figure 3.10: Layout of the CMS ECAL showing the arrangement of $PbWO_4$ crystals in the barrel and endcap regions along with the preshower detector [27].

3.5.2 Hadron calorimeter

The HCAL [41] is a sampling calorimeter made up of brass absorber materials and plastic scintillators. It is designed for measuring the hadronic jets and other exotic particles that leave a signature in the form of missing transverse energy, E_T^{Miss}. This calorimeter plays an essential role in the identification of the quarks and gluons by measuring the energy and direction of the jets. Moreover, it can indirectly detect particles that do not interact with the detector material such as the neutrino by conservation of the momentum in the transverse plane (i.e. missing transverse energy). Figure 3.11 shows the longitudinal view of the CMS detector with the HCAL coverage in η.

3.6 Magnet

The CMS magnet is the central device around which the whole CMS experiment is built. It is the largest superconducting magnet ever built in the world creating a

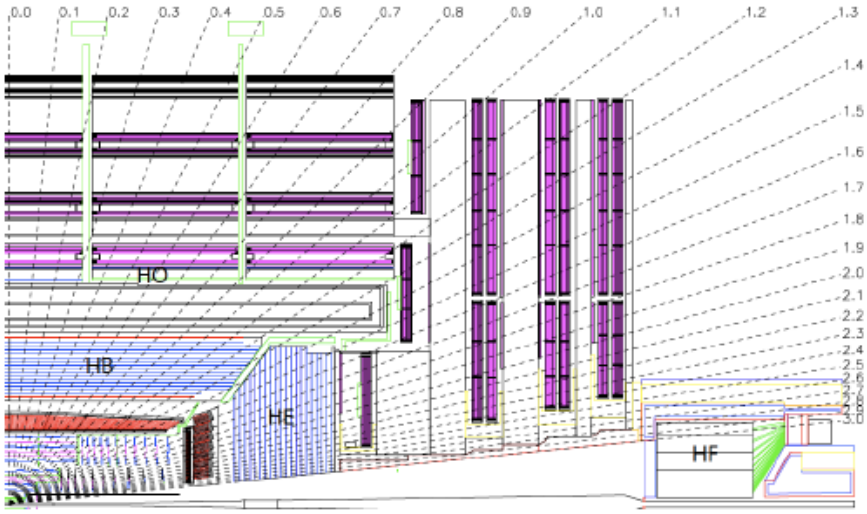

Figure 3.11: Longitudinal cross section of the quarter of the CMS detector showing the positions of the hadronic calorimeter barrel (HB), the hadronic calorimeter endcap (HE), the forward hadronic calorimeter (HF), and the outer hadronic calorimeter (HO) [27].

magnetic field of 4 T. Its job is to bend the path of the particles emerging from high energy collisions in the LHC. The more momentum a particle has, the less its path is curved by the magnetic field. Therefore, tracing its path gives a measure of momentum.

The magnet of the CMS detector is a superconducting solenoid and is designed to create a 4 T uniform magnetic field. The CMS magnet system is the conjunction of a superconducting coil embedded within a vacuum tank surrounded by the return iron yoke. The magnetic flux generated by the superconducting coil is returned through a return iron yoke. A field of 4 T brings substantial benefits for the muon tracking, inner tracking and the ECAL. The CMS magnet provides a large bending power allowing a precise measurement of the transverse momentum of the charged particles. The transverse momentum of a charged particle p_T in a magnetic field is; $p_T = 0.3 \times B \times R$, where B is the magnetic field and R is the radius of curvature of the charged particle. Its details can be found in the magnet project [42].

3.7 Muon system

One of the main design objectives of the CMS detector is to obtain a high precision muon momentum measurement, its key role both in the new physics searches and SM measurements. In particular, it is relevant for the analysis presented in this dissertation because the selection is based on a well reconstructed high p_T muon. Hence, a robust and redundant muon spectrometer is needed to provide the precise muon identification, good resolution of high p_T measurements, and the effective trigger capabilities.

The CMS muon system [34,43] is the outermost group of subdetectors of the CMS experiment, covering an $|\eta|$ region up to 2.4. It consists of three different types of the gaseous detectors whose design is driven by the differences in the radiation environment and magnetic field at different η regions. DTs are used in the barrel, up to $|\eta| < 1.2$, where both the muon rate and residual magnetic field are low. In the two endcap regions of the CMS where the muon rates and background levels are high and the magnetic field is large and non uniform, the muon system uses CSCs. With their fast response time, fine segmentation, and radiation resistance, the CSCs identify muons between $0.9 < |\eta| < 2.4$. There are four stations of the CSCs in each endcap with chambers positioned perpendicular to the beam line and interleaved between the flux return plates. The details of all of these detectors can be found in the muon TDR [43]. A schematic view of the one quadrant of the CMS muon system is shown in Figure 3.12.

The trigger capabilities of both the types of detector is complemented with the use of a gaseous parallel plate chambers called RPCs. They combine a moderated spatial resolution with the excellent time resolution. RPCs provide a fast, independent and highly segmented trigger. Trigger signals coming from the DTs, CSCs, and the RPCs

proceed in parallel to the Global Trigger in order to perform efficient rejection of background, track identification and selection over the transverse momentum of the muons. The muon system has three purposes: muon identification, momentum measurement, and triggering. Good muon momentum resolution and trigger capability are enabled by the high field solenoidal magnet and its flux return yoke. The CMS muon system is designed to have the capability of reconstructing the momentum and the charge of the muons over the entire kinematic range of the LHC.

A particle is measured by fitting a curve to hits on the four muon stations, which sits outside of the magnet coil and are interleaved with the iron return yoke. By tracking its position through the multiple layers of each station combined with tracker measurements, the detectors precisely trace a particle's path. This gives a measurement of its momentum as particles traveling with more momentum bend less in a magnetic field. As a consequence, the CMS magnet is very powerful; we can bend even the path of very high energy muons and calculate their momentum. In total, there are 1400 muon chambers: 250 DTs and 540 CSCs to track the particle's positions and provide a trigger, and 610 RPCs to form a redundant trigger system, which quickly decides to keep the acquired muon data or not. Because of the many layers of detector and different specialties of each type, the system is naturally robust and able to filter out background noise. DTs and RPCs are arranged in concentric cylinders around the beam line (the barrel region), CSCs and RPCs make up the endcaps disks that cover the ends of the barrel.

The DT system measures the muon positions in the barrel part of the detector where the muon rate is low and magnetic field is uniform. The barrel detector consists

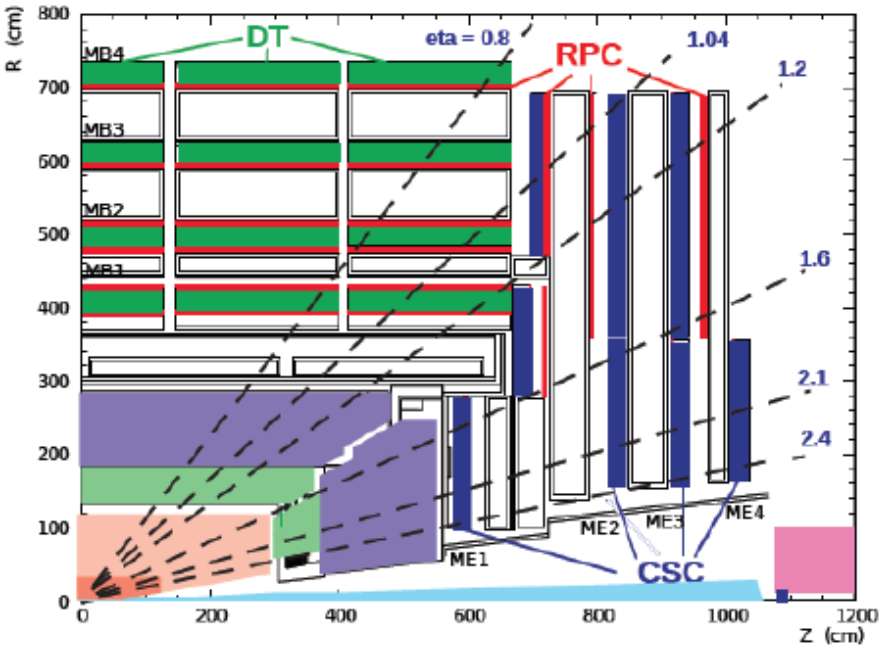

Figure 3.12: Layout of the CMS muon system shown for one quadrant of the CMS detector. The four barrel DT stations (MB1-MB4), four endcap CSC stations (ME1-ME4), and RPC stations are shown [27].

of four concentric stations of 250 chambers inside the magnet yoke of the CMS. The inner three stations have 60 drift chambers each and the outer station has 70 chambers. The barrel DT chambers cover the pseudorapidity region $|\eta| < 1.2$. It follows the yoke segmentation and consists of five iron wheels composed of 12 azimuthal sectors with each one covering an angular region of 30^0. Every wheel consists of four concentric rings of chambers called stations and labeled MB1, MB2, MB3, MB4 respectively, where MB stands for Muon Barrel. Each station is formed by 12 DT chambers with the exception of MB4, which consists of 14 of them. A schematic layout of the Muon barrel DT chambers is shown in Figure 3.13.

The basic detector element is a rectangular drift tube cell with a transverse size of 4.2 cm $\times$ 1.3 cm. Cells are filled with a $85\%\mathrm{Ar}, 15\%\mathrm{CO}_2$ gas mixture and are grouped

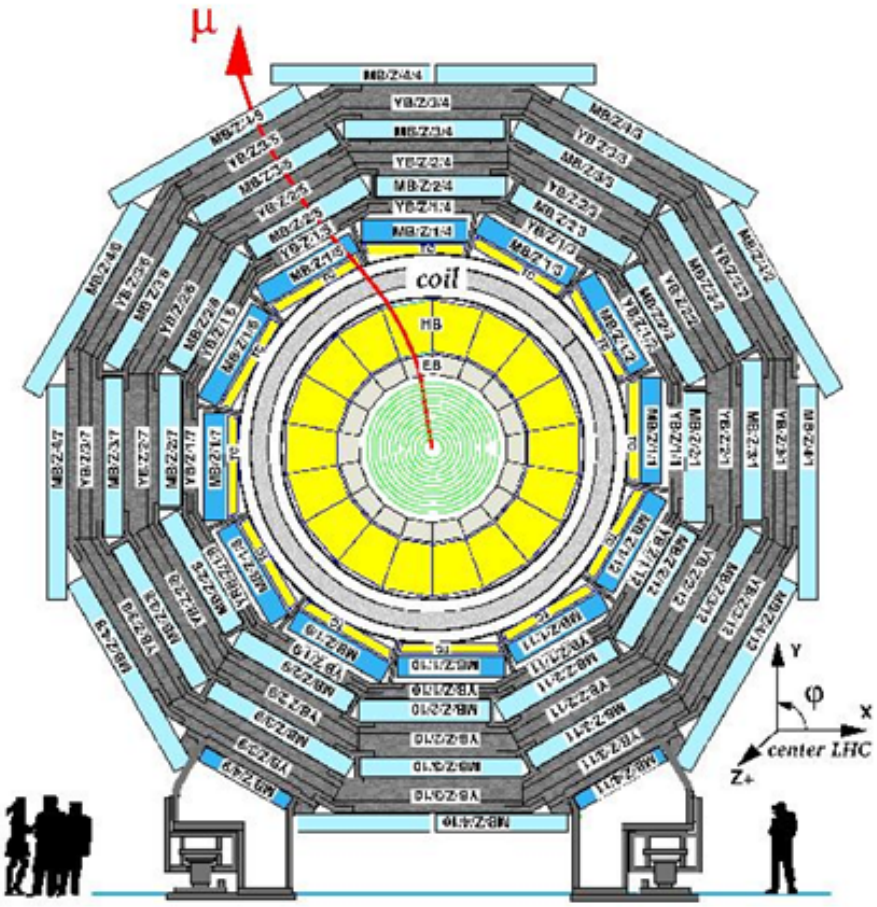

Figure 3.13: Layout of the muon barrel (MB) DT chambers in one of the five CMS barrel wheels. YB refers to the yoke barrel regions with the same numbering scheme used for the MB DT stations [27].

parallelly to form the detection layers. Each tube contains electrode plates that enclose a gas mixture and a stretched anode wire. When a muon or any charged particle passes through the gas, it liberates electrons from the atoms through ionization of the gas. The resulting electrons drift to the nearest anode wire. By recording where along the wire electrons hit as well as by calculating the muon's original distance from the anode wire, DTs give a muon's position measurement in two coordinates. Figure 3.14 demonstrates the layout of drift cell and the basic operation of a drift cell.

The CSCs constitute an essential component of the CMS muon detector that

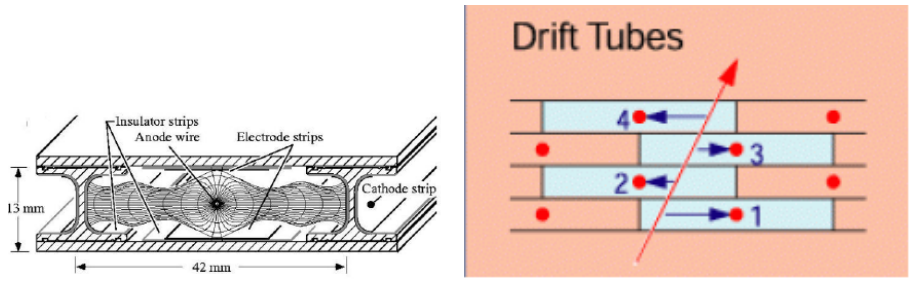

Figure 3.14: Left: Muon drift tube layout and operation [44]. The red line with the arrow shows a muon traversing the drift tube. The anode wires (shown by red dots) are perpendicular to the page. The horizontal blue lines with the arrow show the muon's distance from the anode wire (obtained by multiplying the speed of an electron in the tube by the drift time) [45].

provides precise tracking and triggering of the muons in the endcaps. Their performance is critical to many physics analyses based on muons. The ME system comprises 468 CSCs in the two endcap disks where the muon and background rates are high and the non-uniformed magnetic field is large. The CSCs cover the far forward region of the detector with $0.9 < |\eta| < 2.4$. Each endcap consists of four stations of chambers that are mounted on the disks enclosing the CMS magnet which is perpendicular to the beam's direction. The stations are ME1, ME2, ME3, and ME4, where ME stands for Muon Endcap. In each disk, the chambers are divided into two concentric rings around the beam axis. The station ME1 has three rings of chambers (ME1/1, ME1/2, ME1/3); ME2 and ME3 have two rings of chambers (ME2/1, ME2/2, ME3/1, ME3/2); and the outermost station ME4 has only one ring (ME4/1). There are 36 chambers in each ring of a muon station except for the innermost ring of the second through fourth disks (ME2/1, ME3/1, and ME4/1) where there are 18 chambers.

CSCs are the multi-wire chambers trapezoidal in shape and consists of six gas gaps, each gap having a plane of radial cathode strips and a plane of anode wires running almost perpendicularly to the strips. All CSCs except those in the third ring of the first

endcap disk (ME1/3), are overlapped in ϕ to avoid gaps in the muon acceptance. All CSCs consist of arrays of positively-charged anode wires crossed with the negatively-charged copper cathode strips within a gas volume. The basic layout of a CSC chamber is shown in the left panel of Figure 3.15 .

When the muons pass through the CSCs, they knock electrons off the gas atoms, which drifts to the anode wires creating an avalanche of electrons. Positive ions move away from the wire and towards the copper cathode also inducing a charge pulse in the strips at right angles to the wire direction. Because the strips and the wires are perpendicular, we get two position coordinates for each passing particle. The closely-spaced wires make the CSCs fast detectors suitable for triggering. The signal on the wires is fast and is used in the Level-1 Trigger. However, it leads to a coarser position resolution. A precise position measurement is made by determining the center of gravity of the charge distribution induced on the cathode strips. Each CSC measures up to six space coordinates (r, ϕ, z). Each CSC module contains six layers making it able to accurately identify the muons and match their tracks to those in the tracker. The spatial resolution provided by each chamber from the strips is typically about 200 μm (100 μm for ME1/1). The angular resolution in ϕ is of the order of 10 mrad. The right panel of Figure 3.15 shows the basic principle of CSC operation.

The CSCs have different sizes. The 144 largest CSCs, ME2/2 and ME3/2, are 3.4 m long along the strip direction and up to 1.5 m wide along the wire direction. The overall area covered by the sensitive planes of all chambers is about 5000 m^2, the gas volume is $\sim$ 50 m^3, and the number of wires is about two million. The nominal gas is a mixture of $40\%\mathrm{Ar}, 50\%\mathrm{CO_2}$ and $10\%\mathrm{CF_4}$. The CO_2 component is a non-flammable

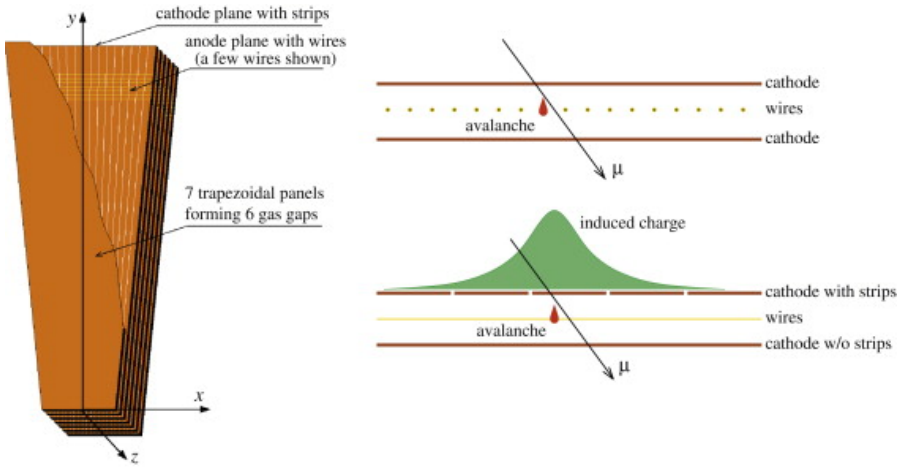

Figure 3.15: Left: A schematic view of a CSC. Right: An illustration of the CSC operation principle. An electron avalanche resulting from a muon traversing a gas gap produces a signal on the anode wires and induces a distributed charge on the cathode strips [46].

quencher needed to achieve large gas gains while the main function of the CF_4 is to prevent the polymerization on wires. The CSCs provide the functions of precision muon measurement and muon trigger in one device. The chamber position resolution varies from 75 to 200 μm, from the first to the last station, to cope with the CMS goal for momentum resolution.

RPCs combine adequate spatial resolution with a time resolution comparable to that of scintillators. They are capable of tagging the time of an ionizing event in a much shorter time than the 25 ns between two consecutive LHC bunch crossings (BXs). Therefore, a fast dedicated muon trigger device based on RPCs can unambiguously identify the relevant BX to which a muon track is associated even in the presence of the high rate and background expected at the LHC. Signals from such devices directly provide the time and position of a muon hit with the required accuracy.

The RPCs are double gap chambers with bakelite strips, operated in avalanche

mode to ensure good operation at high rates. They produce a fast response with good time resolution, but a coarser position resolution than the DTs or CSCs. They also help to resolve the ambiguities in attempting to make tracks from the multiple hits in a chamber. A total of six layers of RPCs are embedded in the barrel muon system, two in each of the first two stations, and one in each of the last two stations. The redundancy in the first two stations allows the trigger algorithm to work even for low p_T tracks that may stop before reaching the outer two stations. In the endcap region, there is a plane of RPCs in each of the first three stations in order for the trigger to use the coincidences between stations to reduce background, to improve the time resolution for BX identification, and to achieve a good p_T resolution. Finally, a sophisticated alignment system measures the positions of the muon detectors with respect to each other and to the inner tracker in order to optimize the muon momentum resolution.

RPCs consist of two parallel plates, a positively-charged anode and a negatively-charged cathode both are made of a very high resistivity plastic material and separated by a gas volume. When a muon passes through the chamber, electrons are knocked out of gas atoms. These electrons in turn hit other atoms causing an avalanche of electrons. The electrodes are transparent to the signal (the electrons), which are instead picked up by the external metallic strips after a small, but precise time delay. The pattern of hit strips give a quick measure of the muon momentum, which is then used by the trigger to make immediate decisions about whether the data are worth keeping. RPCs combine a good spatial resolution with a time resolution of just one nanosecond.

3.8 Muon reconstruction

The strategy for the physics analysis in the CMS is based on the reconstruction of the high level physics objects, which correspond to particles traveling through the detector. The detector's components record the signal of a particle as it travels through the material of the detectors and this signal is reconstructed as individual points in space known as recHits. To reconstruct a physical particle traveling through the detector, the recHits are associated together to determine points on the particle's trajectory. The characteristics of the trajectory as it travels through the detector are then used to define its momentum, charge, and particle identification.

The CMS muon system is designed to identify and reconstruct muons over the pseudorapidity interval $|\eta| < 2.4$. This results high reconstruction effciencies (>99%) for the muons that are within the η range and have sufficient p_T [34]. Also, the high magnetic field makes possible the excellent muon momentum resolution. In the standard CMS reconstruction procedure, particle tracks are first reconstructed independently in the inner tracker (referred to as tracker tracks) and in the muon system (referred to as standalone muon tracks). Tracks are also reconstructed locally within the muon system using available DT or CSC particle hits (referred to as muon segments). Based on these, muon reconstruction is done by the following two approaches:

- Tracker muon reconstruction (inside-out): In this approach, all tracker tracks above a certain p_T threshold are considered and are extrapolated to the muon system for matching muon segments. If at least one muon segment matches the extrapolated tracker track, the corresponding tracker track is qualified as a tracker muon track.

- Global muon reconstruction (outside-in): In this approach, standalone muon tracks are extrapolated for matching tracker tracks. If one is found, hits from the tracker track and standalone muon tracks are combined and used to determine a global muon track. In the specific case, when tracker tracks are not available in a given collision event, only a standalone muon track is reconstructed. However, this is very rare (occurring in only about 1% of the events) due to high tracker efficiency. At low momentum ($p_T \sim 20GeV/c$), the tracker muon reconstruction is more efficient than the global muon reconstruction, because it requires only one matching muon segment. At high momentum ($p_T > 200GeV/c$), global reconstruction gives high efficiency (as muons penetrate more than one station at high p_T) and significantly improves the muon momentum resolution compared to the tracker only fit [34, 47]. Figure 3.16 shows a comparison of momentum resolution when reconstructed with different approaches.

3.9 Dimuon invariant mass

In mathematics and theoretical physics, an invariant is a property of a system which remains unchanged under some transformation. The invariant mass is a characteristic of the total energy and momentum of an object or a system of objects that is the same in all frames of reference related by Lorentz transformations. If objects within a system are in relative motion, then the invariant mass of the whole system will differ from the sum of the objects' rest masses.

In particle physics, the invariant mass is equal to the mass in the rest frame of the particle, and can be calculated by the particle's energy E and its momentum **p** as

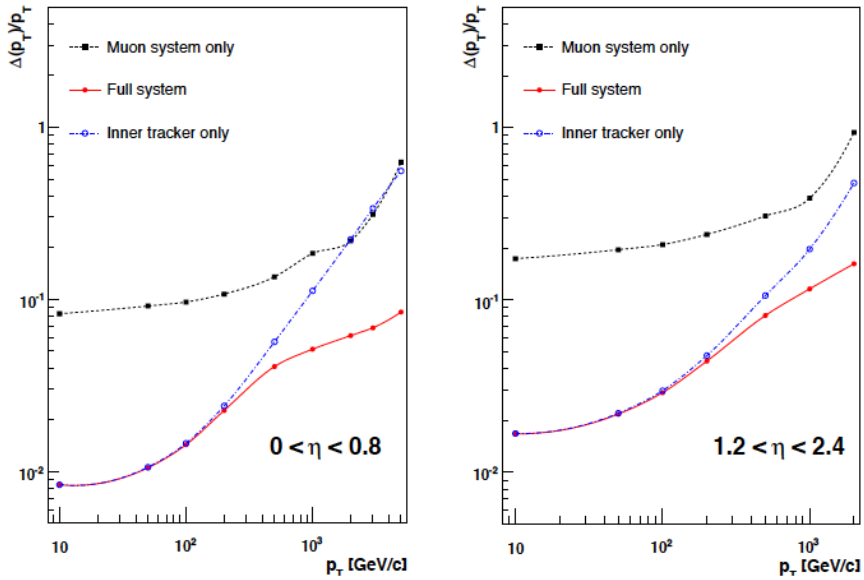

Figure 3.16: The muon p_T resolution as a function of p_T using simulated data for the" muon system only", the " inner tracking system only", and the "full system" [27].

measured in any frame, by the energy-momentum relation:

$$\mathrm{M}^2 = (E_1 + E_2)^2 - |\mathbf{p}_1 + \mathbf{p}_2|^2 = m_1^2 + m_2^2 + 2E_1E_2 - 2\mathbf{p}_1\mathbf{p}_2 \tag{3.5}$$

One practical application of the conservation of the invariant mass involves combining the four-momenta $\mathbf{P}_A$ and $\mathbf{P}_B$ of two daughter particles produced in the decay of a heavier particle with four-momentum $\mathbf{P}_C$ to find the mass of the heavier particle. Conservation of four-momentum gives $\mathbf{P}_C = \mathbf{P}_A + \mathbf{P}_B$, while the mass M of the heavier particle is given by $M^2 = -|\mathbf{P}_C|^2$. By measuring the energies and three-momenta of the daughter particles, we can reconstruct the invariant mass of the two particle system, which must be equal to M. This technique is used in experimental searches for Z' bosons at high energy particle colliders, where the Z' boson would show up as a bump in the invariant mass spectrum of electron-positron or muon-antimuon pairs.

We use four-momentum (E, **p**) of two oppositely-charged muons to calculate the invariant mass of the dimuons in our analysis, which is the same as the four-momenta invariant mass technique mentioned in the previous paragraph to account for short-lived particles, e.g. for the Z boson, for which the energy and momentum of the muon and antimuon decay products are measured.

The measured invariant mass of the dimuon gives the estimate of the mass of the particle which decays into a pair of muons. If the pair of muons really stems from a Z' boson, the invariant mass distribution will feature a peak around the corresponding mass. If a peak is observed at a certain mass value, which does not correspond to any known particle, there is a chance that a new particle has been discovered. This method is general and can be applied to any particle produced in resonance and decaying into secondary particles.

3.10 Trigger and data acquisition system

The Trigger and data acquisition system (DAQ) of the LHC experiment is necessary because the collision data rate is much higher than the rate of writing data to mass storage. The LHC provides pp collisions with a very high interaction rate, about 10^9 events per second. The designed BX interval for proton beams is 25 ns, which corresponds to a BX frequency of 40 MHz, but the maximum storage rate allowed is 100 Hz. Depending on luminosity, several collisions occur at each crossing of the proton bunches at approximately 20 pp collisions at the nominal design luminosity of $10^{34}\text{cm}^{-2}\text{s}^{-1}$, producing approximately one MB of data. Since it is impossible to store and process the large amount of data associated with such a high number of events, a drastic reduction in the event rate has to be achieved to preserve the interesting physics events. This

task is performed by the trigger system, which is the start of the physics event selection process.

The rate is reduced in two steps, called Level-1 (L1) Trigger [48] and High Level Trigger (HLT) [49]. The L1 trigger consists of custom designed, largely hardware-based programmable electronics, whereas the HLT is a software based system implemented in a filter farm of about 1000 commercial computer processors. The event rate reduction capability is designed to be at least a factor of 10^6 for the combined L1 and HLT triggers. The design output rate limit of the L1 trigger is 100 kHz. The L1 trigger uses coarsely segmented data from the calorimeters and the muon system while holding the high resolution data in pipelined memories in the front end electronics. The HLTs that are implemented as a computer processing farm is designed to achieve a rejection factor of 10^3, write up to 100 events per second to mass computer storage. The last stage of HLT processing does the reconstruction and event filtering with the primary goal of making datasets of different signatures on easily accessible media.

The architecture of the DAQ of the CMS detector is shown schematically in Figure 3.17. The CMS Trigger and DAQ system is designed to collect and analyze the detector information at the LHC BX frequency of 40 MHz. The DAQ system must sustain a maximum input rate of 100 kHz and provide enough computing power for a software filter system, the HLT, to reduce the rate of stored events by a factor of 1000. Thus, the main purpose of the DAQ and HLT systems is to read the CMS detector event information for those events that are selected by the L1 Trigger and to select the most interesting ones for output to mass storage among those events. The proper functioning of the DAQ at the desired performance will be a key element in reaching the physics

potential of the CMS experiment. In addition, to maximize this physics potential, the selection of events by the HLT must be kept as broad and as inclusive as possible so as not to loose signal.

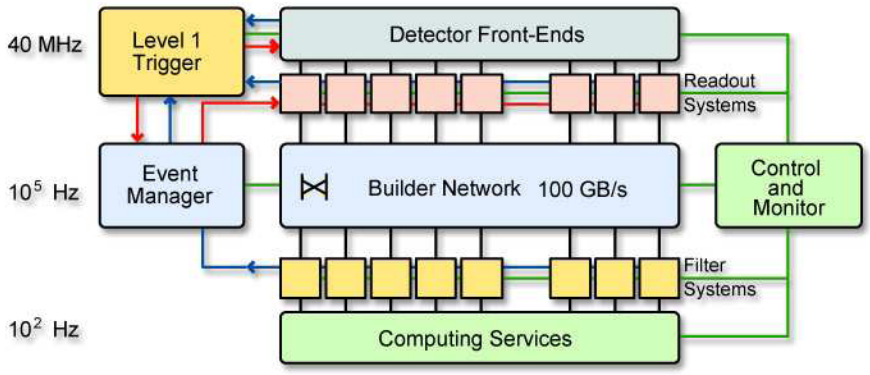

Figure 3.17: Architecture of the CMS DAQ system [34].

CHAPTER 4

Muon Endcap Alignment

The Muon Endcap Alignment system is designed to continuously monitor the actual positions of the CSCs relative to the tracking system. When the high magnetic field is switched on and off, the chambers mounted on the endcap yokes undergo substantial motion and deformation. Details of the design and performance of the alignment system can be found elsewhere [50–52]. In this chapter, we focus on the alignment performance for the rϕ (X_{CMS}, Y_{CMS}) coordinates in terms of resolution and precision achieved with full optical sensor system.

4.1 Introduction

The alignment system for the CMS muon endcap detector consists of several hundred sensors such as optical 2D CCD sensors illuminated by lasers and analog distance and tilt sensors to monitor the position of one sixth of 468 large CSCs. The chambers mounted on the endcap yoke disk undergo deformation when 3.8 Tesla (T) magnetic field is applied. The ME alignment system is required to monitor the chamber positions with 75-200 μm accuracy in rϕ, 400 μm in the radial direction and $\sim$1 mm in the Z direction. We reconstruct the absolute X_{CMS} and Y_{CMS} positions of chambers at B = 0 T (Feb 15, 2010) and B = 3.8 T (March 6, 2010), the data from the optical system. We also compare the reconstructed results with photogrammetry (PG) measurements at B = 0 T

to find the accuracy of the results. We also check the accuracy of the optical alignment measurements against PG data at B = 0 T provided by the CERN survey group that performed the survey and PG measurements of all ME stations when the magnetic field is off. Figure 4.1 below shows one of the muon endcap stations with fully-installed CSCs.

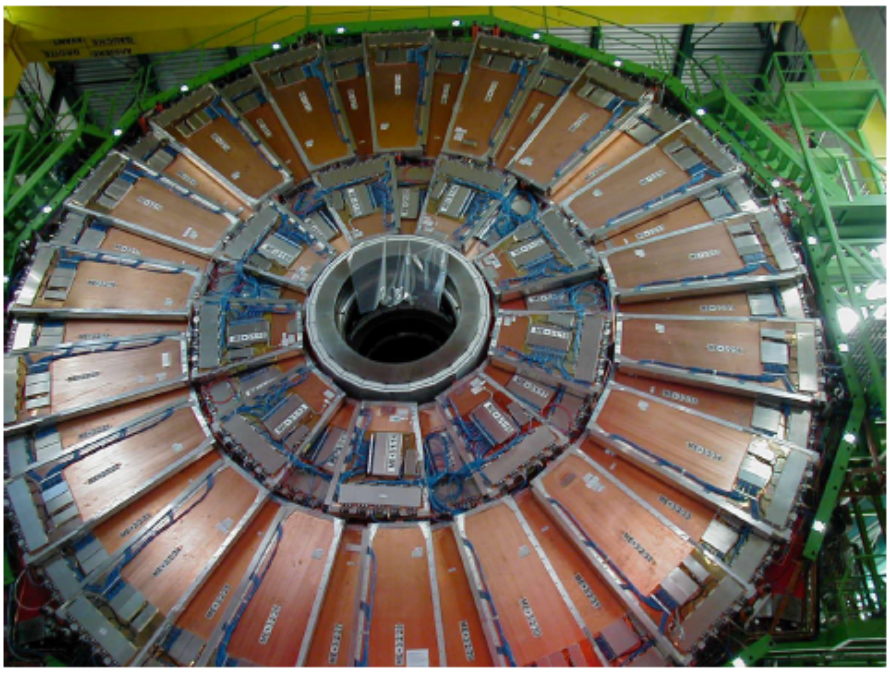

Figure 4.1: Fully instrumented CMS ME station ME+3, with CSCs [53].

4.2 Muon endcap system design

The task of the ME alignment system is to provide absolute positions of the CSCs in rϕ (X,Y) and Z coordinates of the CMS. Because of the geometrical constraints and economy, the system only aligns one sixth of the all chambers. The main monitoring tools in the rϕ planes are Straight Line Monitors (SLMs). Two crosshair lasers, which emit a nearly radial laser beam across four chambers from each end, provide straight reference lines that are picked up by two optical sensors called Digital CCD Optical Position Sensors (DCOPS) on each chamber as shown in Figure 4.2. Every DCOPS

consists of four linear CCDs, each with 2048 pixels and 14 μm pixel pitch. The system also uses R-sensors for monitoring radial chamber positions, Z-sensors for axial distance measurements between the stations, and inclinometers for monitoring the tilt of the transfer plates on which lasers, reference DCOPS, and Z-sensors are mounted. The rϕ alignment is performed by the optical SLMs and transfer lines. The SLMs run across the surfaces of one sixth of all the CSCs along radial directions and link two axial transfer lines on the opposite sides of a disk as shown in Figure 4.3. Lasers, reference DCOPS, and transfer DCOPS are mounted on the Transfer Plates (TPs). Any tilt or displacement of these TPs away from their nominal positions changes the direction of the SLM laser beam and produces a bias in the measurements of the CSCs [51].

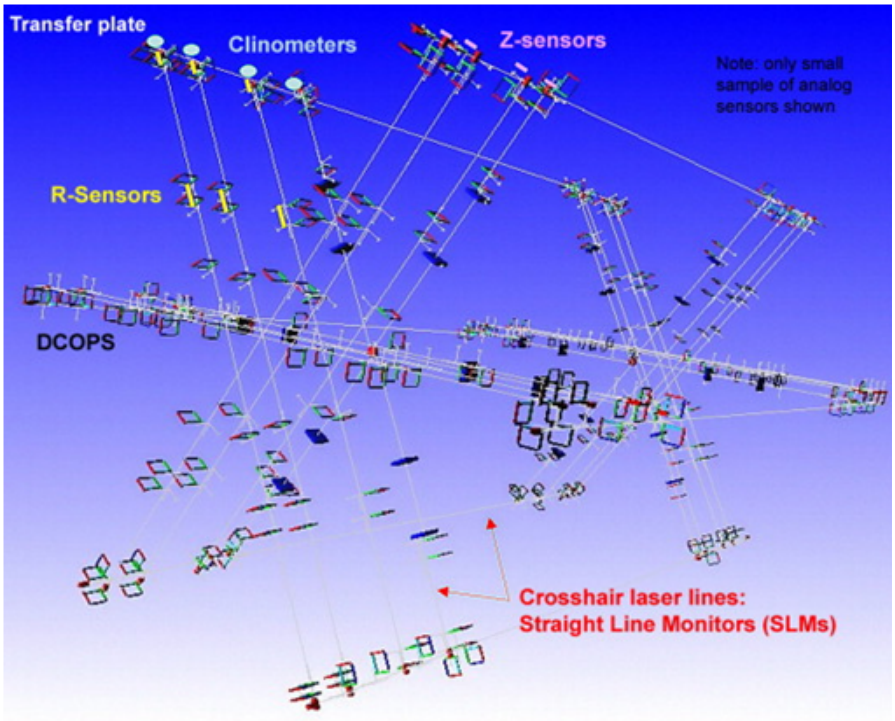

Figure 4.2: Visualization of the geometry and optical components of the CMS ME alignment system. The square objects represent digital optical alignment sensors (DCOPS) for monitoring three straight laser lines across each muon endcap station [51].

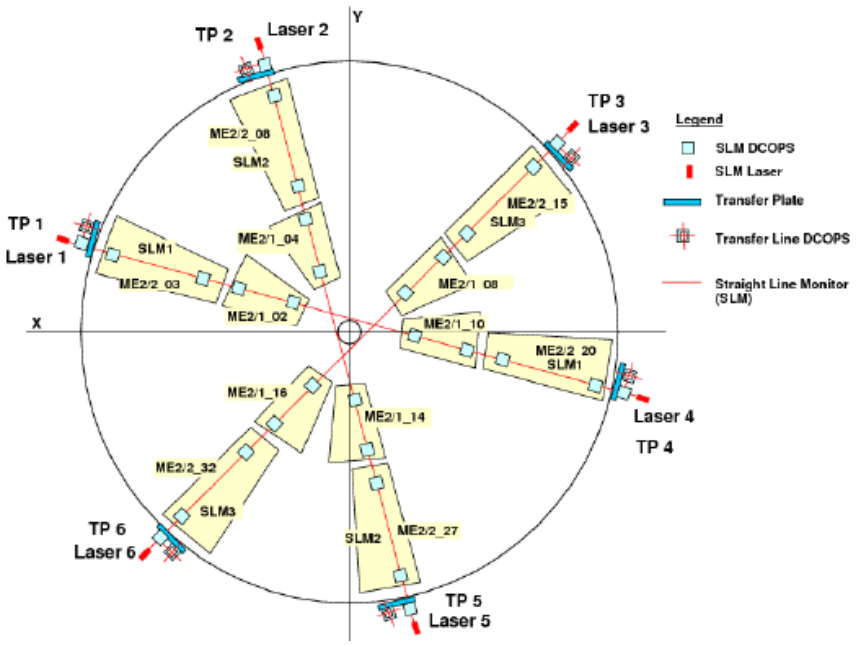

Figure 4.3: Schematic rϕ view of straight line monitors in the ME+2 station. Locations of axial transfer lines running perpendicular to the plane and across endcaps are indicated. Optical sensors and other alignment components are also shown [50].

4.3 Offline geometry reconstruction with COCOA

The muon alignment system uses a reconstruction software program called CMS Object oriented Code for Optical Alignment (COCOA), which transforms the various measurements into a reconstructed aligned geometry. It reconstructs the position and orientation of the optical system objects and chambers with full propagation of errors. The alignment geometry of the chambers and all alignment objects within the system are organized in a hierarchical order using a system description file (SDF). The starting geometry at B = 0 T uses two types of measurements: PG and survey. The PG measurements of the CSCs and alignment components are done with an open detector with respect to the disks. The survey measurements are generally performed for disks and wheels after closing the detector and in the global CMS reference frame. The geometry

reconstruction proceeds independently for each alignment subsystem. The output of the COCOA contains the best geometrical description of the system compatible with the measurements. The reconstructed results must be validated before they can be used for the muon track reconstruction. For the optical-based measurements presented in this dissertation, the accuracy is determined by comparing the reconstructed results at B = 0 T with the PG measurements. This is only an independent method to check the results. It is expected that, on average, the PG values and reconstructed values agree. If the alignment reconstruction is done correctly, the distribution of the difference between the PG and reconstructed position is expected to have a mean of zero. The deviation from zero is taken as an estimate of the systematic error in the reconstruction [50].

4.4 Reconstruction of the CSC positions in ME± 1

In the ME1 stations, the straight line monitors cannot reach across the entire endcap disk as they are blocked (by design) by the calorimeters attached to the YE1 yoke disks. Therefore, instead of three full length SLMs, there are six half length SLMs in each ME1 station. Each half length SLMs observes two chambers (one in ME1/2 ring and one in the outer ME1/3 ring) and connects to the link alignment laser lines at the inner radius and to the barrel Module for Alignment of the Barrel (MABs) at the outer radius. The reconstruction of the CSC positions in ME1 using half SLM data is more complex than the reconstruction of full length SLM in ME±2,3,4, because additional informations from the link alignment is required. For the ME1/1 and ME1/2 chambers, $X_{CMS}, Y_{CMS}, Z_{CMS}$ coordinates as well as the chamber rotations are obtained from the reconstruction of the link sensors data. The reconstruction procedures and results for the chamber positions in ME1/1, ME1/2 and ME1/3 are described in [50].

4.5 Reconstruction of the CSC positions in ME±2,3,4

Our analysis of the 2010 data focuses on determining the CSC positions in the global rϕ plane (X_{CMS},Y_{CMS}) perpendicular to the beam line. First, we reconstruct the chamber positions at B = 0 T. An example of the simultaneous fit for both the lasers in rϕ at B = 0 T is shown in Figure 4.4 for ME+2 SLM1. We then reconstruct the position of all monitored chamber at B = 3.8 T using an input on the DCOPS measurements and the absolute Z_{CMS} position of the endcap yoke disk centers provided by survey as listed in Table 4.1 [54]. Figures 4.5 and 4.6 show the simulatenous fit for both the lasers in rϕ at B = 3.8 T. The discrepancies in rϕ between reconstructed values and the PG measurements is shown in Figure 4.7 for all ME±2,3,4 stations.

Yoke disk center	x_{CMS}^{meas}[mm]	y_{CMS}^{meas}[mm]	z_{CMS}^{meas}[mm]	$z_{CMS}^{nominal}$[mm]
YE+3	-0.3	2.0	9909.30	9900.00
YE+2	-1.2	-1.2	8825.30	8820.00
YE+1	1.5	-0.2	7567.00	7560.00
YE-1	-1.1	-0.5	-7567.90	-7560.00
YE-2	1.1	0.3	-8825.30	-8820.00
YE-3	-1.4	-0.2	-9903.10	-9900.00

Table 4.1: Position of the muon endcap yoke disk centers in global CMS coordinates measured by survey with the closed detector before the STARTUP 2010 [54]. The nominal global Z position of the yoke disk centers are also shown for comparison. Nominal (X,Y) coordinates are (0,0) for all the yoke disks.

Reconstruction at B = 3.8 T cannot be checked against PG or the survey because these cannot be performed for a closed detector when the magnetic field is on. Therefore, we explicitly assume that the COCOA reconstruction of the CSC position at B = 3.8 T has very similar errors as the B = 0 T reconstruction because of the same reconstruction method in both cases. The X_{CMS}, Y_{CMS} information is derived from the alignment pin position; the center is nearly at the midpoint between the pins. Figure 4.8 shows an

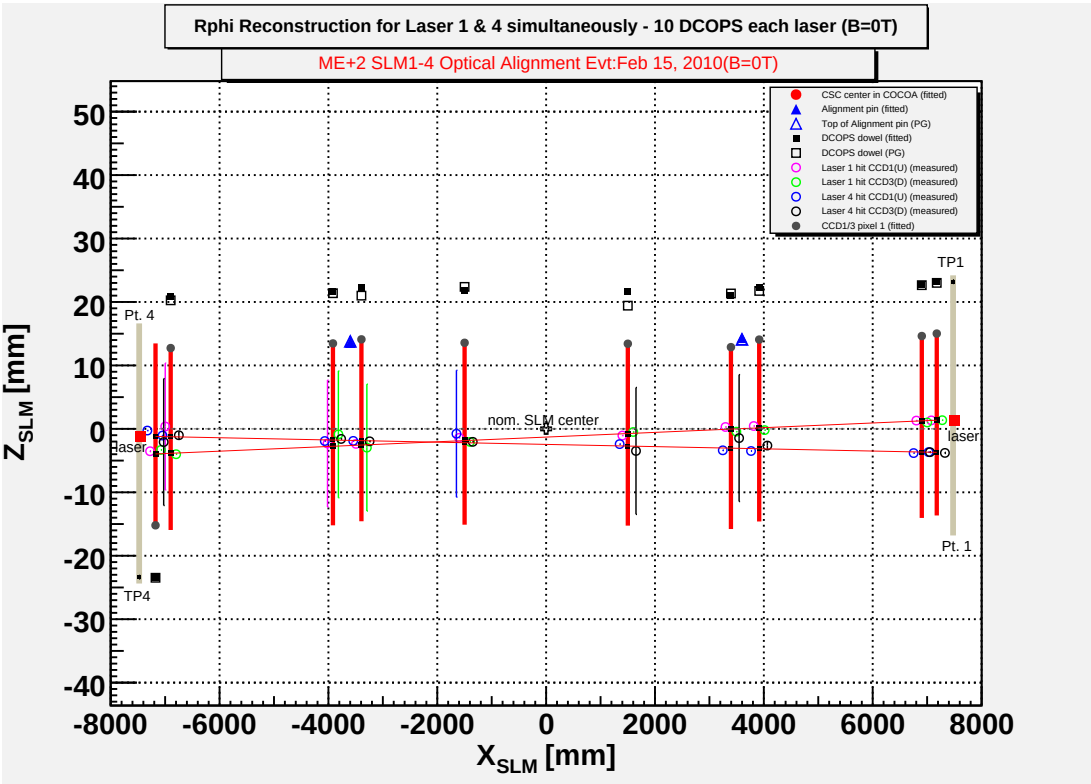

Figure 4.4: Reconstruction result for the DCOPS positions in Z_{SLM} vs. X_{SLM} along a SLM at B = 0 T in zoom version. The data shown are for a SLM connecting TP1 and TP4 of the station ME+2. The large vertical bars indicate the fitted positions of optical sensors. Laser hits on optical sensors are indicated by open circles with error bars.

example of the SLM fit residuals in rϕ at B = 0 T at the top and B = 3.8 T at the bottom (i.e. the difference between the measured and fitted laser hit positions of the DCOPS for all SLMs in the ME+2 station). The sigma of the plots gives the precision of the reconstructed positions. Table 4.2 summarizes the mean and sigma of the all the SLMs in ME$\pm$2,3,4 stations. The outliers in the plots indicate that there are some points that are slightly away from the mean of the distribution, which is due to a bad profile of the laser hits on the CCDs for some of the DCOPS. Figure 4.9 below shows the SLM fit residuals for all SLMs in ME+2,3,4 (top) and ME-2,3,4 (bottom) stations when the magnetic field is on.

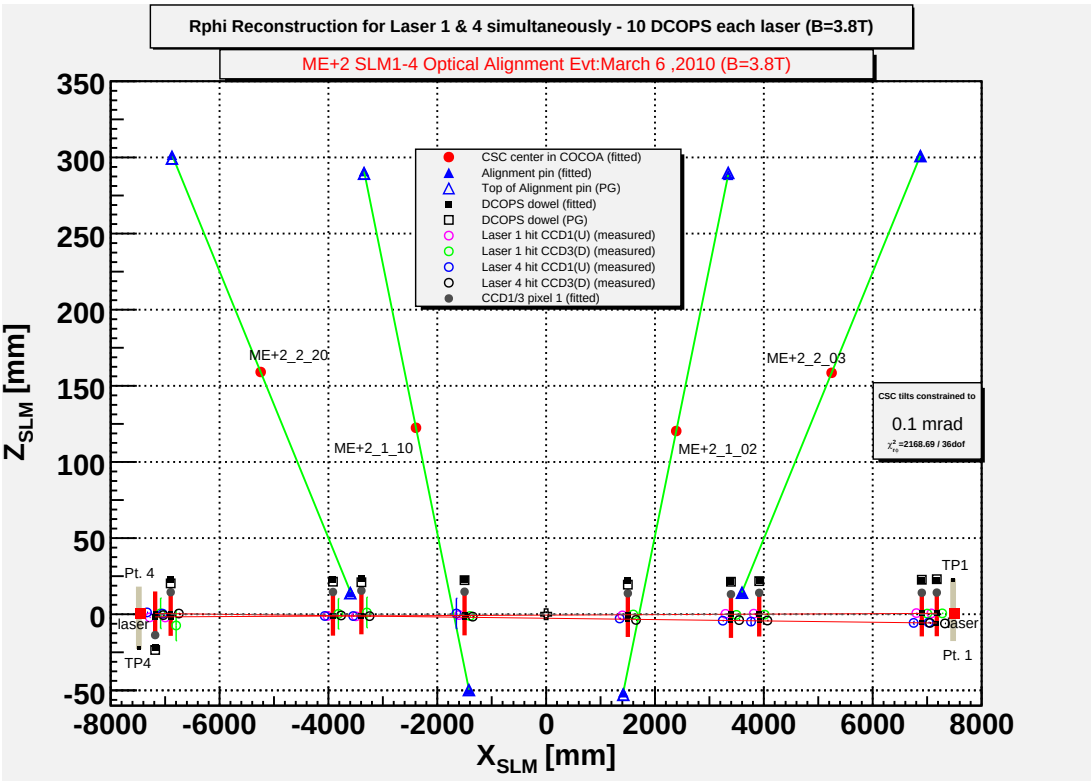

Figure 4.5: Reconstruction result for the DCOPS positions in Z_{SLM} vs. X_{SLM} along a SLM at B = 3.8 T. The data shown are for a SLM connecting TP1 and TP4 of the station ME+2. The large vertical bars indicate the fitted positions of optical sensors. Laser hits on optical sensors are indicated by open circles with error bars.

Residuals in Rϕ[mm] at B = 3.8 T		
Station	Mean	Sigma
ME+2	-0.019	0.153
ME+3	-0.004	0.217
ME+4	0.010	0.118
ME+234	-0.003	0.168
ME-2	0.001	0.137
ME-3	0.008	0.150
ME-4	0.004	0.143
ME-234	0.005	0.143

Table 4.2: Mean and sigma of the fit residuals at B = 3.8 T for all the SLMs in ME$\pm$2,3,4 stations. The sigma gives the precision of the reconstructed position.

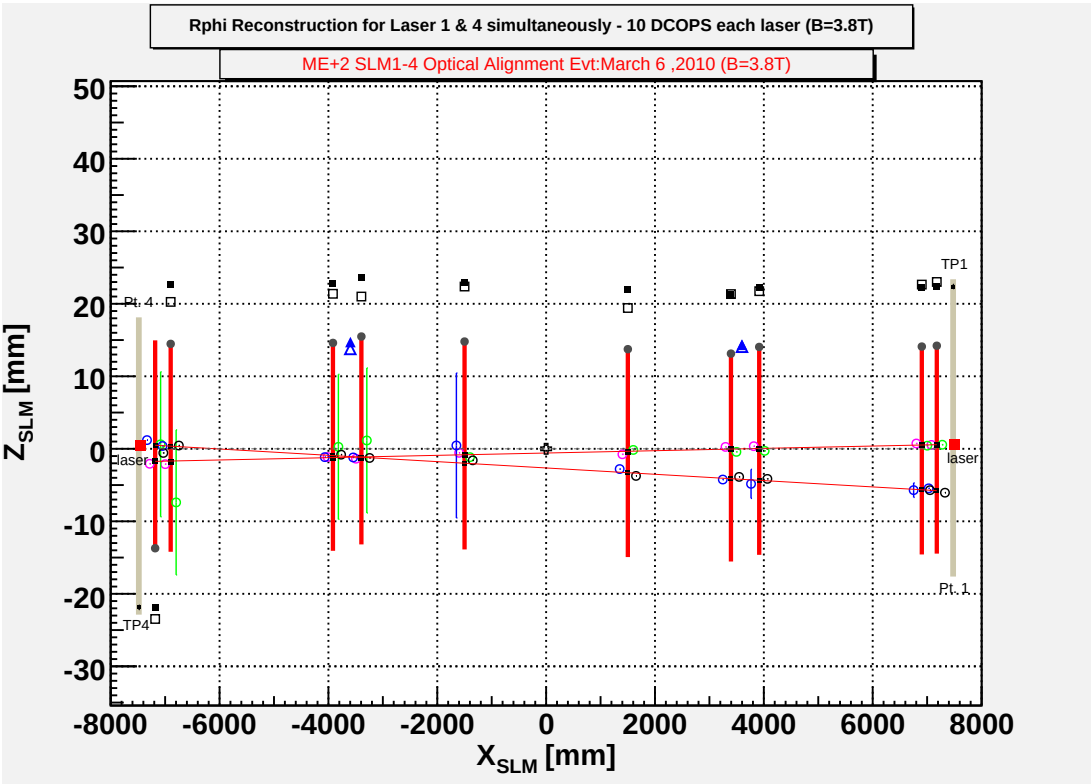

Figure 4.6: Reconstruction result for the DCOPS positions in Z_{SLM} vs. X_{SLM} along a SLM at B = 3.8 T in zoom version. The data shown are for a SLM connecting TP1 and TP4 of the station ME+2. The large vertical bars indicate the fitted positions of optical sensors. Laser hits on optical sensors are indicated by open circles with error bars.

4.6 Muon endcap alignment constants

The hardware-based detector geometry at B = 3.8 T is provided in the form of alignment constants for reprocessing the 2010 data. For the monitored chambers of MEs, the position and orientation of the chambers are provided by the COCOA reconstruction. In case of unmonitored chambers, X_{CMS},Y_{CMS} values are obtained by combining informations from PG. For the first time, we provide X_{CMS},Y_{CMS} positions of the CSCs in all ME±2,3,4 disks, based on hardware measurements. In the case of monitored ME±2,3,4

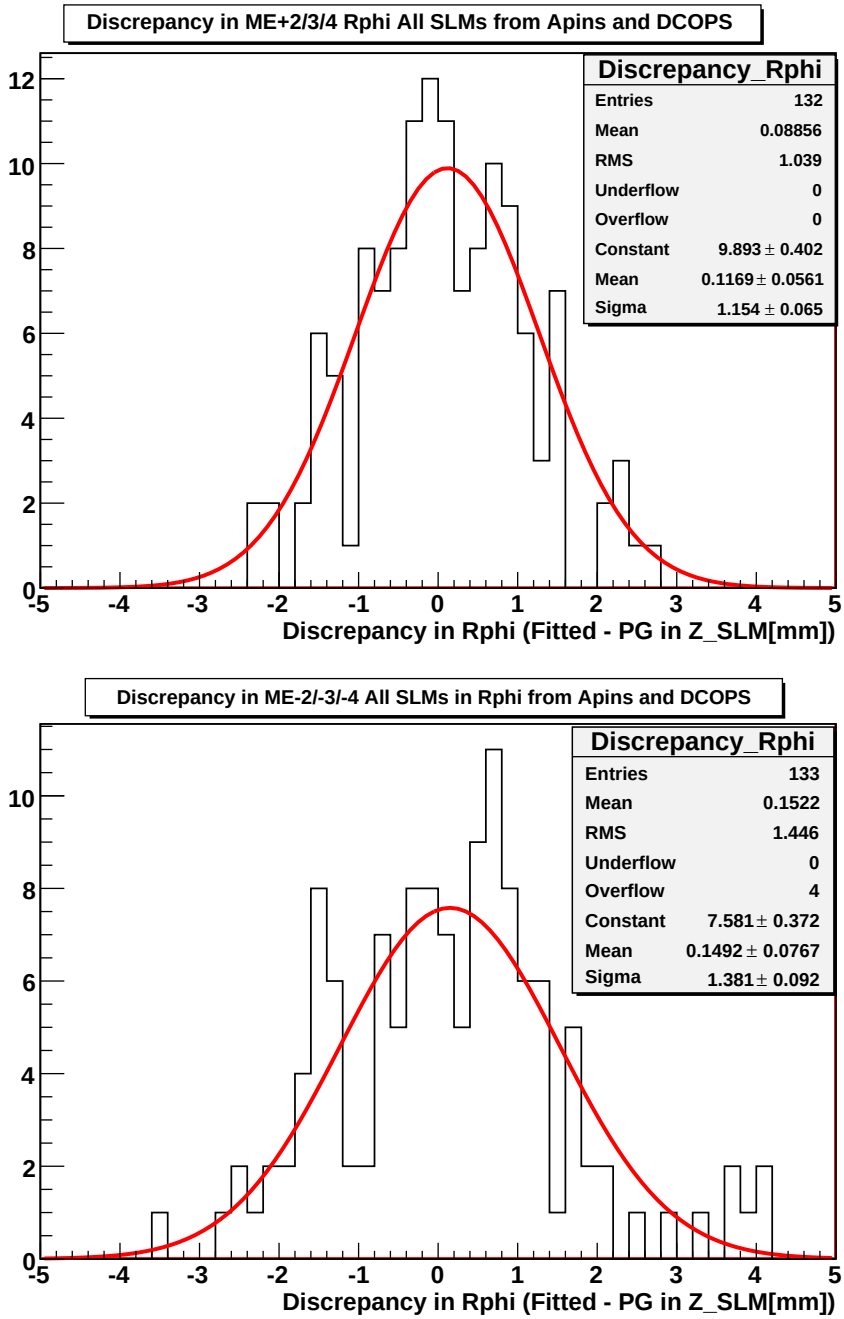

Figure 4.7: Discrepancy in rϕ positions between the COCOA reconstructed and photogrammetry (PG) at B= 0 T, for all SLMs from alignment pins and the DCOPS in ME+2,3,4 stations (top) and in ME-2,3,4 (bottom) using full SLMs fitted with a Gaussian.

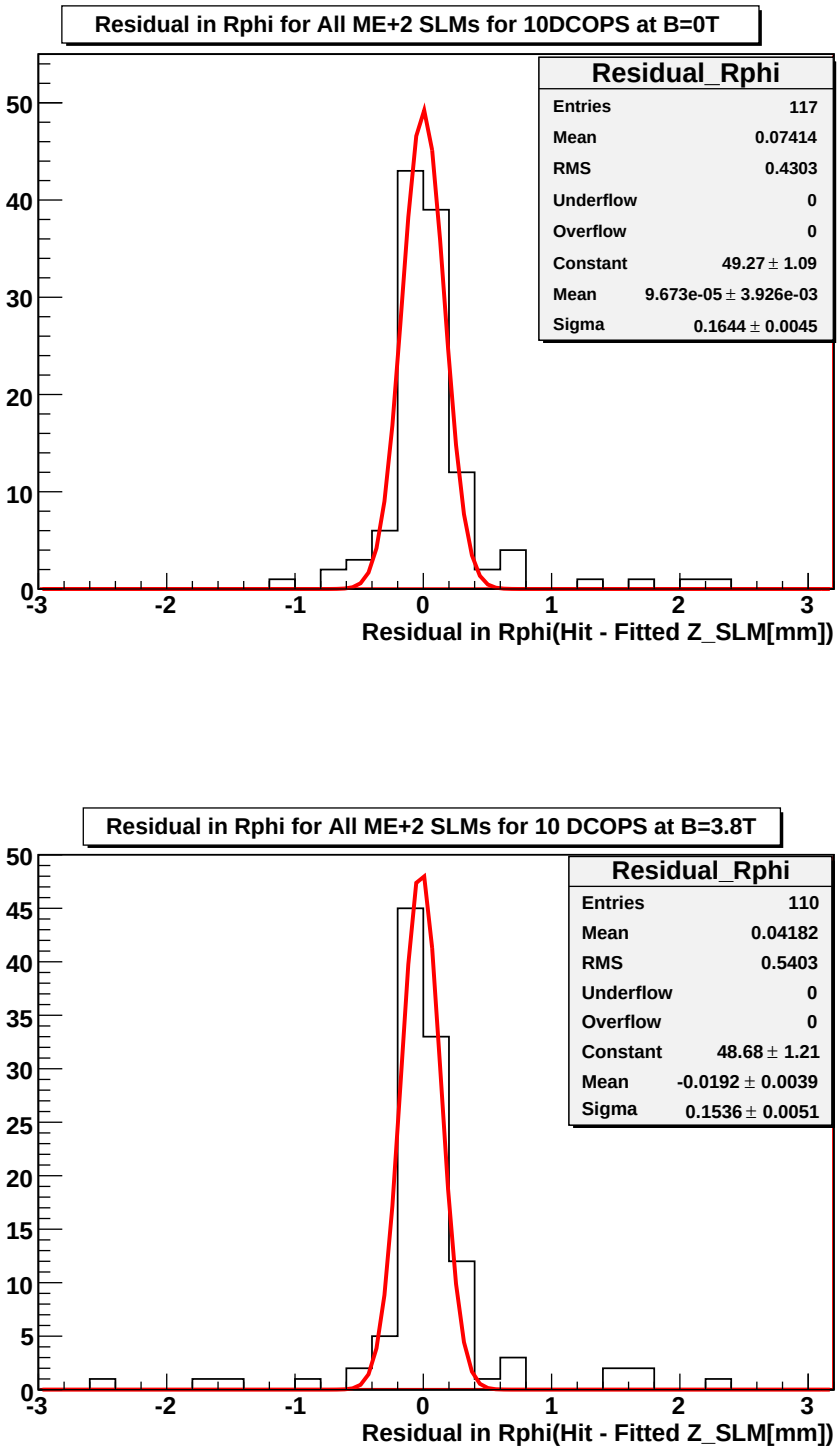

Figure 4.8: SLM fit residuals in rϕ for all the SLMs in ME+2 for the 10 DCOPS at B = 0 T(top) and at B = 3.8 T (bottom) fitted with a Gaussian.

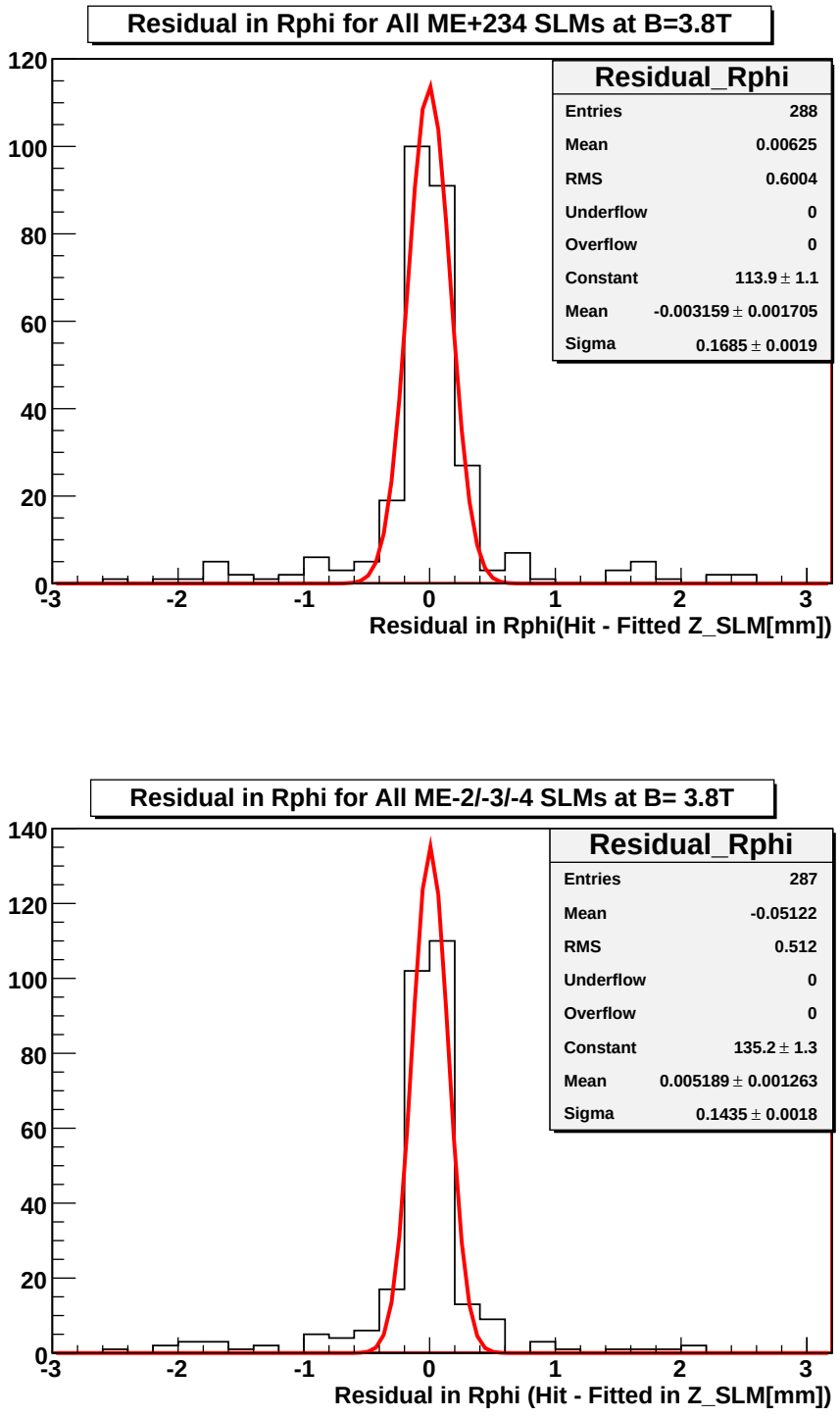

Figure 4.9: SLM fit residuals in rϕ for all the SLMs in ME+2,3,4 for the 10 DCOPS at B = 3.8 T (top) and for all the SLMs in ME-2,3,4 at B = 3.8 T (bottom) fitted with a Gaussian.

chambers, the constants are based on optical measurements with the ME DCOPS sensors. For the ME±1/1,2,3 chambers, the constants are based on measurements using the Link system sensors only. These coordinates have been successfully validated against track-based alignment with the 2010 beam halo data (closed rings ME+3/1, ME-3/1, ME-3/2 , ME-4/1). The absolute position of the CSC chambers in global X_{CMS},Y_{CMS} for ME± endcaps are summarized in Table 4.3 [55]. The average alignment correction with respect to nominal geometry are visualized in color plots as shown below.

CSCs	X_{CMS}[mm]	Y_{CMS}[mm]	CSCs	X_{CMS}[mm]	Y_{CMS}[mm]
MEp2/1/02	2200.40	1024.75	MEm2/1/02	2200.15	1024.38
MEp2/1/04	1026.30	2199.59	MEm2/1/04	1024.99	2199.82
MEp2/1/08	-1988.35	1392.17	MEm2/1/08	-1989.33	1391.19
MEp2/1/10	-2418.89	-210.79	MEm2/1/10	-2417.83	-212.41
MEp2/1/14	-211.52	-2417.88	MEm2/1/14	-210.71	-2417.9
MEp2/1/16	1392.41	-1987.9	MEm2/1/16	1390.93	-1989.71
MEp3/1/02	2291.21	1065.08	MEm3/1/02	2290.99	1066.49
MEp3/1/04	1068.63	2290.75	MEm3/1/04	1066.68	2290.75
MEp3/1/08	-2069.85	1450.04	MEm3/1/08	-2071.5	1448.33
MEp3/1/10	-2516.95	-221.61	MEm3/1/10	-2516.97	-223.10
MEp3/1/14	-220.57	-2517.7	MEm3/1/14	-220.12	-2517.57
MEp3/1/16	1449.37	-2070.41	MEm3/1/16	1448.97	-2070.7
MEp4/1/02	2381.28	1107.66	MEm4/1/02	2381.14	1107.58
MEp4/1/04	1110.71	2380.26	MEm4/1/04	1109.5	2382.44
MEp4/1/08	-2151.16	1506.86	MEm4/1/08	-2153.76	1504.42
MEp4/1/10	-2616.12	-230.74	MEm4/1/10	-2615.73	-232.00
MEp4/1/14	-229.69	-2616.32	MEm4/1/14	-228.9	-2617.41
MEp4/1/16	1506.12	-2151.9	MEm4/1/16	1506.38	-2151.59

Table 4.3: Absolute position of the inner CSCs in ME±2,3,4 disks [55].

4.7 Effect of muon misalignment on Z′ search

The limited knowledge about the exact positions and orientations of the silicon sensors in the CMS tracker is one of the largest potential sources for tracking uncertainties. Similarly, the alignment precision of the muon system limits the detection of the

CSCs	X_{CMS}[mm]	Y_{CMS}[mm]	CSCs	X_{CMS}[mm]	Y_{CMS}[mm]
MEp2/2/03	4947.71	1800.46	MEm2/2/03	4948.5	1797.38
MEp2/2/08	1801.13	4947.49	MEm2/2/08	1801.55	4947.50
MEp2/2/15	-4035.12	3382.41	MEm2/2/15	-4034.51	3383.09
MEp2/2/20	-5184.98	-914.03	MEm2/2/20	-5184.41	-916.52
MEp2/2/27	-914.69	-5184.91	MEm2/2/27	-913.75	-5185.32
MEp2/2/32	3382.42	-4035.25	MEm2/2/32	3383.41	-4034.21
MEp3/2/03	4948.03	1798.61	MEm3/2/03	4947.83	1799.57
MEp3/2/08	1801.96	4946.93	MEm3/2/08	1798.3	4948.43
MEp3/2/15	-4033.92	3383.6	MEm3/2/15	-4034.45	3383.16
MEp3/2/20	-5184.45	-916.95	MEm3/2/20	-5184.46	-916.52
MEp3/2/27	-915.41	-5184.75	MEm3/2/27	-912.17	-5185.69
MEp3/2/32	3383.88	-4033.72	MEm2/2/32	3383.41	-4034.21

Table 4.4: Absolute position of the outer CSCs in ME±2,3,4 disks [55].

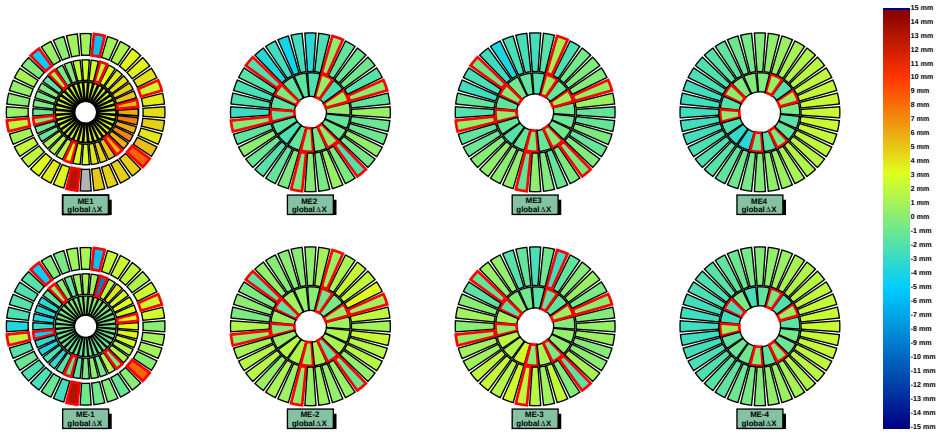

Figure 4.10: Visualization of the ME global-X alignment correction in rϕ relative to the nominal positions.

high momentum muons. In order to study the impact of these alignment uncertainties, it is necessary to estimate realistic displacements for the individual detector elements and also to set up a software environment which allows to systematic implementation of these misalignment effects in the track reconstruction.

In order to assess the impact of misalignment effects on the tracking, it is important to develop a consistent set of displacements and rotations for all tracking devices in

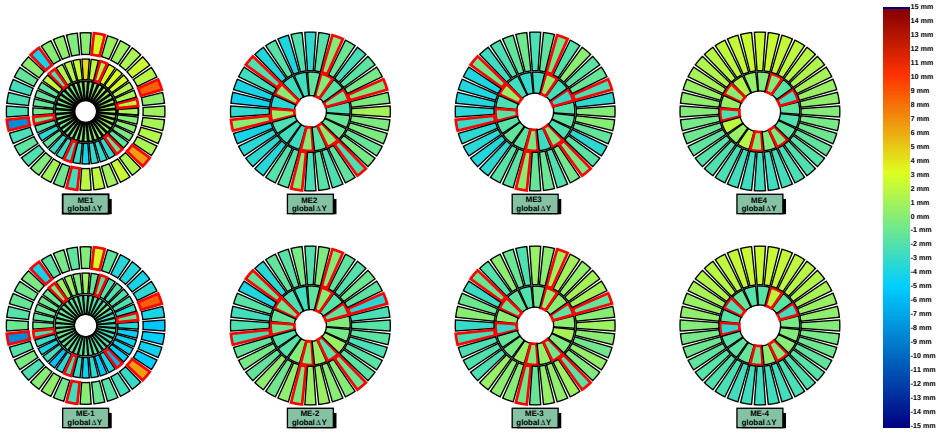

Figure 4.11: Visualization of the ME global-Y alignment correction in rϕ relative to the nominal positions.

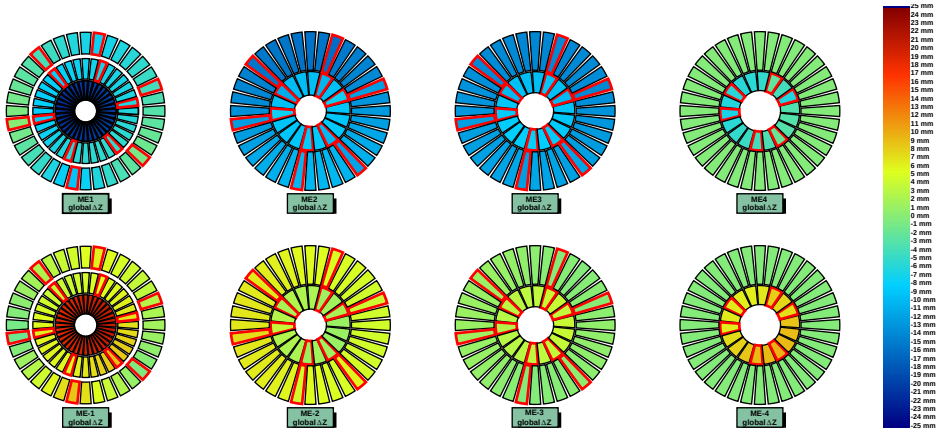

Figure 4.12: Visualization of the ME global-Z alignment correction in rϕ relative to the nominal positions.

the CMS, which perform as close as possible the alignment uncertainties expected during the data taking. It is necessary to ensure that the technical functionality of detector components for all tracking devices, for example, pixel detector; strip tracker; and muon chambers (DTs and CSCs), is assured. The combination of the technical functionality and realistic estimates of alignment uncertainties for the individual tracking devices is referred to as the misalignment scenario.

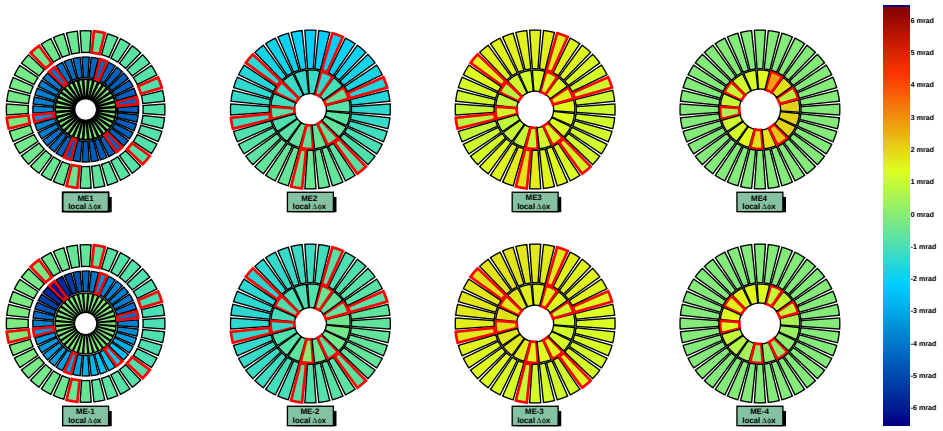

Figure 4.13: Visualization of the ME local-phiX alignment correction in rϕ relative to the nominal positions.

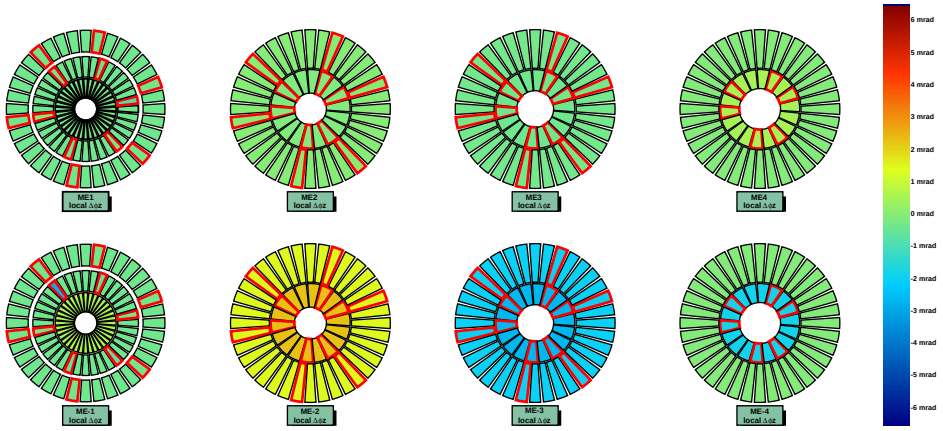

Figure 4.14: Visualization of the ME local-phiZ alignment correction in rϕ relative to the nominal positions.

The main element in the performance of high p_T muon reconstruction and, therefore, of the Z′ search, is the alignment of the tracker and the muon system. Unlike the muons in the region of low and moderate p_T values, where the influence of the tracker alignment is predominant, both the tracker alignment and the muon system alignment play an important role for the muons at TeV scale. We take them into account by using the two realistic misalignment scenarios developed in the CMS reconstruction: the"first

data" and the "long term". These scenarios; however, are only based on the current best estimates of expected alignment uncertainties and will be refined as better estimates from alignment studies become available.

The first scenario is supposed to describe the conditions expected at the initial stage of the data taking (First Data scenario), while the second one addresses the alignment uncertainties expected when the full alignment of the detector is done (Long Term scenario). All the physics studies are intended to be carried out with "First Data" or "Long Term" scenarios. In addition, the "Survey Only" scenario is provided for the muon system and describes the knowledge of detector positions before any alignment information is included. Therefore, it is intended to be used mainly for the debugging of the misalignment software and other technical tasks and not for physics studies; it is directly provided only for the muon system. We expect p_T resolution to be rather poor at the beginning of the data taking (First Data scenario) and improve substantially with time (Long Term scenario). As expected, misalignment of the muon system plays an important role only for high-p_T muons.

As discussed above, event in the worst case scenario, neither the trigger efficiency nor the offline reconstruction efficiency for high p_T muons is affected by the misalignment once the alignment position uncertainties are used in reconstruction algorithms [56]. Therefore, uncertainties in alignment translate mainly into uncertainties in the invariant mass resolution. Even sizable variations in the width of the mass resolution have only a small impact on the Z' mass reach. Another potentially important source of systematic uncertainties is the uncertainty in the calibration precision of the muon chambers. Uncertainties in the calibration of the CSCs are less critical and, hence, are expected to

have a negligible impact on the Z′ detection as well. The details of these studies can be found in [56, 57].

4.8 Summary

The ME alignment system has successfully recorded data during the year 2010. For the CSCs, all monitored chambers are aligned in X_{CMS},Y_{CMS}. An aligned detector geometry at B = 3.8 T is provided in the form of alignment constants which can be used for muon track reconstruction. The resolution for all ME+2,3,4 in rϕ is 168 μm and 143 μm for all ME-2,-3,-4. The systematic error associated with the reconstruction is estimated to be 116 μm for ME+2,3,4 and 149 μm for ME-2,-3,-4 from a comparison with PG. The alignment constants for the 2010 STARTUP is provided in SQlite database and is available at the CERN Analysis Facility (CAF) [55].

CHAPTER 5

Search for a Z' Using 7 TeV Collision Data of the 2011 Run

The LHC at CERN started pp collisions at $\sqrt{s} = 7$ TeV on March 14, 2011, after a first successful operation in 2010. The search for Z' decaying to dimuons in the data collected during 2010 has been published in [20,58], corresponding to an integrated luminosity of 40 pb^{-1}. In this chapter, we continue the search using the LHC collision data of the 2011 run at 7 TeV center-of-mass energy, collected by the CMS detector. The dataset corresponds to an integrated luminosity of 5.28 fb^{-1}.

5.1 Introduction

We conduct the search by selecting events in which there are good quality opposite-sign pairs of muon and by reconstructing the dimuon mass. The dominant, irreducible SM background from the DY process, together with the smaller, reducible backgrounds from $t\bar{t}$ and other SM processes, predict a rapidly falling mass spectrum above the Z peak. We perform a shape analysis on the measured spectrum to distinguish bumps (i.e. the resonance peak from new physics from the smoothly falling background). We use unbinned maximum likelihood fits to calculate the significance of any such bump and to set limits on the production cross section of Z' times branching

ratio into dimuons, scanning over a range of $M_{Z'}$, without making any assumptions on the absolute background rate.

5.2 Dataset and run selection

Our main analysis uses only the /SingleMu/ primary dataset, while cross checks on efficiencies and backgrounds relies on other datasets. We use the November-2011 reprocessing ("re-reco") of the full 2011 dataset, in which the main difference with respect to the prompt-reconstruction dataset ("prompt-reco") was an updated tracker alignment. Based on the instantaneous luminosity, the 2011 data taking period was divided into two sections, 2011A and 2011B.

In the CMS experiment, a data quality management (DQM) team certifies individual luminosity sections as being good or bad for the physics analysis. For each lumisection, the overall decision of good or bad for the physics analysis is composed of the individual decisions for each of the subdetectors (e.g. pixels, CSCs, HCAL) and reconstruction subsystems (e.g. tracking, muons, jets), determined by examining numerous histograms in comparison to reference histograms. Since our analysis looks for muons in the final states, validation requirements for calorimeters are not taken into account. Therefore, we use "MuonPhys" JSON files for the run and lumisection selection. In studies where electrons and other objects use the"Golden" JSON, ECAL/HCAL must be good.

When the re-reco JSONs were available, it was announced by the CMS Physics Object Group (POG) to use pixel luminosity measurements instead of the usual Forward Hadron Calorimeter (HF) luminosity measurements [59], because the HF luminosity system has distinct problems with the 2011 data. The total integrated luminosity of full

2011 dataset corresponds to 5.28 fb^{-1} using the pixel cluster counting method. Table 5.1 below shows the datasets used in this analysis with run ranges and corresponding luminosities.

Dataset	Run range	Int. Luminosity(pb^{-1})
/SingleMu/Run2011A-08Nov2011-v1/AOD	160404-163869	234
	165088-173198	1908
	173236-173692	274
/SingleMu/Run2011B-19Nov2011-v1/AOD	175832-180296	2864
Total (Run 2011A + Run 2011B)	160404-180296	5280

Table 5.1: Datasets used in this analysis with run ranges and corresponding luminosities.

5.3 Trigger requirements

The trigger used to select events for this analysis is an unprescaled single muon trigger with the lowest p_T threshold. Both the 2011A and 2011B muon datasets use a single muon trigger to select events both at the L1 and HLT. The relevant single muon HLT trigger paths for these run periods are HLT_Mu30, HLT_Mu40 and HLT_Mu40_eta2p1. As the names imply, the HLT_Mu30 and HLT_Mu40 triggers select events with muon p_T>30 GeV/c and p_T>40 GeV/c within $|\eta|$<2.1, respectively. The HLT_Mu40_eta2p1 is the same as the HLT_Mu40 except that the restriction on $|\eta|$ appears also at the L1 level. The corresponding L1 triggers select events at a lower p_T threshold, p_T>12 GeV/c for the the HLT_Mu30 and p_T> 16 GeV/c for the HLT_Mu40 and HLT_Mu40_eta2p1 (with an explicit cut of $|\eta|$<2.1). Table 5.2 summarizes the run ranges and HLT paths used in this analysis. In simulated samples where such a trigger path does not exist, or in earlier runs, we emulate the HLT_Mu40_eta2p1 decision using a lower p_T single muon

trigger (e.g. HLT_Mu16), requiring the HLT object that fired it (determined by the HLT filter name) to have $p_T > 40$ GeV and to be within $|\eta| < 2.1$.

Dataset	Run range	HLT path
Run 2011A	160404-163869	HLT_Mu30
	165088-173198	HLT_Mu40
	173236-173692	HLT_Mu40_eta2p1
Run 2011B	175832-180252	HLT_Mu40_eta2p1

Table 5.2: The 2011A and 2011B datasets used with run ranges and HLT paths.

Both the CMS software (CMSSW) and the trigger paths themselves changed in 2011. Therefore, we have done a basic check on the trigger efficiency as measured in simulation using the DY events where both muons are in acceptance (defined as one muon in the restricted pseudorapidity range $|\eta| < 2.1$, the other in $|\eta| < 2.4$, and both muons having $p_T > 45$ GeV), which is simulated in CMSSW_4_2_3. Figure 5.1 shows the single muon L1, HLT, and L1+HLT trigger efficiencies with respect to MC truth as a function of dimuon invariant mass. The total trigger efficiency is predicted to be at or above 98% for the entire range of dimuon masses under consideration.

5.4 Event, muon, and dimuon selection

For the full 2011 dataset, we kept all the requirements from the analysis done for the European Physical Society (EPS) meeting [60] except for the muon trigger acceptance and modification to muon track selection. We require that both muons pass a selection that is nearly the same as the tight selection used by the muon POG [61], as well as Vector Boson Task Force (VBTF) updated selection. To get a sample of pure dimuon events with high efficiency, we impose the following event selection mostly designed to remove beam/cosmic background events:

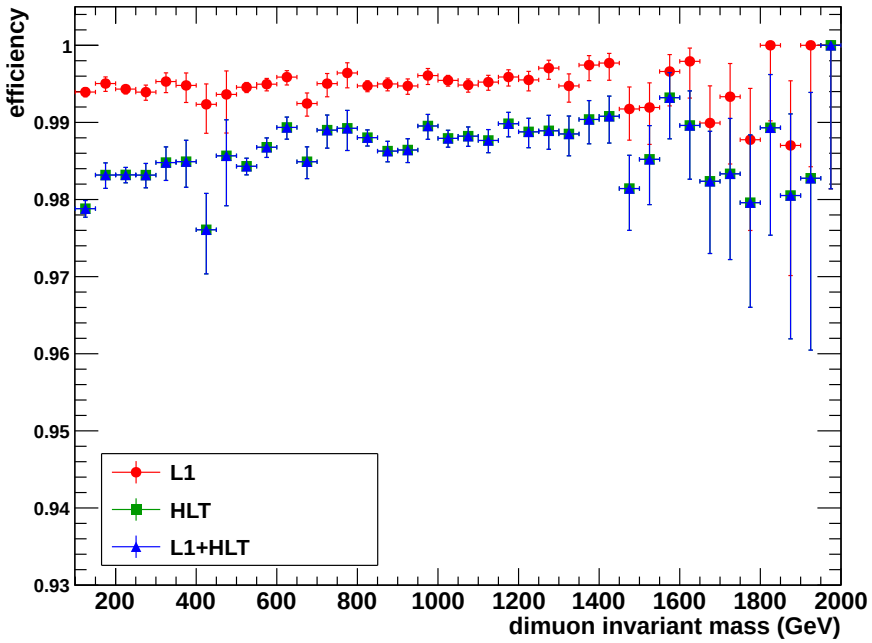

Figure 5.1: The efficiency of the L1 single muon path (L1 SingleMu12), the emulated HLT single muon path (HLT_Mu40_eta2p1), and the product of the two as a function of simulated dimuon invariant mass, as evaluated using CMSSW version 4_2_3 .

- In order to avoid events that are coming from beam backgrounds, events are required to have at least a quarter of the tracker tracks reconstructed in the inner tracker marked as high purity. The reconstructed tracks are filtered to remove fake tracks and to provide quality of remaining tracks. The filter uses information on the number of hits, the normalized χ^2 of the track, and the compatibility of the track originating from a pixel vertex. Tracks that pass the tightest selection are labeled as high purity.

- We require a good offline reconstructed primary vertex (PV) to be found in the event as defined by the tracking POG in CMS. A primary vertex is considered good, if it is associated with at least four tracks, and found within $|r| < 2$ cm and $|z| < 24$ cm, where r and z correspond to the radial and longitudinal distances from

the interaction point. This cut is particularly good at rejecting non-collision events in which there are very few tracks reconstructed where a track from a cosmic ray muon traverses near the interaction point giving a fake dimuon.

In order to reduce the rate of muons from decays-in-flight (muons coming from pion and kaon decays) and punch-through (secondary hadrons or muons, fake muons from a hadronic shower in the calorimeter that survive to reach the muon detector) and to ensure the quality of muon tracks, both muon candidates are required to pass the following selection criteria:

- The muon must be reconstructed as a global muon and a tracker muon.
- The muon must have $p_T > 45$ GeV/c, reconstructed offline.
- The global muon track fit must include at least one hit from each of the pixel and muon detector.
- The global muon track fit must have at least nine tracker layers with hits in the fit.
- The tracker muon track must have matched segments in at least two muon detector stations.
- The muon must have a transverse impact parameter $|d_{xy}| < 2$ mm with respect to the beam spot. This selection significantly reduces the rate of muons from decays-in-flight.

- The muon must pass a relative tracker-only isolation cut; the sum of the p_T of all tracks, excluding muons track must be less than 10% of the muons p_T. This supresses the muons from hadronic decays.

- At least one of the reconstructed muon candidates must be matched within $\Delta R < 0.2$ and $\Delta p_T/p_T < 1$ to the HLT muon candidate (trigger muon), which has a p_T threshold of 40 GeV/c and is restricted to the $|\eta| < 2.1$.

To form a dimuon, the two muons passing the above selection must further satisfy the following requirements:

- must have an opposite charge.

- must be consistent with originating from a common vertex. A constrained fit of the muon candidate tracks to a common vertex must satisfy $\chi^2 < 10$.

- The background from cosmic ray muons that pass close to the detector interaction point can appear as two muon candidates back-to-back in space faking a dimuon event. In addition to the impact parameter cut, we require the three dimensional angle between the two muon's momenta be less than π - 0.02 radian in order to suppress it.

In events with more than one opposite-sign dimuon, we keep only the one with the highest invariant mass. We perform a common-vertex fit using the Kalman filter formulation as implemented in CMSSW [62] in order to compute the kinematics of the dimuon system particularly its mass. This also serves to ensure that the two muons originate from the same vertex as a guard against pileup and as a check on reconstruction quality; we explicitly require that the vertex fit has $\chi^2 < 10$.

Muons are fundamentally measured in q/p_T so there might be a possibility of charge misidentification, which could make the q/p_T measurement wrong. The rate of muon charge misidentification is known [47] to be below 0.5% for muons with p_T up to 300 GeV, the requirement for opposite-sign dimuons is still highly efficient. So as a quality cut, we do not use the same sign events in our final selection; however, we use it as a control sample.

For this analysis, instead of cutting on the number of silicon tracker hits in the muon track fit, we cut on the number of tracker layers. This cut is part of an updated set of CMS muon POG recommendations and was introduced to protect against muons mismeasured due to an insufficient lever arm in the tracker. Cutting on layers is more effective at promoting longer tracks than cutting on hits because a single layer of the tracker can contribute more than one hit to the fit at a given radius.

The muon POG studied the efficiency of the tight muon identification [61]. Using Tag and Probe method with muons from the Z peak and tracks in the silicon inner tracker as probes, the efficiency is measured to be $96.4\% \pm 0.2\%$ in the barrel and $96.0\% \pm 0.3\%$ in the endcap with scale factors between data and the simulation of 0.999 ± 0.003, and 0.983 ± 0.005 respectively. The efficiency to reconstruct tracks in the silicon inner tracker was measured separately and found to be 99% or higher in the whole acceptance range, which is in good agreement with the simulation.

5.5 The effect of pileup on muon isolation

Our selected muons are required to be isolated to reject background from misidentified muons from jets, and non-prompt muons from hadron decays. For the 2011 data, the average number of pileup events is larger, which could decrease the signal efficiency.

Pileup interactions lead to more reconstructed charged tracks and more energy deposited in the calorimeters for each primary interaction. As our isolation requirement is loose (relative cut on the "tracker-only isolation"), only the former is relevant to our analysis. To cross check that we are robust against these effects, we examine the distributions of the relative "tracker-only isolation" as a function of the number of reconstructed primary vertices. We also examine the behavior of a "tracker-plus-calorimeters" isolation variable. For otherwise selected muons from dimuons on the Z peak (i.e. those with mass reconstructed in the range $60 < m < 120$ GeV), Figure 5.2 shows the fraction of muons that fail a cut on the "tracker-only" and "tracker-plus-calorimeters" relative isolation variables at thresholds of 10% and 15%, respectively, as a function of the number of reconstructed primary vertices. Using muons from Z decays helps to remove muons that are not originally isolated; in the mass range selected, the expectation from simulation is that fewer than 0.3% of dimuons are from processes other than $Z \to \mu\mu$.

As a function of dimuon invariant mass, Figure 5.3 shows the combined reconstruction and selection efficiency for dimuons passing the above cuts with respect to triggered events in acceptance (both muons in $|\eta| < 2.4$ and having $p_T > 45$ GeV), all events in acceptance, and the total acceptance times efficiency. The study was performed on simulated DY events using CMSSW version 4_2_3 with global tag START42_V11. The Z peak has been cut away by the online and offline p_T thresholds, while above the Z peak, most of the total inefficiency at low dimuon invariant masses is due to the geometrical acceptance. The total dimuon reconstruction efficiency including acceptance is above 76% for masses above 600 GeV and is about 82% at 1 TeV.

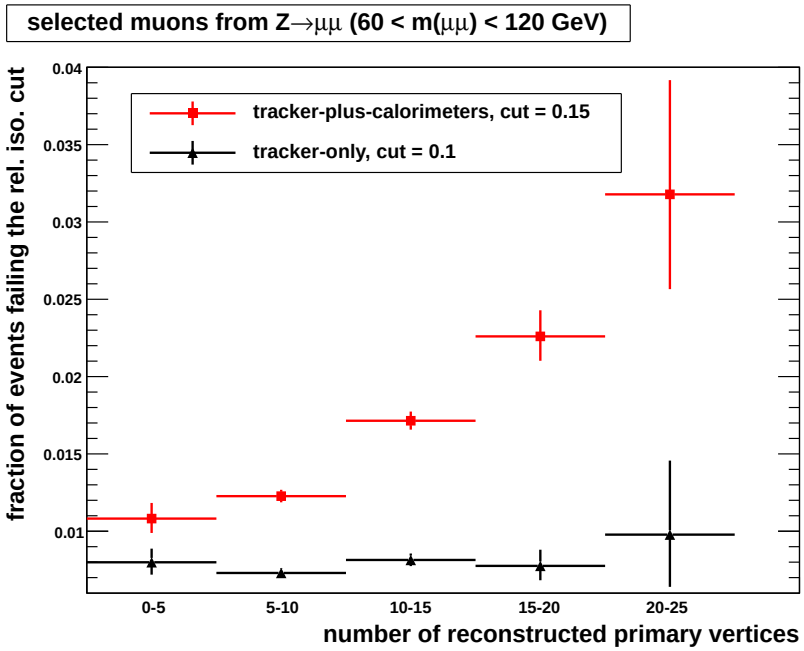

Figure 5.2: From dimuons on the Z peak ($60 < m < 120$ GeV), the fraction of muons otherwise selected using our analysis cuts that fail a cut on the "tracker-only" relative isolation at 10% (black triangles) or a cut on the "tracker-plus- calorimeters" relative isolation at 15% (red squares), as a function of the number of reconstructed primary vertices.

5.6 Data/MC comparisons

In this section, we compare distributions of analysis related variables between the data and the prediction from MC simulation of the contributing SM processes, focusing especially on the dimuon mass spectrum where we expect a signal from new physics. Simulated event samples for the signal and background processes were generated with PYTHIA, MADGRAPH and POWHEG event generators. The MADGRAPH [63] was used for $t\bar{t}$ and W+ jets samples and the POWHEG V1.1 framework [64–66] for DY to muons and single top samples. Both of these were interfaced with the PYTHIA V6.424 (using the Z2 tune) [67] parton shower generator. All other processes were generated using PYTHIA. The CTEQ6L1 [68] parton distribution function (PDF) set was used

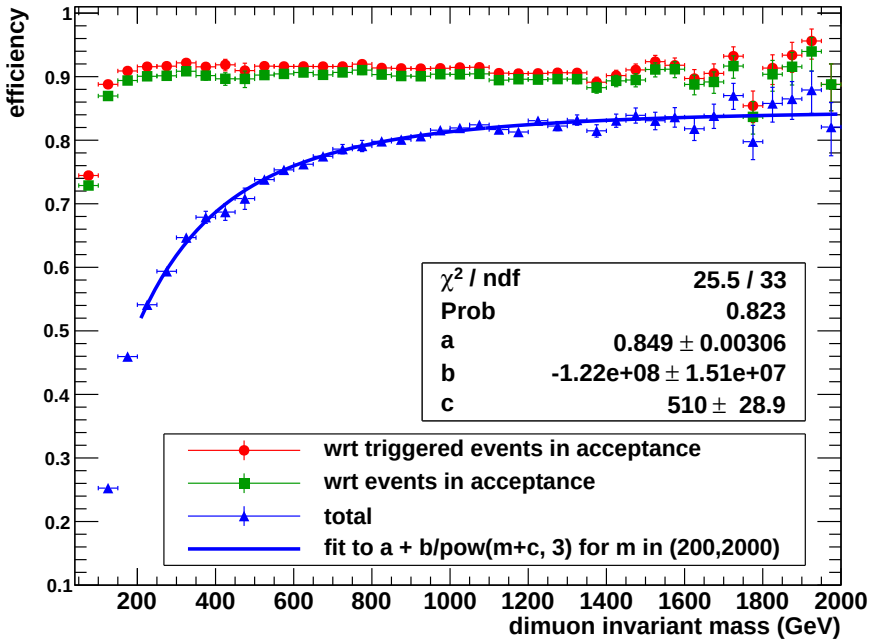

Figure 5.3: The efficiency for dimuons passing our selection with respect to "triggered events in acceptance", with respect to "events in acceptance", and the "total acceptance times efficiency", as a function of inavariant mass as evaluated on simulated DY events using CMSSW_4_2_3 with global tag START42_V11. The solid blue curve is a fit to the "total acceptance times efficiency" in the dimuon mass range, from 200 to 2000 GeV.

for all samples except the DY where the CT10 [69] set was used. The response of the detector was simulated in detail using GEANT4 [70].

Table 5.3 lists the generators PYTHIA, POWHEG, and MADGRAPH, physics processes, kinematic cuts, cross sections, number of events for the various signal and background samples produced with MC simulation that are used in this analysis. The various background samples are combined using the information in this table to produce the overall prediction from simulation. Table 5.4 lists the datasets used in the MC simulation of the signal and background processes considered. In this section, we present dimuon invariant mass spectrum using 4.9 fb^{-1} of data before the re-reconstructed JSON available and 5.28 fb^{-1} of data with the re-reconstructed JSON. The distribution from each simulated sample is relatively scaled by weights derived from the information in

Table 5.3; the entire summed distribution is then scaled to the data using the number of events found in the window of $60 < m < 120$ GeV around the Z peak.

Process	Program	Generation parameter	σ (pb)	Events
$Z' \to \mu^+\mu^-$, SSM	PYTHIA	M = 750 GeV	0.3473	20400
		M = 1000 GeV	0.08922	20238
	-	M = 1250 GeV	0.02781	20088
		M = 1500 GeV	0.009643	20412
		M = 1750 GeV	0.003649	20758
$DY \to \mu^+\mu^-$	PYTHIA	$M_{\mu\mu} > 20$ GeV	1631	2148325
		$M_{\mu\mu} > 120$ GeV	7.9	54550
		$M_{\mu\mu} > 200$ GeV	0.97	55000
		$M_{\mu\mu} > 500$ GeV	0.027	55000
		$M_{\mu\mu} > 800$ GeV	0.0031	55000
		$M_{\mu\mu} > 1000$ GeV	9.7×10^{-4}	55000
$DY \to \tau^+\tau^-$	PYTHIA	$M_{\tau^+\tau^-} > 20$ GeV	1631	2032536
$t\bar{t}$	MADGRAPH	—	157	3701947
tW	POWHEG	—	7.9	814390
$\bar{t}$W	POWHEG	—	7.9	809984
WW	PYTHIA	—	43	4225916
WZ	PYTHIA	—	18	4265243
ZZ	PYTHIA	—	5.9	4187885
W+jets	MADGRAPH	—	2.8×10^4	15110974
Inclusive-μ QCD	PYTHIA	$\hat{p}_T > 20$ GeV, $\lvert\eta(\mu)\rvert < 2.5$, $p_T(\mu) > 15$ GeV	8.5×10^{-4}	20416038

Table 5.3: Summary of analyzed MC samples for the various signal and background processes.

Figure 5.4 shows the dimuon mass spectrum as observed in data overlaid on the summed prediction from simulation with the various background processes separated into three main categories. As an example of the signal for which we are searching, the shape of a Z'_{SSM} with mass M = 1 TeV is also overlaid. Figure 5.5 shows the cumulative distributions for data and simulation, the value in each bin being equal to the number of events having that mass or greater. Table 5.5 summarizes the dimuon event counts for both data and simulation for both the control region $120 < M_{\mu\mu} < 200$ GeV and the search region $M_{\mu\mu} > 200$ GeV. The uncertainties listed for the simulation include both statistical and systematic components.

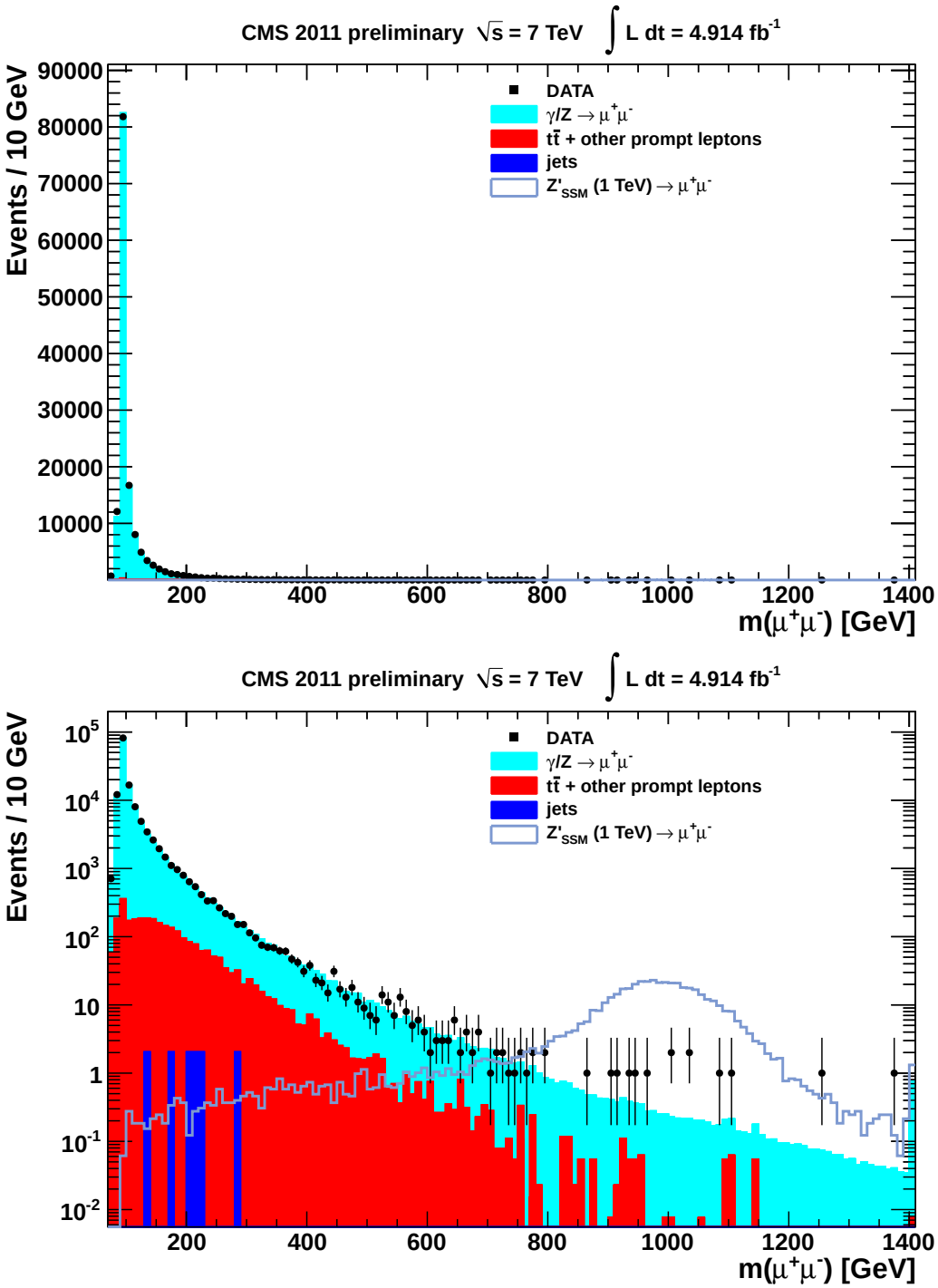

Figure 5.4: The observed opposite-sign dimuon invariant mass spectrum, overlaid on the summed prediction from simulation, in both linear (top) and log (bottom) scale. Other prompt leptons includes the contributions from $Z \to \tau\tau$, the diboson processes WW, WZ, and ZZ, and single top (tW). Jets includes contributions from QCD multi-jets and W+jets. As an example of the signal shape for which we are searching, the signal from a Z'_{SSM} of mass M = 1 TeV is also overlaid.

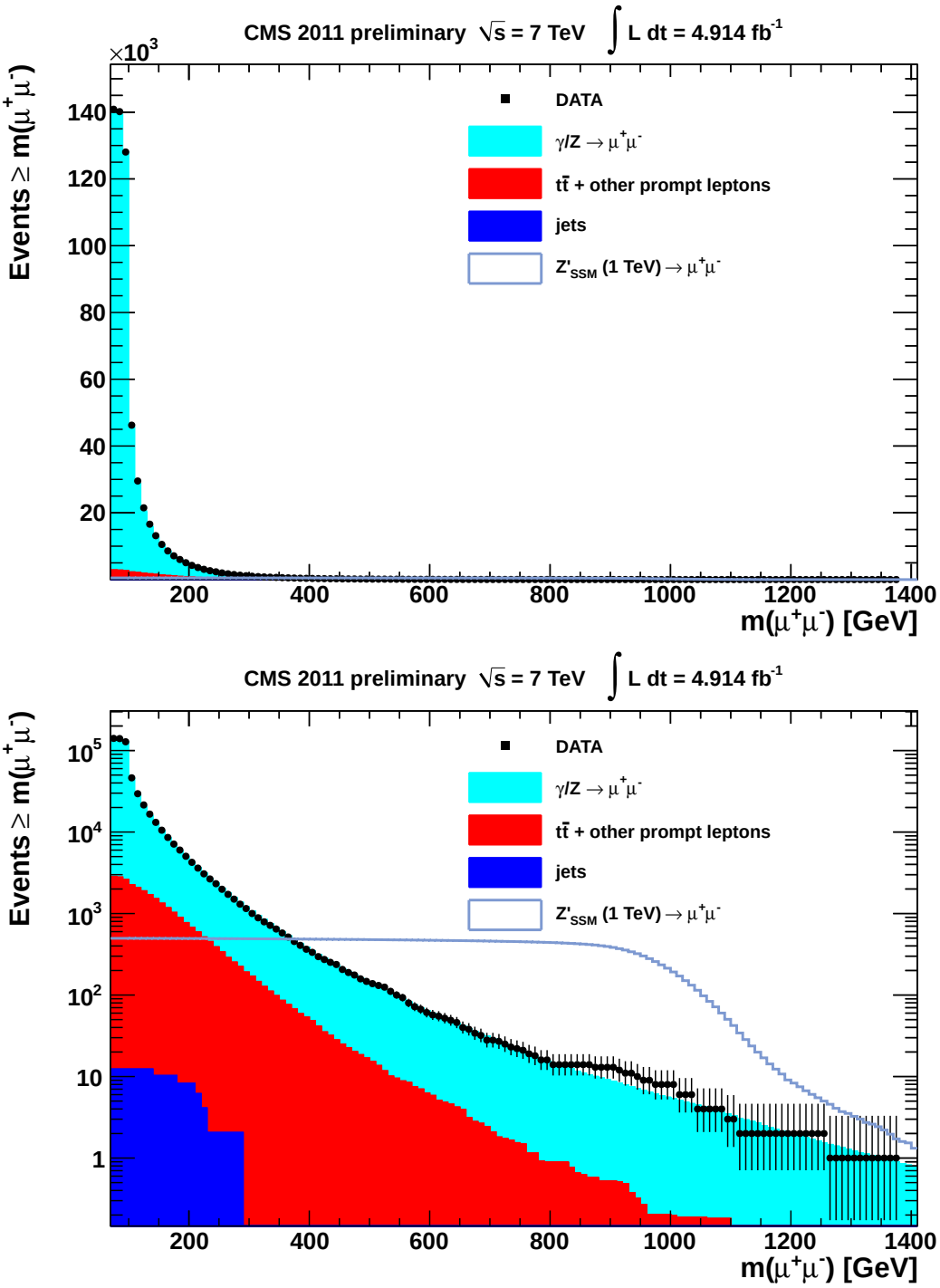

Figure 5.5: Number of opposite-sign dimuons with invariant mass greater than the given value, overlaid on the summed prediction from simulation, in both linear (top) and log scale (bottom). Other prompt leptons includes the contributions from $Z \to \tau\tau$, the diboson processes WW, WZ, and ZZ, and single top (tW). Jets includes contributions from QCD multi-jets and W+jets.

Process	Dataset path
$Z' \to \mu^+\mu^-$, SSM	/ZprimeSSMToMuMu_M-750_TuneZ2_7TeV-pythia6/Summer11-PU_S4_START42_V11-v1
	/ZprimeSSMToMuMu_M-1000_TuneZ2_7TeV-pythia6/Summer11-PU_S4_START42_V11-v1
	/ZprimeSSMToMuMu_M-1250_TuneZ2_7TeV-pythia6/Summer11-PU_S4_START42_V11-v1
	/ZprimeSSMToMuMu_M-1500_TuneZ2_7TeV-pythia6/Summer11-PU_S4_START42_V11-v1
	/ZprimeSSMToMuMu_M-1750_TuneZ2_7TeV-pythia6/Summer11-PU_S4_START42_V11-v1
$DY \to \mu^+\mu^-$	/DYToMuMu_M-20_TuneZ2_7TeV-pythia6/Summer11- PU_S3_START42_V11-v2
	/DYToMuMu_M-120_TuneZ2_7TeV-pythia6-tauola/Summer11-PU_S3_START42_V11-v2
	/DYToMuMu_M-200_TuneZ2_7TeV-pythia6-tauola/Summer11-PU_S3_START42_V11-v2
	/DYToMuMu_M-500_TuneZ2_7TeV-pythia6-tauola/Summer11-PU_S3_START42_V11-v2
	/DYToMuMu_M-800_TuneZ2_7TeV-pythia6-tauola/Summer11-PU_S3_START42_V11-v2
	/DYToMuMu_M-1000_TuneZ2_7TeV-pythia6-tauola/Summer11-PU_S3_START42_V11-v2
$DY \to \tau^+\tau^-$	/DYToTauTau_M-20_TuneZ2_7TeV-pythia6-tauola/Summer11-PU_S3_START42_V11-v2
$t\bar{t}$	/TTJets_TuneZ2_7TeV-madgraph-tauola/Summer11-PU_S4_START42_V11-v1
tW	/T_TuneZ2_tW-channel-DR_7TeV-powheg-taola/Summer11-PU_S4_START42_V11-v1
$\bar{t}W$	/Tbar_TuneZ2_tW-channel-DR_7TeV-powheg-taola/Summer11-PU_S4_START42_V11-v1
WW	/WW_TuneZ2_7TeV_pythia6_tauola/Summer11-PU_S4_START42_V11-v1
WZ	/WZ_TuneZ2_7TeV_pythia6_tauola/Summer11-PU_S4_START42_V11-v1
ZZ	/ZZ_TuneZ2_7TeV_pythia6_tauola/Summer11-PU_S4_START42_V11-v1
W+jets	/WJetsToLNu_TuneZ2_7TeV-madgraph-tauola/Summer11-PU_S4_START42_V11-v1
Inclusive-μ QCD	/QCD_Pt-20_MuEnrichedPt-15_TuneZ2_7TeV-pythia6/Summer11-PU_S4_START42_V11-v1

Table 5.4: Dataset paths for the Summer 2011 simulated background samples in Table 5.3.

Source	Number of events	
	$120 - 200$ GeV	> 200 GeV
CMS data	17240	4250
Total background	16272 ± 739	4266 ± 185
Z^0/γ^*	15055 ± 726	3591 ± 170
$t\bar{t}$+other prompt leptons	1213 ± 145	667 ± 80
Multi-jet events	4 ± 3	8 ± 4

Table 5.5: Number of dimuon events with invariant mass in the control region 120-200 GeV and in the search region M > 200 GeV. The total background is the sum of the SM processes listed. The MC yields are normalized to the expected cross sections. Uncertainties include both statistical and systematic components added in quadrature.

The dimuon mass spectrum shown above at 4.9 fb^{-1} uses the simulated samples from the Summer 2011 as shown in Table 5.3. In the same year, another set of simulated samples for the backgrounds (Fall 2011) were also available. Those set of samples from the Fall 2011 run was also used in this analysis to generate dimuon mass spectrum. The main difference between the summer and fall 2011 samples was the number of events in

the DY and $t\bar{t}$ samples, which are the main backgrounds of our analysis. The Fall 2011 DY sample at M > 20 was generated with POWHEG, where as Summer 2011 DY sample was generated with PYTHIA. Table 5.6 shows the datasets used in the MC simulation of the signal and background processes considered for the analysis of full 5.28 fb^{-1} data. Figure 5.6 shows the dimuon mass spectrum overlaid on the summed distribution of simulated background samples and Figure 5.7 shows the cumulative distribution for the same set of data and background samples.

Process	Dataset path
$Z' \to \mu^+\mu^-$, SSM	/ZprimeSSMToMuMu_M-1000_TuneZ2_7TeV-pythia6/Fall11-PU_S6_START44_V9B-v1
DY $\to \mu^+\mu^-$	/DYToMuMu_M-20_CT10_TuneZ2_7TeV-powheg-pythia/Fall11- PU_S6_START44_V9B-v1
	/DYToMuMu_M-120_TuneZ2_7TeV-pythia6-tauola/Fall11- PU_S6_START44_V9B-v1
	/DYToMuMu_M-200_TuneZ2_7TeV-pythia6-tauola/Fall11- PU_S6_START44_V9B-v1
	/DYToMuMu_M-500_TuneZ2_7TeV-pythia6-tauola/Fall11- PU_S6_START44_V9B-v1
	/DYToMuMu_M-800_TuneZ2_7TeV-pythia6-tauola/Fall11- PU_S6_START44_V9B-v1
	/DYToMuMu_M-1000_TuneZ2_7TeV-pythia6-tauola/Fall11- PU_S6_START44_V9B-v1
DY $\to \tau^+\tau^-$	/DYToTauTau_M-20_TuneZ2_7TeV-pythia6-tauola/Fall11- PU_S6_START44_V9B-v1
$t\bar{t}$	/TTJets_TuneZ2_7TeV-madgraph-tauola/Fall11-PU_S6_START44_V9B-v1
tW	/T_TuneZ2_tW-channel-DR_7TeV-powheg-taola/Fall11-PU_S6_START44_V9B-v1
$\bar{t}W$	/Tbar_TuneZ2_tW-channel-DR_7TeV-powheg-taola/Fall11-PU_S6_START44_V9B-v1
WW	/WW_TuneZ2_7TeV_pythia6_tauola/Fall11-PU_S6_START44_V9B-v1
WZ	/WZ_TuneZ2_7TeV_pythia6_tauola/Fall11-PU_S6_START44_V9B-v1
ZZ	/ZZ_TuneZ2_7TeV_pythia6_tauola/Fall11-PU_S6_START44_V9B-v1
W+jets	/WJetsToLNu_TuneZ2_7TeV-madgraph-tauola/Fall11-PU_S6_START44_V9B-v1
Inclusive-μ QCD	/QCD_Pt-20_MuEnrichedPt-15_TuneZ2_7TeV-pythia6/Fall11-PU_S6_START44_V9B-v1

Table 5.6: Dataset paths for the Fall 2011 simulated background samples.

5.7 Background estimation

The largest background for the search of Z' in our analysis is from the DY process, which is an irreducible background. After the DY, the next largest background is from $t\bar{t}$ decays. Most $t\bar{t}$ decays, which end in our selection are events in which both W bosons decay leptonically. Besides this decay, it is also possible that one of the muons is from the leptonic decay and the other muon is from one of the jets, the b-jet. The samples in Table 5.3 allow us to obtain estimates of expected relative background rates

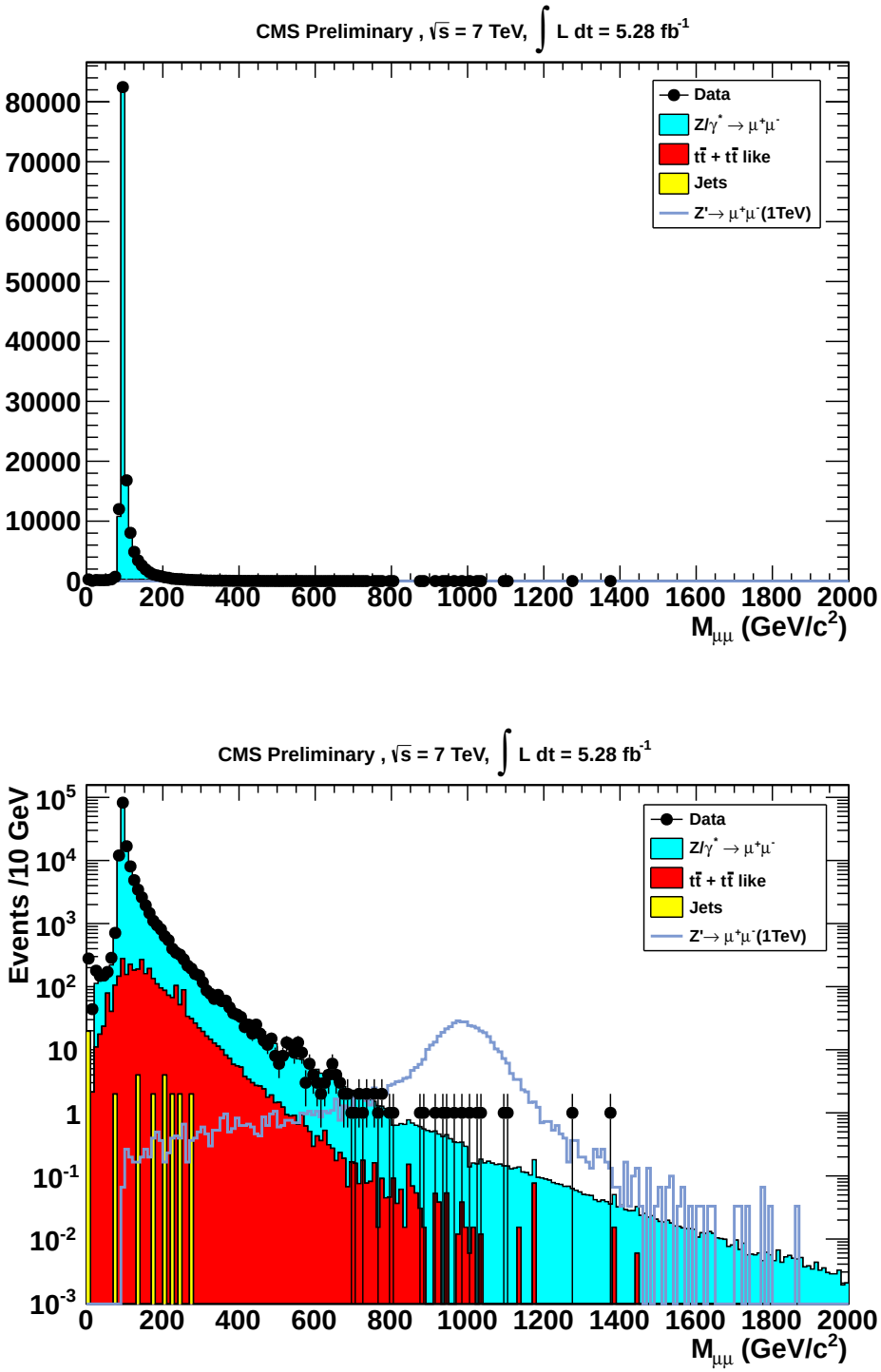

Figure 5.6: The observed opposite-sign dimuon invariant mass spectrum, overlaid on the summed prediction from simulation, in both linear (top) and log (bottom) scale. Other prompt leptons includes the contributions from $Z \to \tau\tau$, the diboson processes WW, WZ, and ZZ, and single top (tW). Jets includes contributions from QCD multi-jets and W+jets.

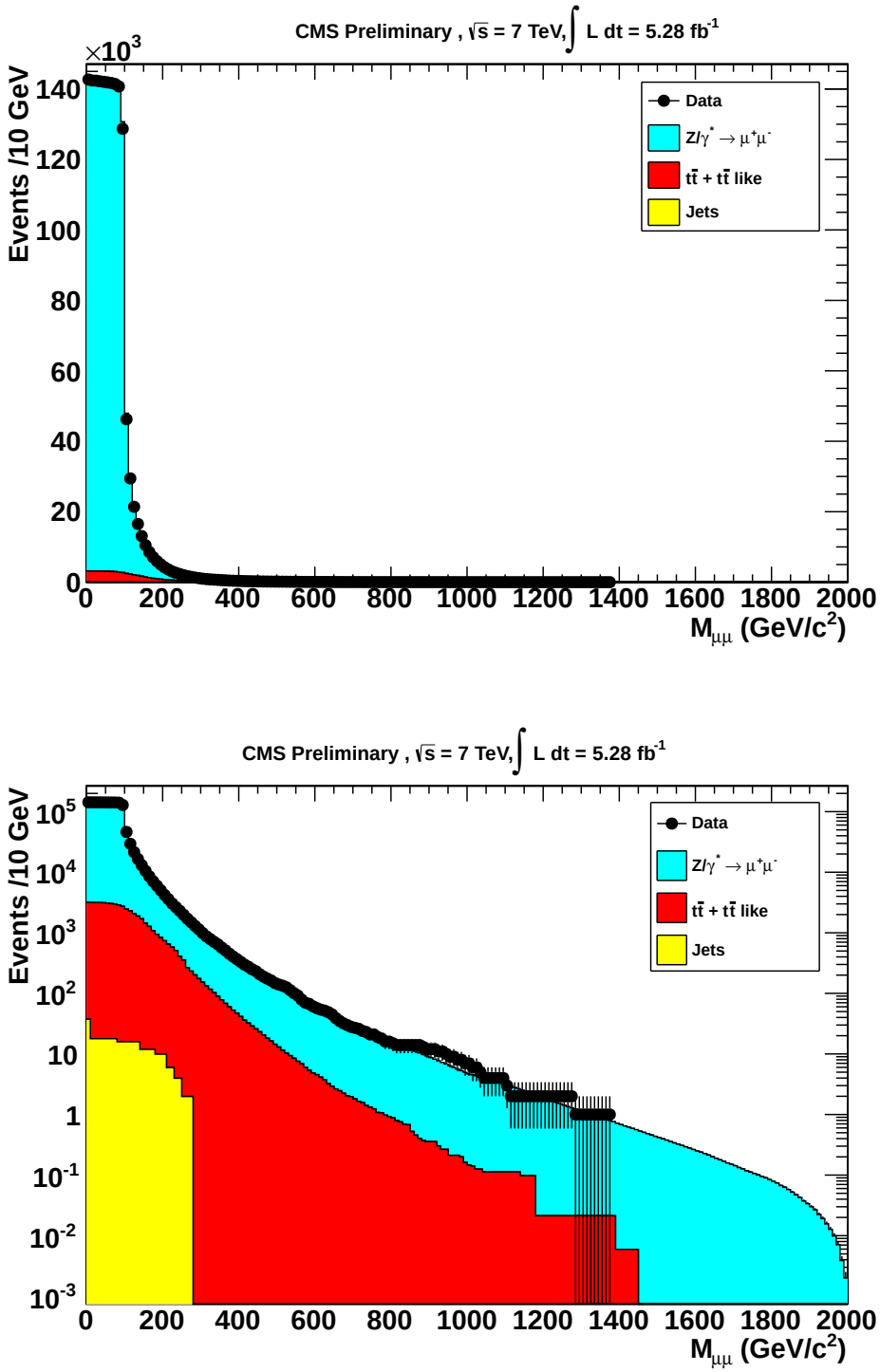

Figure 5.7: Number of opposite-sign dimuons with invariant mass greater than the given value, overlaid on the summed prediction from simulation, in both linear (top) and log scale (bottom).

for different processes. The $t\bar{t}$ background rate is found to be about 11% of the DY rate for $M_{\mu\mu} > 200 GeV/c^2$ (the DY prediction is based on NLO simulation). Other processes that are $t\bar{t}$ like, which contribute another 5% are also a source of prompt muons where most of the time both the muons appear to come from the same vertex and are associated with heavy flavor decay (e.g. single top (tW), dibosons, $Z \to \tau^+\tau^-$). Dimuons in which one or more muon is misidentified and contribute less than 1% are a non-prompt source of muons from heavy flavor decay or hadronic punch-through, and associated with jet activity (e.g. W+jets, QCD processes). Another type of background are dimuons coming from cosmic ray muons traversing the detector near the interaction point, which is coincident with a collision event that pass our primary vertex requirement and can be reconstructed as pair of opposite-sign muons. We perform data-driven estimates of the rate and shapes of these non DY backgrounds especially for $t\bar{t}$ and other source of prompt muons and for the QCD processes and cosmic ray muons that are difficult to estimate using simulation. We have considered the following methods to estimate the non-DY backgrounds:

- Source of prompt muons (including $t\bar{t}$): the "eμ method" in which the dimuon spectrum in the data is estimated starting from the electron muon dilepton spectrum as pioneered in CMS by the High Energy Electron Pair (HEEP) group [71].

- Source of non-prompt (misidentified muons): check the agreement between the data and MC for charge symmetric backgrounds by looking at the same sign dimuon spectrum.

- QCD background: use the probability for a muon to be isolated to re-weight the mass spectrum of anti-isolated dimuons.

- Dimuons from cosmic ray events: estimate the contamination from cosmic ray muons faking muon pairs by looking at events rejected with the transverse impact parameter cut. These methods for estimating the background from the data are described in detail in [58].

5.8 Normalization to Z resonance

We count events in the mass range of 60-120 GeV and perform background subtraction using the event counts from non- Z simulated samples rescaled by the data/simulation scale factor on the peak. As the single muon trigger and offline thresholds have been raised to $p_T = 40$ and 45 GeV, most of the Z peak normalization window has been cut away. We use a prescaled trigger path HLT_Mu15 with corresponding offline p_T threshold at 20 GeV to record Z events with selection otherwise identical to our primary one (restricting the HLT_Mu15 trigger acceptance to $|\eta| < 2.1$). As Mu15 was prescaled by various factors over the running period, we throw random numbers to achieve an overall prescale factor of 2000. By doing so, we found 680 events in the Z mass window in the data. Given the estimated total efficiency in this mass range of about 0.27, this is consistent with the theoretical cross section and the value measured by VBTF.

The dominant uncertainty on the ratio of the geometrical acceptances and other related theoretical considerations is for the Z because the acceptance of the Z is much smaller than at high mass. Therefore, we assign a systematic uncertainty of 2 % following the VBTF study [72] and as discussed in the 2010 analysis note [58]. The evolution of

the triggering and reconstruction efficiency from the Z peak to higher masses is taken from the simulation as in 2010. The overall variation in the efficiency ratio due to the increasing probability of muons showering is of the order of 2%, which we consider as the systematic uncertainty on the ratio of efficiencies. Considering the sources discussed above, we assign an overall normalization related systematic uncertainty of 3%.

5.9 Background shape and fitting

As discussed in Section 5.7, the dominant background comes from the DY process. The rest of the backgrounds have a rate of about 10 % of the DY. In the peak search and in setting limits, we only consider the background shape of dimuons from the DY. For use in the calculations, we parameterize the smoothly falling background by a function of the form:

$$P(m \mid a, b)_{\mathrm{DY}} = \exp{(am)} m^b \tag{5.1}$$

We parameterize the shape of the dimuon spectrum from the DY background using the function given in Equation 5.1 . The parameters of the background shape are determined by fitting the functions to the fully reconstructed DY dimuon mass spectrum as shown in Figure 5.8. We perform the fit in the mass range 200-2500 GeV. The fitted parameters we obtained are a = - 0.002423 and b = - 3.625.

Adding another exponentially falling shape has a similar effect on the high mass tail as it varies the shape parameters. By including another shape to represent the rest of the backgrounds mostly from $t\bar{t}$, and examining the impact on the result of the search and the limits set as a function of the $t\bar{t}$ contribution relative to the DY, we find less than 1% difference in the results. We, therefore, neglected the smaller backgrounds by

only using the DY shape.

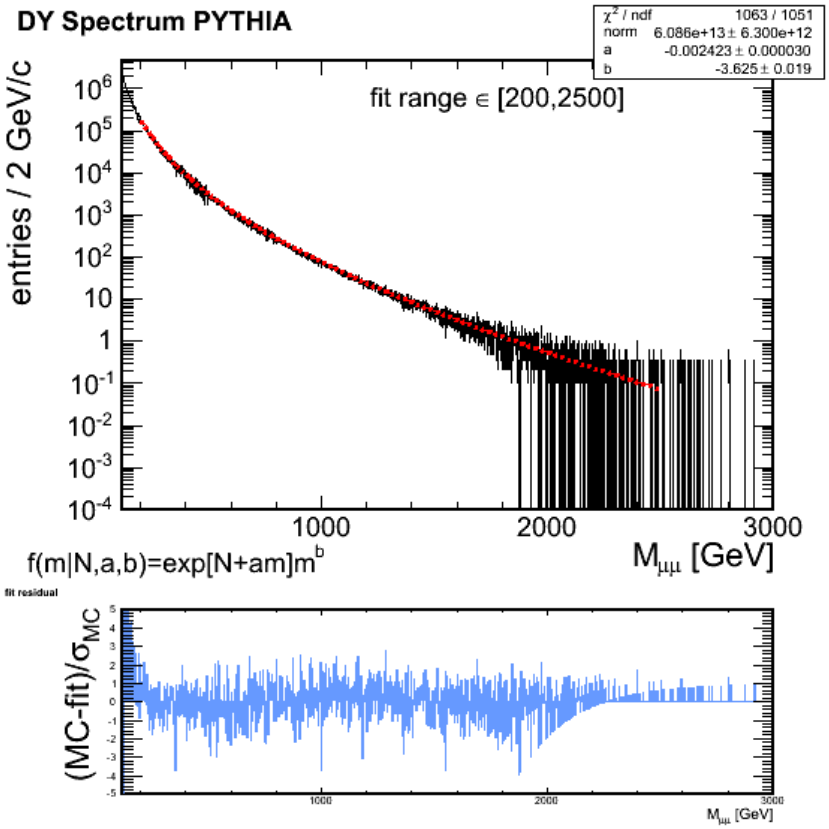

Figure 5.8: Fit to the simulated DY dimuon mass spectrum with residuals [73].

5.10 Statistical interpretation

5.10.1 Input to limit setting

The observed invariant mass spectra agree with expectations based on SM processes. We do not see any significant excess in our invariant mass spectrum; limits are set on the possible contributions from narrow resonances. In order to set limits, the background shape, the signal acceptance times efficiency and the mass resolutions are parameterized as a function of mass. The input to the limit setting tool is summarized in Table 5.7.

Input	Value
N_Z in 60-120 GeV from prescaled trigger	680
Z^0 acc.×eff. in 60-120 GeV, divided by prescale factor	0.27/2000
Z'acc. × eff./Z^0acc. × eff.uncert.	3%
N_{bkg} 200-2500 GeV	4250
Z'acc. × eff.	$0.85 - 1.2 \times 10^8/(m+510)^3$
mass resolution	$0.009332 + 5.71 \times 10^{-5} m - 1.171 \times 10^{-9} m^2$
background shape	$\exp(-0.002423\ m) \cdot m^{-3.625}$

Table 5.7: The input parameters to the limit setting code. Masses m are in GeV.

5.10.2 Systematics

The uncertainty on the DY background results from the uncertainty of evolution of Data/MC efficiency scale factor with energy, NLO effects and PDF uncertainties. The NLO uncertainty is taken to be 6% from the 2010 analysis. The PDF uncertainties vary from 4% at 400 GeV to 16% at 1.5 TeV, and 20% at 2 TeV. However, by the time the PDF uncertainty becomes large, the DY background is already well below an event so a 20% uncertainty will have little effect on the limits. Therefore, an average uncertainty of 10% was taken. The $t\bar{t}$ background has a 15% uncertainty due to the uncertainty on the $t\bar{t}$ cross section. The uncertainties were summed together and rounded up to 20%. The 3% uncertainty on the ratio of total efficiencies is mainly from the uncertainty on the Z acceptance and the evolution of the efficiency estimates with dimuon mass, which are estimated from simulation as discussed in Section 5.8. Table 5.8 below summarizes the systematic uncertainties on input parameters for the limit setting.

Observable	Uncertainty
Z'acc. × eff./Zacc. × eff. (MC evolution of efficiency with energy)	3%
Z/DY background (NLO effects)	6%
Z/DY background (PDF effects)	5-20% (10% average)

Table 5.8: The systematic uncertainties on input parameters for the limits.

5.10.3 Limits

The limits are set using the same 2010 procedure [74] on the ratio of the production cross section times branching ratio to dimuons for Z and Z′ bosons. We use a Bayesian technique using the RooStats [75] implementation of the Markov Chain Monte Carlo (MCMC) method [76] to perform the integration. The procedure followed to set a 95% CL limits is identical to that described in [20]. The dilepton mass spectrum is also assessed for the significance of a potential signal candidate by the method called "look-elsewhere" effect (LEE). The LEE represents the notion that the significance of a peak-like structure in the spectrum is reduced if one considers a possibility of background fluctuations in other regions of the spectrum. This is computed by modifying the limit setting tool to search for excesses rather than to set limits. It also corrects for the LEE by running pseudo-experiments. The input is the same to this tool as for the limits tool and allows for the dielectron and dimuon channels to be handled separately.

To compute the mass limits using specific benchmark models; Z'_{SSM} and Z'_{ψ}, we compute R_{σ} as a function of M using NLO or NNLO K-factors where available. These computed model's cross sections are plotted as the solid curves overlaid on Figure 5.9 with the width of the band indicating the theoretical uncertainties. The 95% CL mass limit is then found by the intersection of these curves with the observed limit on R_{σ}. In Figure 5.9, the predicted cross section times branching ratios for Z'_{SSM}, Z'_{ψ} are shown together with those for G_{KK} production. The leading order cross section predictions for Z'_{SSM} and Z'_{ψ} from PYTHIA using CTEQ6.1 PDFs are corrected for a mass dependent K factor obtained using ZWPRODP [7,77,78] to account for the NNLO QCD contributions.

The dominant uncertainty in this analysis is that in R_{ϵ}, the ratio of selection

efficiency times detector acceptance for Z′ decay to that of Z decay. This uncertainty is 8% for the dielectron channel and 3% for the dimuon channel. For the dimuon channel, the mass scale uncertainty for this analysis is set to zero. The effects of the uncertainties in the PDF and the higher order corrections on the shape of the background distribution, and hence on the fitting function used for the background, were examined. No further systematic uncertainties were found that required to accommodate these effects on the background shape.

The uncertainties described above are propagated into a comparison of the experimental limits with the predicted cross section times branching ratios (R_σ) to obtain a 95% CL lower limits on Z′ masses in various models. No uncertainties on cross sections for the various theoretical models are included when determining the limits. As a result of the dimuon analysis on the limit, the Z'_{SSM} can be excluded below 2150 GeV, and the Z'_ψ below 1820 GeV. For the dielectron, the production of Z'_{SSM} and Z'_ψ bosons is excluded for masses below 2120 and 1810 GeV, respectively. The combined limit obtained by using the product of the likelihoods for the individual channels is shown in Figure 5.9 (bottom). The 95% CL lower limits on the mass of a Z′ resonance are 2330 GeV for Z'_{SSM}, 2000 GeV for Z'_ψ. Table 5.9 below summarizes the 95% CL lower mass limits for the benchmark models considered for both channel individually and combined dilepton channel.

5.11 Summary

We performed a search for a narrow high mass resonance decaying to opposite-sign dimuons based on 5.28 fb^{-1} of pp collision data from the LHC at $\sqrt{s} = 7$ TeV taken in 2011. The agreement in the mass spectrum between the data and the SM simulation is

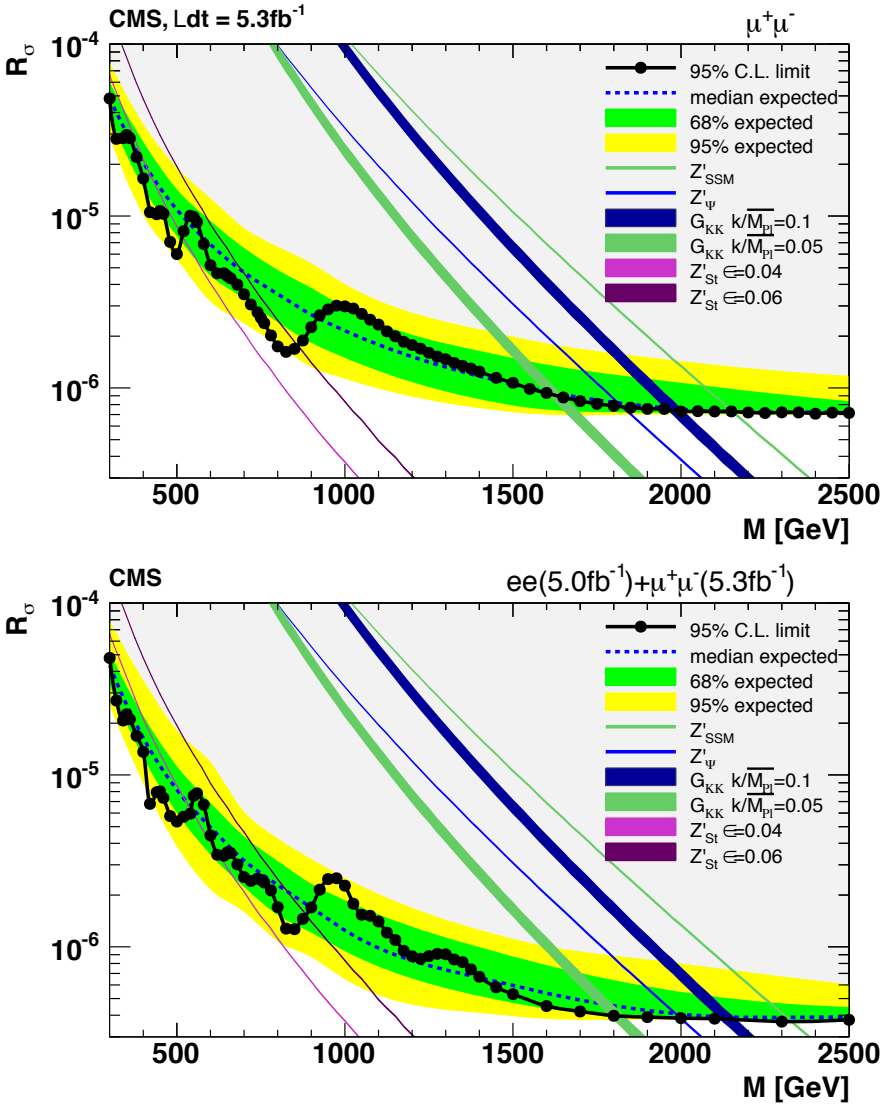

Figure 5.9: Upper limits as a function of the resonance mass M on the production ratio R_σ of cross section times branching fraction into lepton pairs for Z'_{SSM}, Z'_ψ and other production to the same quantity for Z bosons. The limits are shown for the $\mu^+\mu^-$ final state (top) and the combined dilepton result (bottom). Shaded green and yellow bands correspond to the 68% and 95% quantiles for the expected limits. The predicted cross section ratios are shown as bands with widths indicating the theoretical uncertainties. The differences in the widths reflect the different uncertainties in the K-factors used [79].

Model	$M_{\mu\mu}$	M_{ee}	M_{ll}, combined
Z'_{SSM}	2150	2120	2330
Z'_{ψ}	1820	1810	2000

Table 5.9: 95% CL lower mass limits for the benchmark models considered, with theoretical uncertainties included. The dimuon only limits, dielectron only limits and limits from the combination of the both channels are given. The mass limit is in GeV [79].

good. All cross checks and systematic studies show that the detector is well understood and that the non-DY backgrounds are under control. The spectra are consistent with expectations from the SM and upper limits have been set on the cross section times branching ratio for Z′ into lepton pairs relative to SM Z boson production and decay. At a 95% CL, for the dimuon channel, Z'_{SSM} can be excluded below 2150 GeV and Z'_{ψ} below 1820 GeV. For the combined (dilepton) channel, Z'_{SSM} can be excluded below 2330 GeV and Z'_{ψ} below 2000 GeV.

CHAPTER 6

Search for a Z' Using 8 TeV Collision Data of the 2012 Run

The LHC at CERN started pp collisions at $\sqrt{s} = 8$ TeV on March 30, 2012, after a successful operation in 2011. The search for Z' decaying to dimuons in the data collected during 2011 at $\sqrt{s} = 7$ TeV has already been presented in (Chapter 5). The CMS detector recorded its first 8 TeV collision events on April 5, 2012, about 23 fb^{-1} of the data. In this chapter, we perform the search of a Z' boson decaying to a muon pair using 20.6 fb^{-1} of 8 TeV collision data of the LHC collected with the CMS detector.

6.1 Introduction

This chapter describes a search for a narrow resonance in the dimuon mass spectra using pp collision data at $\sqrt{s} = 8$ TeV collected by the CMS detector at the LHC. We present the details of analysis, which uses the full 2012 dataset collected at $\sqrt{s} = 8$ TeV corresponding to an integrated luminosity of 20.6 fb^{-1}.

Similar to 2011 analysis, the search is performed by selecting events, which consists of good quality opposite sign pair of muons and reconstructing the dimuon mass. The dominant, irreducible SM background from the DY process together with the smaller, reducible backgrounds from $t\bar{t}$ and other SM processes, predict a smoothly

falling mass spectrum above the Z peak. We perform a shape analysis on the measured spectrum to find the bumps (resonance peak) from new physics. We use the resonant peak from the SM process $Z \to \mu^+\mu^-$ to normalize our results rather than normalizing to the absolute measurement of the luminosity. We consider the ratio:

$$\frac{\sigma(pp \to Z') \cdot \mathrm{BR}(Z' \to \mu^+\mu^-)}{\sigma(pp \to Z) \cdot \mathrm{BR}(Z \to \mu^+\mu^-)} = \frac{N(Z')}{N(Z)} \times \frac{A(Z)}{A(Z')} \times \frac{\epsilon(Z)}{\epsilon(Z')} \tag{6.1}$$

where $\sigma(pp \to Z')$ and $\sigma(pp \to Z)$ are the production cross sections at $\sqrt{s}$ =8 TeV of the new particle Z' and the SM Z, respectively; $\mathrm{BR}(Z' \to \mu^+\mu^-)$ and $\mathrm{BR}(Z \to \mu^+\mu^-)$ are the branching ratios into opposite-sign dimuon pair of Z' and Z, respectively; $N(Z')$ is the number of the dimuon pair in a given mass range above the Z peak, $A(Z')$ is the geometrical acceptance of muon pair, and $\epsilon(Z')$ is the trigger plus reconstruction efficiency for dimuon pair in acceptance. N(Z), A(Z), and $\epsilon(Z)$ are defined similarly, but using the mass range 60-120 GeV around the Z peak.

By interpreting our results using this ratio, we are robust against many known and unknown uncertainties as they cancel each other in ratio. For example, the absolute value of the luminosity cancels, which removes the substantial uncertainty associated with its measurement. To be robust against uncertainties in the absolute background level, the search for resonances is based on a shape analysis of the dimuon mass spectra. In the absence of a signal, we set limit on the ratio R_σ of the production cross section times branching ratio for high mass resonances to that for the Z boson.

6.2 Data and Monte Carlo samples

6.2.1 Dataset and run selection

Similar to the 2011 analysis, this analysis also uses the /SingleMu/ primary datasets while cross checks on efficiencies, backgrounds, relies on other datasets. We use the combination of prompt-reco and re-reco version of the full 2012 dataset. Based on the instantaneous luminosity, the 2012 data taking period was divided into four sections: 2012A, 2012B, 2012C and 2012D. We follow the recommendation of the PdmV group [80] to select the dataset and JSON files. For the run and lumisection selection, we use the official "MuonPhys" JSON files in which ECAL and HCAL do not have to be marked as good. In studies where electrons and other objects use "Golden" JSONs, requires ECAL and HCAL to be good.

The luminosity for the 2012 pp data taking is recommended to be estimated on the basis of the pixel cluster counting method [81]. It has been approved and announced by the Luminosity Physics Object Group (LUM POG) on August 28, 2013. Detailed documentation for the lumi measurements can be found on the lumiCalc twiki [82]. The uncertainty related to the pixel cluster counting based luminosity is 2.6% . This dataset corresponds to the integrated luminosity of 20.575 fb^{-1} by a pixel cluster counting method. The Table 6.1 below shows the datasets used in this analysis with run ranges and corresponding luminosities.

Dataset	Run range	Int.Luminosity(pb^{-1})
/SingleMu/Run2012A-13Jul2012-v1/AOD	190456-193621	841.867
/SingleMu/Run2012A-recover-06Aug2012-v1/AOD	190782-190949	81.669
/SingleMu/Run2012B-13Jul2012-v1/AOD	193833-196531	4811.00
/SingleMu/Run2012C-24Aug2012-v1/AOD	198022-198913	480.233
/SingleMu/Run2012C-PromptReco-v2/AOD	198934-203746	6729.00
/SingleMu/Run2012D-PromptReco-v1/AOD	203768-208686	7631.00
Total (2012A+2012B+2012C+2012D)	190456-208686	20574.769

Table 6.1: Datasets used in this analysis with run ranges and corresponding luminosities.

6.2.2 Monte Carlo samples

Similar to the 2011 analysis, simulated event samples for the signal and background processes for the 2012 run were also generated with PYTHIA, MADGRAPH and POWHEG event generators. The MADGRAPH generator was used for W+jets samples, and the POWHEG for DY, single top and $t\bar{t}$ samples. Both of these generators were interfaced with the PYTHIA (using the Z2 tunestar) parton shower generator. The diboson samples are generated with PYTHIA. The parton distribution functions used for PYTHIA and POWHEG samples are same as in the 2011 analysis (Chapter 5) and the response of the detector was simulated using GEANT4. Table 6.2 lists the generators, physics processes, kinematic cuts, cross sections, number of events for the various signal and background samples produced with MC simulation that are used in this analysis. The various background samples are combined using the information in this table to produce the overall prediction from simulation. Table 6.3 lists the datasets used in the MC simulation of the signal and background processes considered. The V7A, V7C1, and V7C2 tags in the dataset of Table 6.3 refer to different muon misalignment scenarios. The LO, NLO and NNLO listed in the table refers to the leading order, next-to leading order, next-next-to leading order correction applied to the simulated samples. The

numbers 1.3 and 1.024 are the QCD K-factor used to correct the samples to NLO and NNLO cross section respectively.

Process	Program	Generation parameters	σ (pb)	Events
$Z'_\psi \to \mu^+\mu^-$	PYTHIA	M = 750 GeV	0.14 (LO) × 1.3	25040
		M = 1000 GeV	0.0369 (LO) × 1.3	25040
		M = 1250 GeV	0.0129 (LO) × 1.3	25344
		M = 1500 GeV	0.00433 (LO) × 1.3	25344
		M = 1750 GeV	0.00172 (LO) × 1.3	25272
		M = 2000 GeV	6.88E-4 (LO) × 1.3	25092
		M = 2250 GeV	2.93E-4 (LO) × 1.3	25104
		M = 2500 GeV	1.27E-4 (LO) × 1.3	25344
		M = 2750 GeV	5.55E-5 (LO) × 1.3	25376
		M = 3000 GeV	2.5E-5 (LO) × 1.3	25040
$Z/\gamma^* \to \mu^+\mu^-$	POWHEG	$M_{\mu\mu} > 20$ GeV	1915 (NNLO)	3293740
		$M_{\mu\mu} > 120$GeV	12.17 (NLO × 1.024)	99984
		$M_{\mu\mu} > 200$GeV	1.520 (NLO × 1.024)	99990
		$M_{\mu\mu} > 500$GeV	0.04519 (NLO × 1.024)	99992
		$M_{\mu\mu} > 800$GeV	0.005620 (NLO × 1.024)	99984
		$M_{\mu\mu} > 1000$GeV	0.001838 (NLO × 1.024)	99989
		$M_{\mu\mu} > 1500$GeV	1.745E-4 (NLO × 1.024)	99992
		$M_{\mu\mu} > 2000$GeV	2.260E-5 (NLO × 1.024)	99974
$Z/\gamma^* \to \tau^+\tau^-$	POWHEG	$M_{\tau^+\tau^-} > 20$GeV	1915 (NNLO)	3295238
$t\bar{t}$	POWHEG	—	234 (NNLO)	21675970
tW	POWHEG	—	11.1 (NNLO)	497658
$\bar{t}$W	POWHEG	—	11.1 (NNLO)	493460
WW	PYTHIA	—	54.8 (NLO)	10000431
WZ	PYTHIA	—	33.2 (NLO)	10000283
ZZ	PYTHIA	—	17.6 (NLO)	9799908
W+jets	MADGRAPH	—	36257 (NNLO)	18393090
Inclusive-μ QCD	PYTHIA	$\hat{p}_T > 20$GeV, $\lvert\eta(\mu)\rvert < 2.5$, $p_T(\mu) > 15$GeV	3.64E8 × 3.7E-4 (LO)	21484602

Table 6.2: Summary of simulated signal and background samples. TAUOLA is also used for those samples where τ decays are relevant.

6.3 Trigger requirements

The trigger used to select events for this analysis is the lowest p_T threshold unprescaled single muon trigger without muon isolation requirements. In 2012, we used the same trigger path used in the analysis of the 2011 dataset, HLT_Mu40_ eta2p1, which requires at least one muon candidate with a transverse momentum $p_T > 40$ GeV. To keep

Process	Dataset path
$Z'_{\psi} \to \mu^+\mu^-$	/ZprimePSIToMuMu_M-750_TuneZ2star_8TeV-pythia6/Summer12_DR53X-PU_S10_START53_V7A-v1
	/ZprimePSIToMuMu_M-1000_TuneZ2star_8TeV-pythia6/Summer12_DR53X-PU_S10_START53_V7A-v1
	/ZprimePSIToMuMu_M-1250_TuneZ2star_8TeV-pythia6/Summer12_DR53X-PU_S10_START53_V7A-v1
	/ZprimePSIToMuMu_M-1500_TuneZ2star_8TeV-pythia6/Summer12_DR53X-PU_S10_START53_V7A-v1
	/ZprimePSIToMuMu_M-1750_TuneZ2star_8TeV-pythia6/Summer12_DR53X-PU_S10_START53_V7A-v1
	/ZprimePSIToMuMu_M-2000_TuneZ2star_8TeV-pythia6/Summer12_DR53X-PU_S10_START53_V7A-v1
	/ZprimePSIToMuMu_M-2250_TuneZ2star_8TeV-pythia6/Summer12_DR53X-PU_S10_START53_V7A-v1
	/ZprimePSIToMuMu_M-2500_TuneZ2star_8TeV-pythia6/Summer12_DR53X-PU_S10_START53_V7A-v1
	/ZprimePSIToMuMu_M-2750_TuneZ2star_8TeV-pythia6/Summer12_DR53X-PU_S10_START53_V7A-v1
	/ZprimePSIToMuMu_M-3000_TuneZ2star_8TeV-pythia6/Summer12_DR53X-PU_S10_START53_V7A-v1
	/ZprimePSIToMuMu_M-750_TuneZ2star_8TeV-pythia6/Summer12_DR53X-PU_S10_START53_V7C1-v1
	/ZprimePSIToMuMu_M-1000_TuneZ2star_8TeV-pythia6/Summer12_DR53X-PU_S10_START53_V7C1-v1
	/ZprimePSIToMuMu_M-1250_TuneZ2star_8TeV-pythia6/Summer12_DR53X-PU_S10_START53_V7C1-v1
	/ZprimePSIToMuMu_M-1500_TuneZ2star_8TeV-pythia6/Summer12_DR53X-PU_S10_START53_V7C1-v1
	/ZprimePSIToMuMu_M-1750_TuneZ2star_8TeV-pythia6/Summer12_DR53X-PU_S10_START53_V7C1-v1
	/ZprimePSIToMuMu_M-2000_TuneZ2star_8TeV-pythia6/Summer12_DR53X-PU_S10_START53_V7C1-v1
	/ZprimePSIToMuMu_M-2250_TuneZ2star_8TeV-pythia6/Summer12_DR53X-PU_S10_START53_V7C1-v1
	/ZprimePSIToMuMu_M-2500_TuneZ2star_8TeV-pythia6/Summer12_DR53X-PU_S10_START53_V7C1-v1
	/ZprimePSIToMuMu_M-2750_TuneZ2star_8TeV-pythia6/Summer12_DR53X-PU_S10_START53_V7C1-v1
	/ZprimePSIToMuMu_M-3000_TuneZ2star_8TeV-pythia6/Summer12_DR53X-PU_S10_START53_V7C1-v1
	/ZprimePSIToMuMu_M-750_TuneZ2star_8TeV-pythia6/Summer12_DR53X-PU_S10_START53_V7C2-v1
	/ZprimePSIToMuMu_M-1000_TuneZ2star_8TeV-pythia6/Summer12_DR53X-PU_S10_START53_V7C2-v1
	/ZprimePSIToMuMu_M-1250_TuneZ2star_8TeV-pythia6/Summer12_DR53X-PU_S10_START53_V7C2-v1
	/ZprimePSIToMuMu_M-1500_TuneZ2star_8TeV-pythia6/Summer12_DR53X-PU_S10_START53_V7C2-v1
	/ZprimePSIToMuMu_M-1750_TuneZ2star_8TeV-pythia6/Summer12_DR53X-PU_S10_START53_V7C2-v1
	/ZprimePSIToMuMu_M-2000_TuneZ2star_8TeV-pythia6/Summer12_DR53X-PU_S10_START53_V7C2-v1
	/ZprimePSIToMuMu_M-2250_TuneZ2star_8TeV-pythia6/Summer12_DR53X-PU_S10_START53_V7C2-v1
	/ZprimePSIToMuMu_M-2500_TuneZ2star_8TeV-pythia6/Summer12_DR53X-PU_S10_START53_V7C2-v1
	/ZprimePSIToMuMu_M-2750_TuneZ2star_8TeV-pythia6/Summer12_DR53X-PU_S10_START53_V7C2-v1
	/ZprimePSIToMuMu_M-3000_TuneZ2star_8TeV-pythia6/Summer12_DR53X-PU_S10_START53_V7C2-v1
$Z/\gamma^* \to \mu^+\mu^-$	/DYToMuMu_M-20_CT10_TuneZ2star_8TeV-powheg-pythia6/Summer12_DR53X-PU_S10_START53_V7A-v1
	/DYToMuMu_M-120_CT10_TuneZ2star_8TeV-powheg-pythia6/Summer12_DR53X-PU_S10_START53_V7A-v1
	/DYToMuMu_M-200_CT10_TuneZ2star_8TeV-powheg-pythia6/Summer12_DR53X-PU_S10_START53_V7A-v1
	/DYToMuMu_M-500_CT10_TuneZ2star_8TeV-powheg-pythia6/Summer12_DR53X-PU_S10_START53_V7A-v1
	/DYToMuMu_M-800_CT10_TuneZ2star_8TeV-powheg-pythia6/Summer12_DR53X-PU_S10_START53_V7A-v1
	/DYToMuMu_M-1000_CT10_TuneZ2star_8TeV-powheg-pythia6/Summer12_DR53X-PU_S10_START53_V7A-v1
	/DYToMuMu_M-1500_CT10_TuneZ2star_8TeV-powheg-pythia6/Summer12_DR53X-PU_S10_START53_V7A-v1
	/DYToMuMu_M-2000_CT10_TuneZ2star_8TeV-powheg-pythia6/Summer12_DR53X-PU_S10_START53_V7A-v1
	/DYToMuMu_M-120_CT10_TuneZ2star_8TeV-powheg-pythia6/Summer12_DR53X-PU_S10_START53_V7C1-v1
	/DYToMuMu_M-200_CT10_TuneZ2star_8TeV-powheg-pythia6/Summer12_DR53X-PU_S10_START53_V7C1-v1
	/DYToMuMu_M-500_CT10_TuneZ2star_8TeV-powheg-pythia6/Summer12_DR53X-PU_S10_START53_V7C1-v1
	/DYToMuMu_M-800_CT10_TuneZ2star_8TeV-powheg-pythia6/Summer12_DR53X-PU_S10_START53_V7C1-v1
	/DYToMuMu_M-1000_CT10_TuneZ2star_8TeV-powheg-pythia6/Summer12_DR53X-PU_S10_START53_V7C1- v1
	/DYToMuMu_M-1500_CT10_TuneZ2star_8TeV-powheg-pythia6/Summer12_DR53X-PU_S10_START53_V7C1-v1
	/DYToMuMu_M-2000_CT10_TuneZ2star_8TeV-powheg-pythia6/Summer12_DR53X-PU_S10_START53_V7C1-v1
	/DYToMuMu_M-120_CT10_TuneZ2star_8TeV-powheg-pythia6/Summer12_DR53X-PU_S10_START53_V7C2-v1
	/DYToMuMu_M-200_CT10_TuneZ2star_8TeV-powheg-pythia6/Summer12_DR53X-PU_S10_START53_V7C2-v1
	/DYToMuMu_M-500_CT10_TuneZ2star_8TeV-powheg-pythia6/Summer12_DR53X-PU_S10_START53_V7C2-v1
	/DYToMuMu_M-800_CT10_TuneZ2star_8TeV-powheg-pythia6/Summer12_DR53X-PU_S10_START53_V7C2-v1
	/DYToMuMu_M-1000_CT10_TuneZ2star_8TeV-powheg-pythia6/Summer12_DR53X-PU_S10_START53_V7C2-v1
	/DYToMuMu_M-1500_CT10_TuneZ2star_8TeV-powheg-pythia6/Summer12_DR53X-PU_S10_START53_V7C2-v1
	/DYToMuMu_M-2000_CT10_TuneZ2star_8TeV-powheg-pythia6/Summer12_DR53X-PU_S10_START53_V7C2-v1

Process	Dataset path
$Z/\gamma^* \to \tau^+\tau^-$	/DYToTauTau_M-20_CT10_TuneZ2star_8TeV-powheg-pythia6/Summer12_DR53X-PU_S10_START53_V7A-v1
$t\bar{t}$	/TT_CT10_TuneZ2star_8TeV-powheg-tauola/Summer12_DR53X-PU_S10_START53_V7A-v2
tW	/T_tW-channel-DR_TuneZ2star_8TeV-powheg-tauola/Summer12_DR53X-PU_S10_START53_V7A-v1
$\bar{t}$W	/Tbar_tW-channel-DR_TuneZ2star_8TeV-powheg-tauola/Summer12_DR53X-PU_S10_START53_V7A-v1
WW	/WW_TuneZ2star_8TeV_pythia6_tauola/Summer12_DR53X-PU_S10_START53_V7A-v1
WZ	/WZ_TuneZ2star_8TeV_pythia6_tauola/Summer12_DR53X-PU_S10_START53_V7A-v1
ZZ	/ZZ_TuneZ2star_8TeV_pythia6_tauola/Summer12_DR53X-PU_S10_START53_V7A-v1
W+jets	/WJetsToLNu_TuneZ2Star_8TeV-madgraph-tarball/Summer12_DR53X-PU_S10_START53_V7A-v1
Incl.-μ QCD	/QCD_Pt_20_MuEnrichedPt_15_TuneZ2star_8TeV_pythia6/Summer12_DR53X-PU_S10_START53_V7A-v3

Table 6.3: Dataset paths for the Summer 2012 simulated background samples.

the trigger rate at an acceptable level, the acceptance of this trigger is restricted to the pseudorapidity range of $|\eta| < 2.1$, and quality cuts are applied to the muon candidate.

CMS software (CMSSW), the HLT muon reconstruction and the quality cuts are changed in 2012. Therefore, we have done a basic check of the trigger efficiency as measured in simulation using the DY events with both muons in acceptance (defined as one muon in the restricted pseudorapidity range $|\eta|<2.1$, the other in $|\eta|<2.4$) simulated in CMSSW_5_3_2. Figure 6.1 shows the combined L1+HLT trigger efficiency as a function of dimuon invariant mass. The total trigger efficiency is predicted to be about 97% for the entire range of dimuon masses under consideration. This is 1-2% lower than was predicted by the 2011 MC samples.

6.4 Tag and Probe method

The "Tag and Probe" is a generic tool developed to measure any lepton efficiency directly from CMS data, e.g. reconstruction, trigger, selection, tracking etc., using dilepton resonances such as Z or J/ψ. Resonances are reconstructed as pairs with one leg passing a tight identification (tag) and one passing a loose identification (probe). "Passing probes" are defined according to the particular efficiency that is to be measured. The (tag + passing probe) and (tag + failing probe) lineshapes are fit separately with

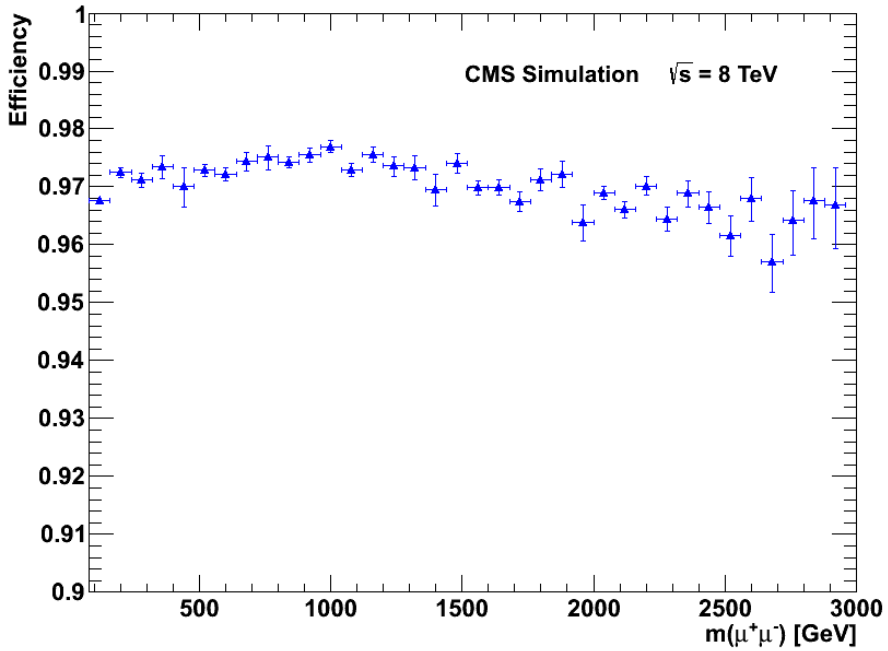

Figure 6.1: The efficiency of the single muon trigger path (HLT_Mu40_eta2p1), used in this analysis for dimuon events as a function of dimuon invariant mass evaluated using CMSSW_5_3_2 .

a signal plus background model. The efficiency is computed from the ratio of the signal yields in the two lineshapes described above. The procedure is repeated in bins of the probe variables (e.g. p_T, η, etc.) to compute efficiency histograms as a function of those variables. For muon related efficiencies, tags are usually good-quality muons matched to a single muon trigger object; probes are muons, inclusive calo muons or just tracks in the tracker or the muon system.

The efficiencies of the single muon trigger (HLT_Mu40_eta2p1) in the data were studied by the muon POG. They are measured by applying the "Tag and Probe" method [61] to muons from Z decays and then compared to the predictions of the MC simulation. Muon POG used the Tag and Probe trees [83] produced by the Higgs Physics Analysis Group (HIG PAG). Trigger efficiencies are defined relative to muons reconstructed offline

and passing selection criteria very similar to those used in our analysis. The efficiency of the single muon trigger is measured to be 94.13 ± 0.02(stat.)%, 84.27 ± 0.07(stat.)%, and 82.66 ± 0.05(stat.)% for single muons in the regions of $|\eta| < 0.9$, $0.9 < |\eta| < 1.2$ and $1.2 < |\eta| < 2.1$, respectively [84]. These measurements translate into efficiencies of 97% or higher for our signal events containing two muons in the final state. The corresponding scale factors, defined as the ratios of measured to efficiencies predicted by MC, are 0.9812 ± 0.0003(stat.) ± 0.0020(syst.), 0.9615 ± 0.0010(stat.) ± 0.0019(syst.), and 0.9918 ± 0.0008(stat.) ± 0.0020(syst.) .

6.5 Event, muon, and dimuon selection

The event and dimuon selection requirements are kept exactly the same as they were in the 2011 published results [73, 85] and the International Conference on High Energy Physics (ICHEP) 2012 results [86, 87], but the muon identification requirements follows the most recent recommendation from the muon POG [88]. The new high p_T muon selection relaxes the requirement made on the number of tracker layers in the muon fit and adds a requirement on the offline muon dp_T/p_T. Together with the new momentum assignment logic [88], the efficiency improves and the momentum misassignment rate is reduced. To get a sample of pure dimuon events with high efficiency, we impose the following event selection:

- To avoid events from beam backgrounds, we filter out events in which fewer than a quarter of the tracks in the silicon tracker are marked as being of high purity.

- We require a "good" offline reconstructed primary vertex to be found in the event as defined by the tracking POG in the CMS. A primary vertex is good if at least four

tracks must be associated to the vertex and located within $|r| < 2$ cm and $|z| < 24$ cm of the nominal interaction point. This cut is particularly useful in rejecting cosmic ray muons triggering in empty bunch crossings, which can produce fake dimuons when traversing the detector near the interaction point.

- The muon must be reconstructed as a "global" muon and a "tracker" muon.
- The offline muon p_T must be at least 45 GeV.
- The global muon track fit must include at least one hit from each of the pixel detector and the muon system.
- The global muon track must have at least six tracker layers with hits in the fit.
- The tracker muon must have matched segments in at least two muon stations.
- The relative p_T error $\delta p_T/p_T$ is required to be smaller than 0.3 to reduce all the misreconstructed muons.
- The muon's transverse impact parameter with respect to the primary vertex, as measured by the tracker-only fit, must be less than 2 mm.
- The muon must pass a relative "tracker-only" isolation cut; the sum of the p_T of all other tracks in a cone of $\Delta R < 0.3$ excluding muon's tracker track must be less than 10% of the muon's p_T, also as measured by the tracker.
- At least one of the reconstructed muon candidates must be matched within $\Delta R < 0.2$ to the HLT muon candidate (trigger muon), which has a p_T threshold of 40 GeV/c and is restricted to the $|\eta| < 2.1$.

To form a dimuon, the two muons passing the above selection must further satisfy the following requirements:

- must have an opposite charge.
- must be consistent with originating from a common vertex. A constrained fit of the muon candidate tracks to a common vertex must satisfy $\chi^2 < 10$.
- To reduce the background from cosmic ray, muons that pass close to the detector interaction point can appear as two muon candidates back-to-back in space, faking a dimuon event. To suppress this, in addition to the impact parameter cut, we require the three dimensional angle between the two muon's momenta be less than π - 0.02 radian.

In events with more than one opposite-sign dimuon, only the one with the highest invariant mass is kept. We perform a common vertex fit using the Kalman filter formulation as implemented in CMSSW [62] to compute the kinematics of the dimuon system, particularly its mass. This also helps to ensure that the two muons originate from the same vertex as a guard against pileup and as a check on reconstruction quality; we explicitly require that the vertex fit has $\chi^2 < 10$.

Muons are fundamentally measured in q/p_T, so there might be a possibility of charge misidentification, which could make the q/p_T measurement wrong. The rate of muon charge misidentification is known [47] to be below 0.5% for muons with p_T up to 300 GeV, so the requirement for opposite-sign dimuons is still highly efficient. So as a quality cut, we do not use same sign events in our final selection; however, we use it as a control sample.

The muon POG studied the efficiency of the muon reconstruction and selection requirements. Applying the "Tag and Probe" method to muons from the Z decays and using tracks in the silicon strip tracker as probes, the efficiency of all above selection criteria except isolation is measured to be 95.9 ± 0.0001(stat.)%, 95.8 ± 0.0002(stat.)%, 95.4 ± 0.0002(stat.)%, and 94.8 ± 0.0005(stat.)% in the regions of $|\eta| < 0.9$, $0.9 < |\eta| < 1.2$, $1.2 < |\eta| < 2.1$ and $2.1 < |\eta| < 2.4$ with scale factors between data and the simulation of $0.9932 \pm 0.0002(\text{stat.}) \pm 0.0050(\text{syst.})$, $0.9911 \pm 0.0003(\text{stat.}) \pm 0.0050(\text{syst.})$, $0.9975 \pm 0.0002(\text{stat.}) \pm 0.0050(\text{syst.})$, and $0.9946 \pm 0.0006(\text{stat.}) \pm 0.0050(\text{syst.})$, respectively [89]. The efficiency of the tracker only isolation cut is measured separately and is found to be 98.6 ± 0.0(stat.)%, with the data to simulation ratio of efficiencies of $1.001 \pm 0.000(\text{stat.}) \pm 0.002(\text{syst.})$ [90].

6.6 The effect of pileup on muon isolation

Our selected muons are required to be isolated to reject background from misidentified muons from jets and non-prompt muons from hadron decays. For the 2012 data, the number of pileup events is larger which could decrease signal efficiency. Pileup interactions generate more charged tracks and more energy deposited in the calorimeters for each primary interaction. As our isolation requirement is loose (relative cut on the" tracker-only" isolation), only the former case is relevant to our analysis. To cross check that we are robust against these effects, we examine the distributions of the relative "tracker-only" isolation as a function of the number of reconstructed primary vertices. We also examine the behavior of a "tracker-plus-calorimeters" isolation variable for comparison.

We obtain a pure sample of $Z \to \mu^+\mu^-$ events by selecting events with a pair

of oppositely-charged muons that form an invariant mass in a mass region around the nominal Z mass, between 60-120 GeV, and with each muon satisfying all the identification criteria described in the previous section except the isolation. Using muons from Z decay helps to suppress muons that are not originally isolated; in the mass range selected, the expectation from simulation is that only about 1.5% of dimuons are from processes other than $Z \to \mu^+\mu^-$ even when no isolation cut is applied. Figure 6.2 shows the fraction of muons that fail a cut on the "tracker-only" and "tracker-plus-calorimeters" relative isolation variables at thresholds of 0.10 and 0.15, respectively, as a function of the number of reconstructed primary vertices. An increase in the fail rate with the number of primary vertices is $\approx 1\%$ for "tracker-only" relative isolation and 4-5 % for "tracker-plus- calorimeters" isolation.

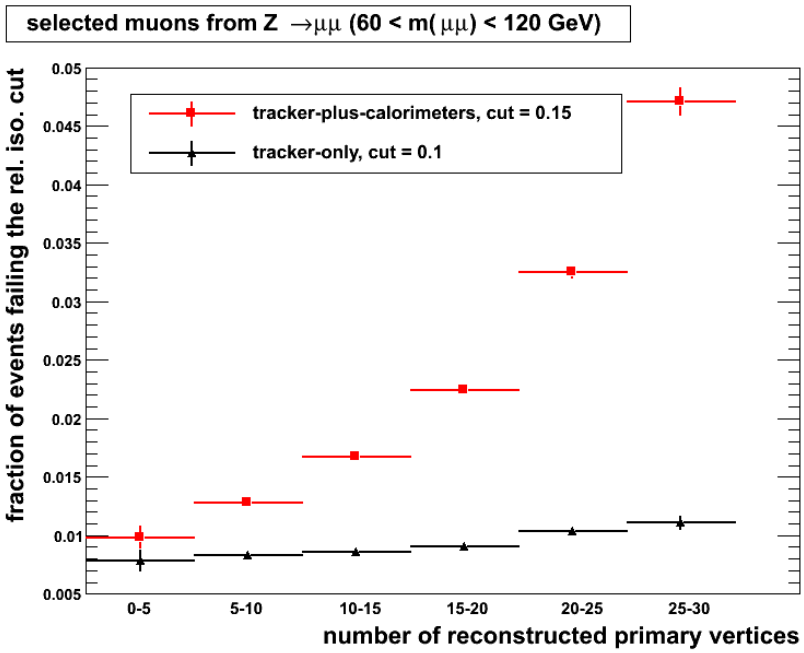

Figure 6.2: For dimuons on the Z peak ($60 < M_{\mu\mu} < 120$ GeV) in the data, the fraction of muons otherwise selected using our analysis cuts that fail a cut on the "tracker-only" relative isolation at 0.1 (black triangles) or a cut on the "tracker-plus-calorimeters" relative isolation at 0.15 (red squares) as a function of the number of reconstructed primary vertices.

Figure 6.3 shows the combined reconstruction and selection efficiency for dimuons passing the above cuts with respect to triggered events in acceptance (defined as one muon in $|\eta| < 2.1$, both muons in $|\eta| < 2.4$, and both muons having $p_T > 45$ GeV), with respect to all events in acceptance, and the total acceptance times efficiency as a function of dimuon invariant mass. This study was performed on simulated DY events using CMSSW_5_3_2 with START53_V7-C1 global tag. The Z peak has been cut away by the online and offline p_T thresholds, while above the Z peak, most of the total inefficiency at dimuon invariant masses below one TeV is due to the geometrical acceptance.

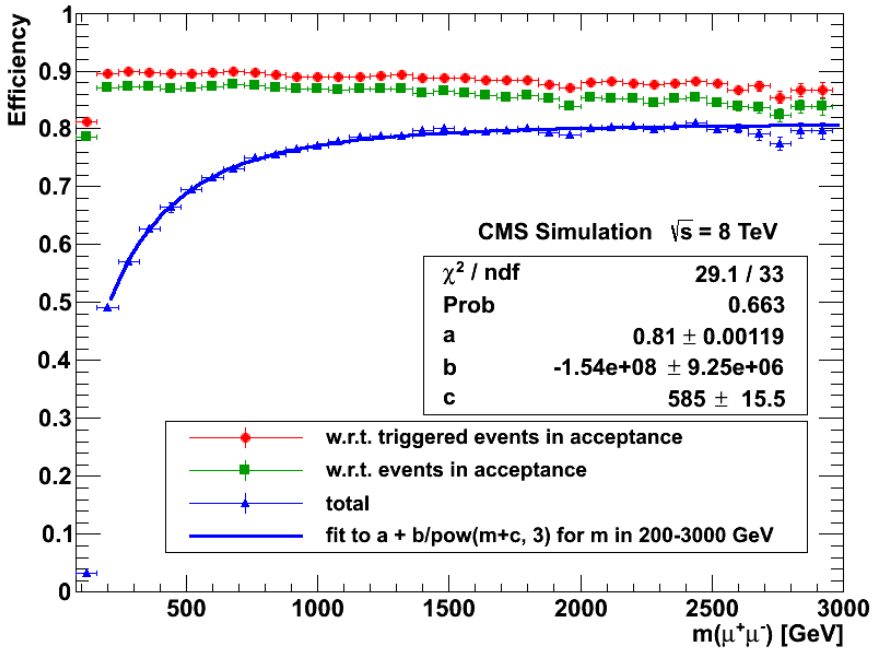

Figure 6.3: The efficiency for dimuons passing our selection with respect to "triggered events in acceptance", with respect to " events in acceptance", and the "total acceptance times efficiency" as a function of inavariant mass as evaluated on simulated DY events. The solid blue curve is a fit to the "total acceptance times efficiency" in the dimuon mass range, from 200 to 3000 GeV.

The combined reconstruction and selection efficiency for triggered events in acceptance is about 90% at $M_{\mu\mu} = 200$ GeV and decreases by only about 3% in the range of

$M_{\mu\mu}$ = 200-3000 GeV. These values are 6-7% higher than those observed in the ICHEP 2012 analysis [87] due to a loose requirement on the minimum number of tracker layers with hits in the track fit and improvements in the muon momentum assignment. This gain in efficiency is also shown in Figure 6.4, which shows the ratio of the number of events in the region $60 < M_{\mu\mu} < 120$ GeV that pass all selection cuts to the number of events passing all cuts except for the one indicated for main cuts in the event selections used in this analysis. The total reconstruction and selection efficiency for the signal, including acceptance for Z′ resonances, is above 70% for masses above 500 GeV and reaches 80% at $M_{\mu\mu}$ = 3 TeV.

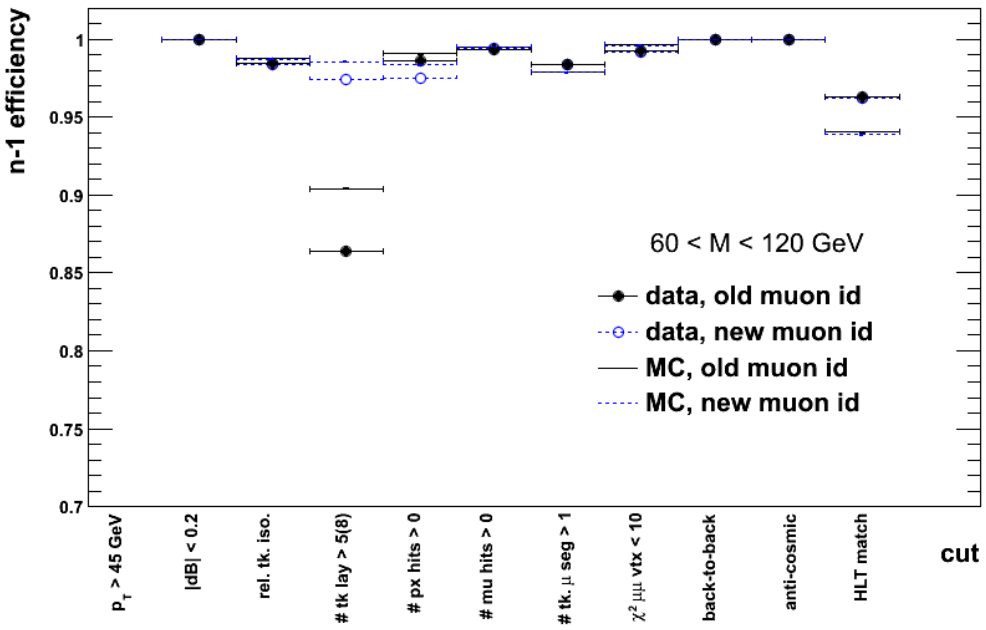

Figure 6.4: The ratio of the number of events in the region $60 < M_{\mu\mu} < 120$ GeV for main cuts in the event selection that pass all selection cuts to the number of events passing all cuts but the one indicated. The ratio measured from the 2012 data is shown in blue open circles and the prediction by the MC simulation is shown in blue dashed lines. The corresponding ratios for the selection used for the ICHEP 2012 results is shown for comparison in black filled circles for data and as black solid lines for the simulation.

6.7 Muon reconstruction

In CMS, the muon reconstruction software uses tracks reconstructed in the inner silicon tracker matched to tracks reconstructed in the outer muon system to produce the global muon track, which gives an estimate for the muon charge, momentum, and production vertex. This is done separately in the inner tracker for all charge particles producing the "tracker-only" fit, and in the muon system, producing the "standalone" fit. Matching standalone tracks to compatible "tracker-only" tracks, a "global" muon track can be reconstructed using the hits from the original pair of tracks. Several different strategies for including information from the muon system have been developed for high p_T muon reconstruction and momentum assignment. The high p_T muon algorithms and their performance are documented in [91, 92].

We use the "Tune P" algorithm, which chooses on a muon by muon basis between the results of a few such algorithms using the tail probability of the $\chi^2/d.o.f$ of the muon track fits. The track selection algorithm has been refined since the ICHEP 2012 analysis by adding a value of the relative p_T measurement error dp_T/p_T greater than 0.25. This new addition helps to suppress misreconstructed muons and allows us to relax the requirement on the number of tracker layers containing hits used in the track fit.

The invariant mass resolution is evaluated from simulation using signal samples listed in Table 6.3. The reconstructed invariant mass of each dimuon passing our selection criteria is compared to its true mass. The resolution is derived by fitting the core of the distribution with a Gaussian as shown in Figure 6.5.

In the previous analysis (ICHEP 2012), we found an unexpected phi-dependent bias between the tracker and muon system measurements of muon p_T in the simulated

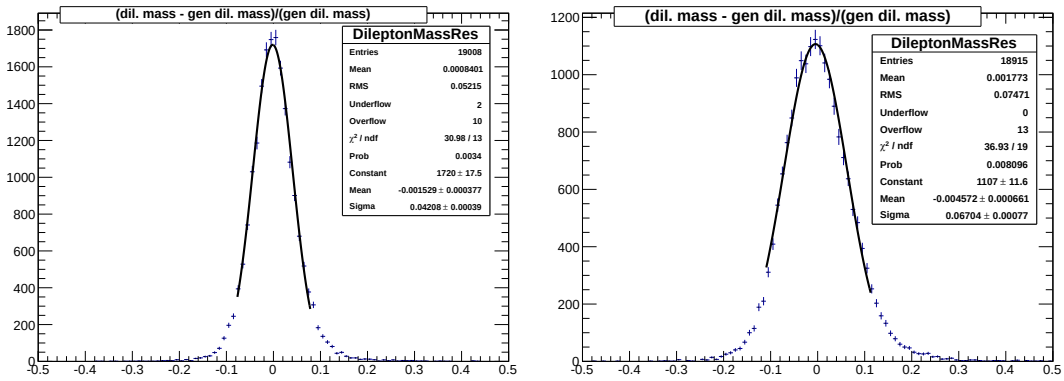

Figure 6.5: Examples of Gaussian fits of the core of the resolution. The left plot shows the distribution for 1 TeV Z′ decays, and the right plot shows the distribution for 2 TeV Z′ decays.

samples. This bias, present in the STARTUP misalignment scenario used in the summer 2012 MC samples (samples with V7A tags in Table 6.3) was a 2 mm upward shift of the barrel muon system. It has no impact on the dimuon mass resolution at mass values below 200 GeV where the tracker dominates, but worsens the resolution at higher masses. Therefore, we used especially generated DY and Z′ samples produced with two sets of updated alignment constants: C1, which copies the old misalignment scenario with the upwards shift of the muon barrel removed (with tags V7C1 in Table 6.3), and C2 with all muon detectors randomly displaced from ideal locations according to the statistical uncertainty of their positions as determined from the 2011 data (with tags V7C2 in Table 6.3).

Figure 6.6 shows the dimuon mass resolution plots for DY MC samples with $M_{\mu\mu} > 1500$ GeV. The top two plots show the difference between the old (left) and new (right) muon ID and momentum assignment, which are evaluated using the MC sample produced with the STARTUP muon misalignment scenario. The comparison of the number of entries and Gaussian fit sigmas shows that the efficiency increases

and the resolution slightly worsens. The worsening of the resolution is as expected since the alignment bug was present in the sample used, whereas, the new "Tune P" momentum assignment algorithm was tuned on MC samples without the bug. The resolution for the samples with fixed alignment are shown in the bottom row of Figure 6.6. A significant improvement of the resolution is found with σ of the Gaussian fits changing from 0.087 for the STARTUP misalignment scenario to 0.058 and 0.046 for the C1 and C2 misalignment scenarios, respectively. The resolution of the "tracker-only" momentum measurement (not shown) remains relatively constant at 0.074 for all the cases. Following the recommendation of the muon alignment group, we are taking the C1 scenario as the baseline for this analysis. All the plots and numbers in this dissertation are based on the C1 DY and signal samples.

Figure 6.7 shows the dimuon mass resolution as a function of invariant mass for three different reconstruction algorithms, the old misalignment and muon ID and for the two new misalignments together with new muon ID. Using the fixed misalignment and new muon ID inverts the hierarchy of the results, ordering the three reconstruction methods in the expected way. First, the fits including the muon system give better resolution at high mass than the "tracker only" fit. Second, the re-optimized "Tune P" algorithm is seen to provide an improvement over the old version in the core resolution even though the main goal of its optimization was to suppress extreme tails of momentum resolution to allow us to loosen the tracker layers ID requirement. Finally, we notice the improvement in the "tracker-only" resolution when moving to updated ID and misalignment. This change is caused by the ID change, the newly introduced requirement of track $dp_T/p_T < 0.3$. At high muon momenta, this cut removes poorly reconstructed tracker

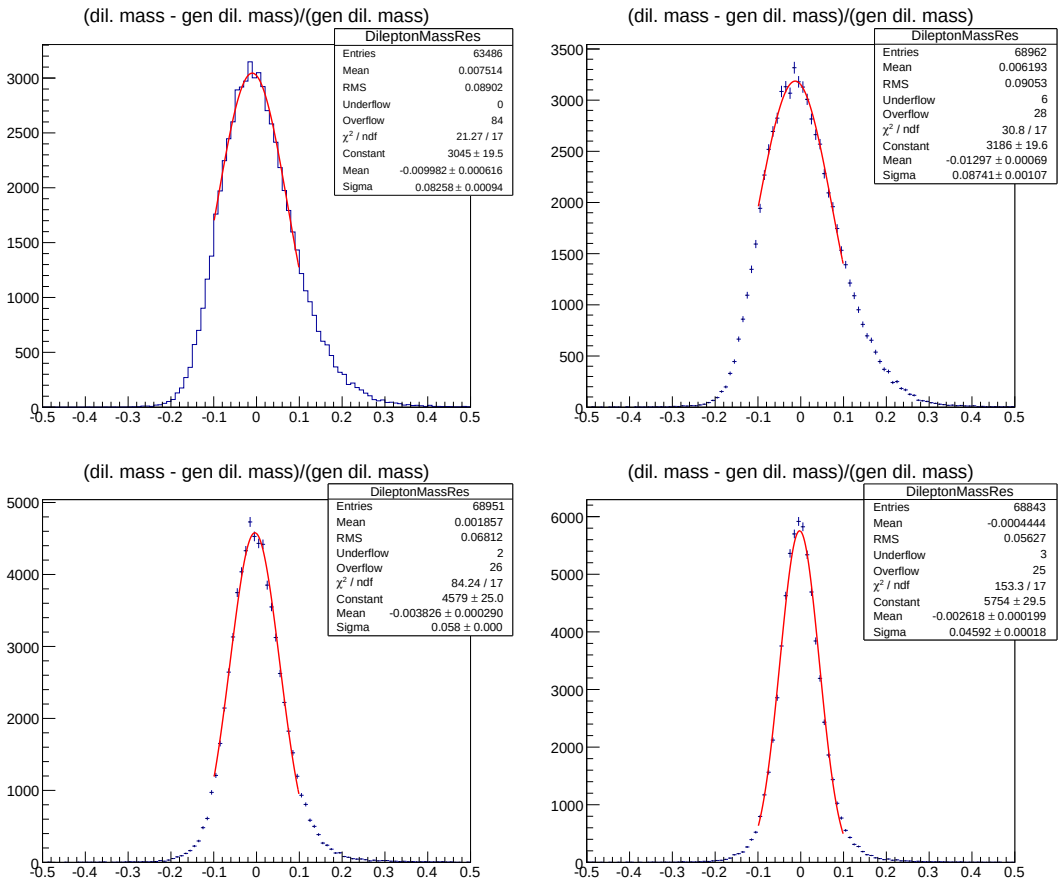

Figure 6.6: Relative dimuon mass resolution extracted from the DY MC samples generated with $M_{\mu\mu} > 1500$ GeV. The top row shows results obtained with the old STARTUP alignment using the ICHEP 2012 (left) and new muon ID and momentum assignment (right). The bottom row shows results for the two new misalignment scenarios, C1 (left) and C2 (right).

tracks, resulting in an improvement of the resolution seen in the plots. The distributions are fitted to a second-order polynomial and the results of the fits are also shown in Figure 6.7. The parameterization obtained for the re-optimized "Tune P" algorithm and the C1 misalignment scenario is $\sigma(m)/m = 0.01675 + 2.575 \times 10^{-5} m + 2.862 \times 10^{-10} m^2$ as shown in Figure 6.8.

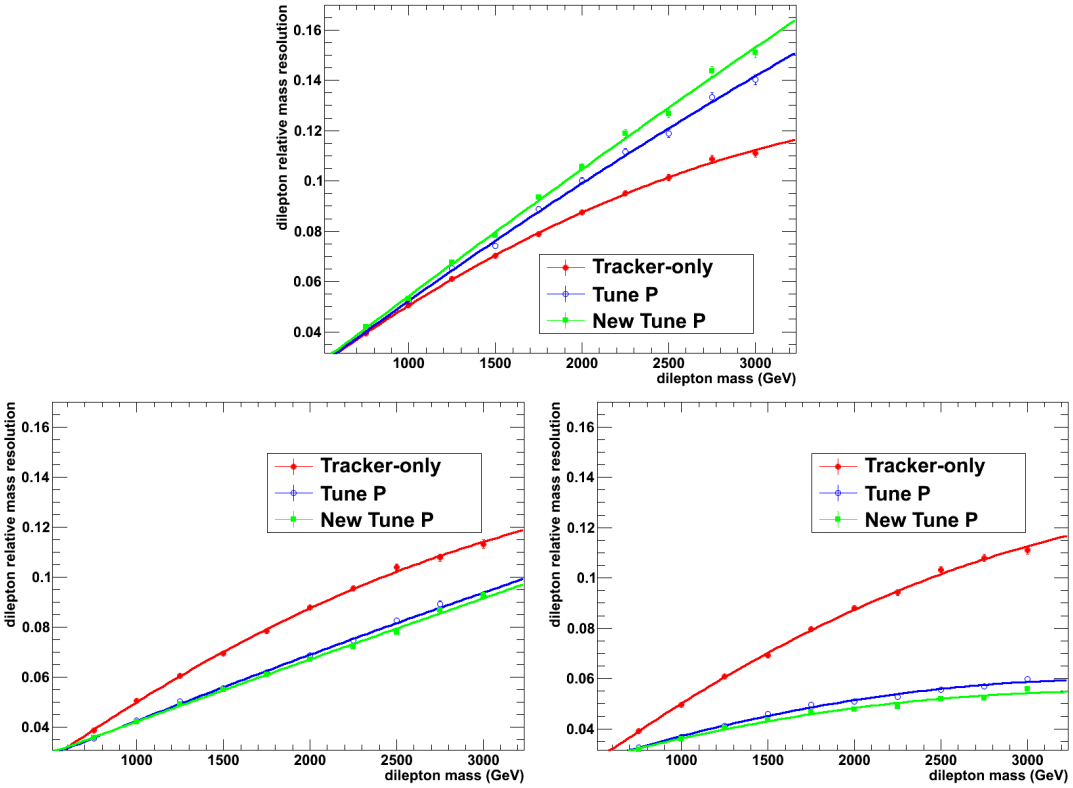

Figure 6.7: Relative invariant mass resolution $\sigma(m)/m$ as a function of dimuon invariant mass for the "tracker-only", "Tune P", and re-optimized "New Tune P" algorithms. The top plot shows results with the old alignment and old muon ID while the left and right at the bottom plots show results with the new muon ID for C1 and C2 alignment scenarios, respectively.

6.8 Background estimation

The largest background in our analysis is from the DY process, which is an irreducible background. After the DY, the next largest background is from $t\bar{t}$ decays. The samples in Table 6.2 allow us to estimate the expected relative background rates for different processes. The $t\bar{t}$ background rate is found to be about 13% of the total background rate for $M_{\mu\mu} > 200 GeV/c^2$. Processes other than $t\bar{t}$, which are $t\bar{t}$ like, where both the muons appear to come from the same vertex most of the time and are rather than from heavy flavor decay (e.g. single top (tW), dibosons, $Z \to \tau^+\tau^-$), contribute

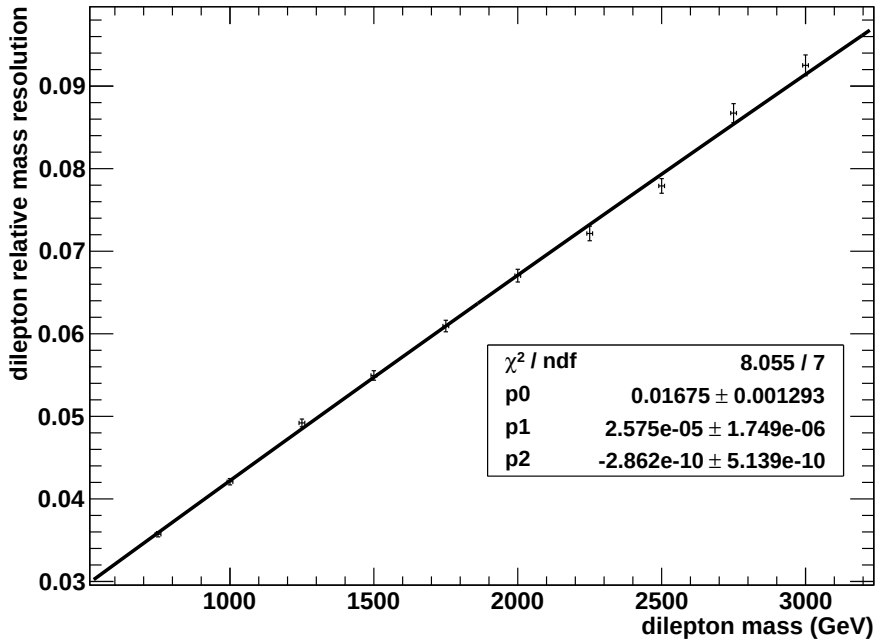

Figure 6.8: Relative invariant mass resolution $\sigma(m)/m$ as a function of dimuon invariant mass for re-optimized "New Tune P" algorithms with the new muon ID for C1 alignment scenario. The distributions are fitted with second-order polynomial whose parameters are shown in the plot.

another 5%. Dimuons in which one or more muon is misidentified are non-prompt sources of muons that arise mostly from W+jets and multi-jet QCD processes contribute less than 1%. Another type of background are dimuons coming from cosmic ray muons traversing the detector near the interaction point and coincident with a collision event to pass our PV requirement can be reconstructed as a pair of opposite-sign muons.

Similar to the 2011 analysis, we have considered the following methods to estimate the non-DY backgrounds:

- For $t\bar{t}$ and $t\bar{t}$-like backgrounds, we use the "eμ" method in which the number of dimuon events is estimated from the electron-muon dilepton spectrum as pioneered in CMS by the HEEP group [71].

- For dibosons and other sources of prompt muons, we check the agreement between the data and simulation by examining the same-sign dimuon spectrum.

- For the background from jets, the rate is estimated from the data using events that fail isolation cuts.

- For dimuons from cosmic ray events, we verify that the contribution is negligible by examining events rejected by anti-cosmics cuts, such as the transverse impact parameter cut.

6.8.1 Drell-Yan background

The main component of the dimuon mass spectrum is due to the DY production. The shape of this contribution to the invariant mass spectrum is obtained from events simulated using the POWHEG event generator interfaced to PYTHIA. The values of the DY cross section in POWHEG in different mass intervals are listed in Table 6.2. We scale them by the ratio of the FEWZz [93] to POWHEG cross sections at the Z peak (1.024) in order to take into account the NNLO QCD corrections. The accuracy of this correction as well as other uncertainties affecting the shape of the DY mass spectrum are discussed in another section. The expected event rates at dimuon masses above the Z peak are normalized to the rates at the Z peak by normalizing the total simulated background in the mass region $60 < M_{\mu\mu} < 120$ GeV to the data.

6.8.2 $t\bar{t}$ and other sources of prompt leptons

The largest background for dimuon analysis after the DY is from $t\bar{t}$. The other sources of prompt leptons are single top, diboson and tau decay. All of these backgrounds

are derived from MC simulations of $t\bar{t}$, tW, $\bar{t}W$ and diboson (WW, WZ, ZZ) production. In order to validate the MC simulation as a good representation of the data, the eμ spectra in the data and from MC simulations are compared. We use 19.6 fb^{-1} of the data from the luminosity sections in which all subdetectors are certified as good (Golden JSON), as described in Section 2. In each eμ pair, the muon is required to pass the full selection as explained in Section 3. For electron identification, we use version 4.0 [94] of the selection used by the HEEP group [95]. In the previous iteration of our analysis, we used the $t\bar{t}$ samples generated with PYTHIA and MADGRAPH event generators. The $t\bar{t}$ background used in this analysis is simulated using POWHEG. The prediction from the simulation is normalized to the luminosity estimate. As in the dimuon analysis, we do not perform rescaling of these distributions to the number of events at the Z peak and fit to a common vertex to calculate the invariant mass. Figure 6.9 and 6.10 show the observed $e^{\pm}\mu^{\mp}$ dilepton invariant mass spectrum and the cumulative distribution, respectively, overlaid with the prediction from simulation.

We use N(eμ) to get an estimate of N($\mu\mu$) in three mass bins: 120-200 GeV, 200-400 GeV, and 400-600 GeV. To derive the $\mu\mu/e\mu$ scale factors, we use simulated $t\bar{t}$ events for which the counts of reconstructed $e\mu$ dilepton and dimuon events in each reconstructed mass bin are shown in Figure 6.11 (a). The red histogram and its error bars shown in (b) represents the scale factors obtained by dividing the two previous histograms bin by bin. The $e\mu$ dilepton and dimuon mass spectra have contributions from other processes, for example, WW, WZ, ZZ, etc. Figure 6.11 (c) shows the relative contribution to the dimuon spectra in each bin for all simulated processes, which contribute to both dilepton and dimuon mass spectra. For the mass range considered, the dominant

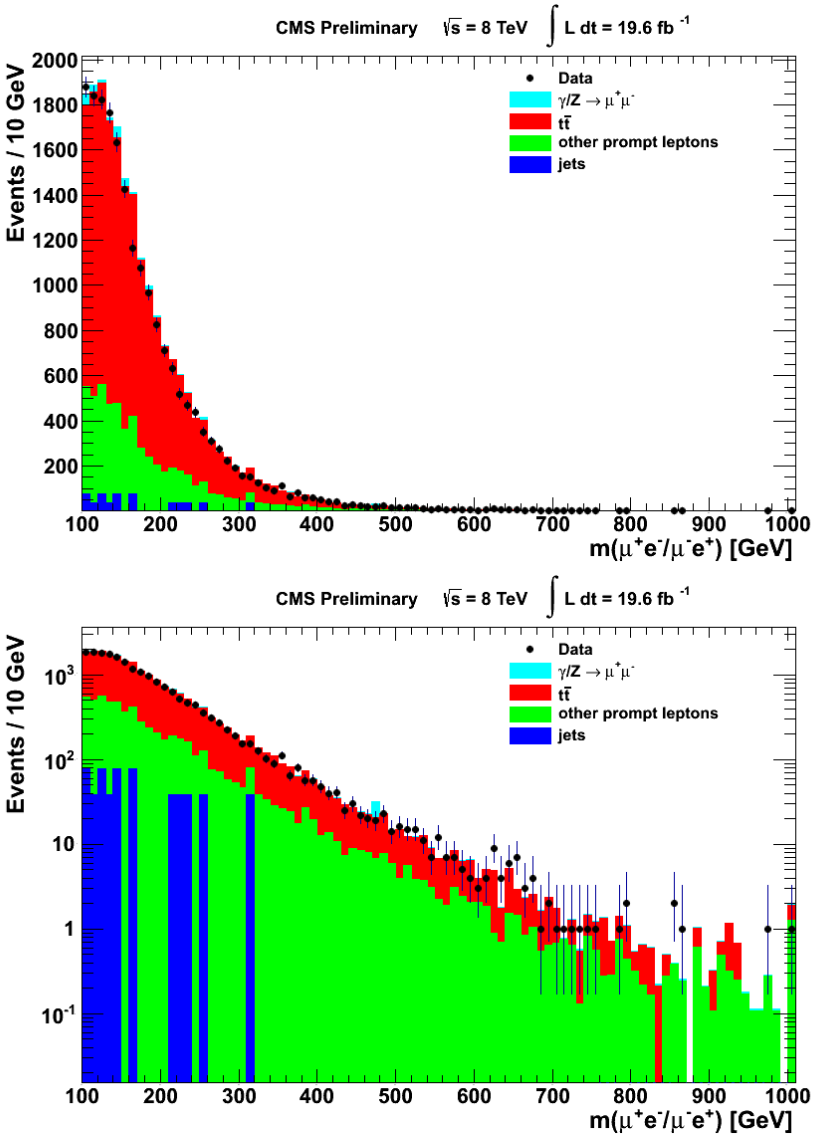

Figure 6.9: The observed $e^{\pm}\mu^{\mp}$ dilepton invariant mass spectrum, overlaid on the prediction from simulation, in linear (top) and log (bottom) scale. "Other prompt leptons" includes the contributions from $Z \to \tau\tau$, the diboson processes WW, WZ, and ZZ, and single top. "Jets" includes contributions from QCD multi-jets and W+jets.

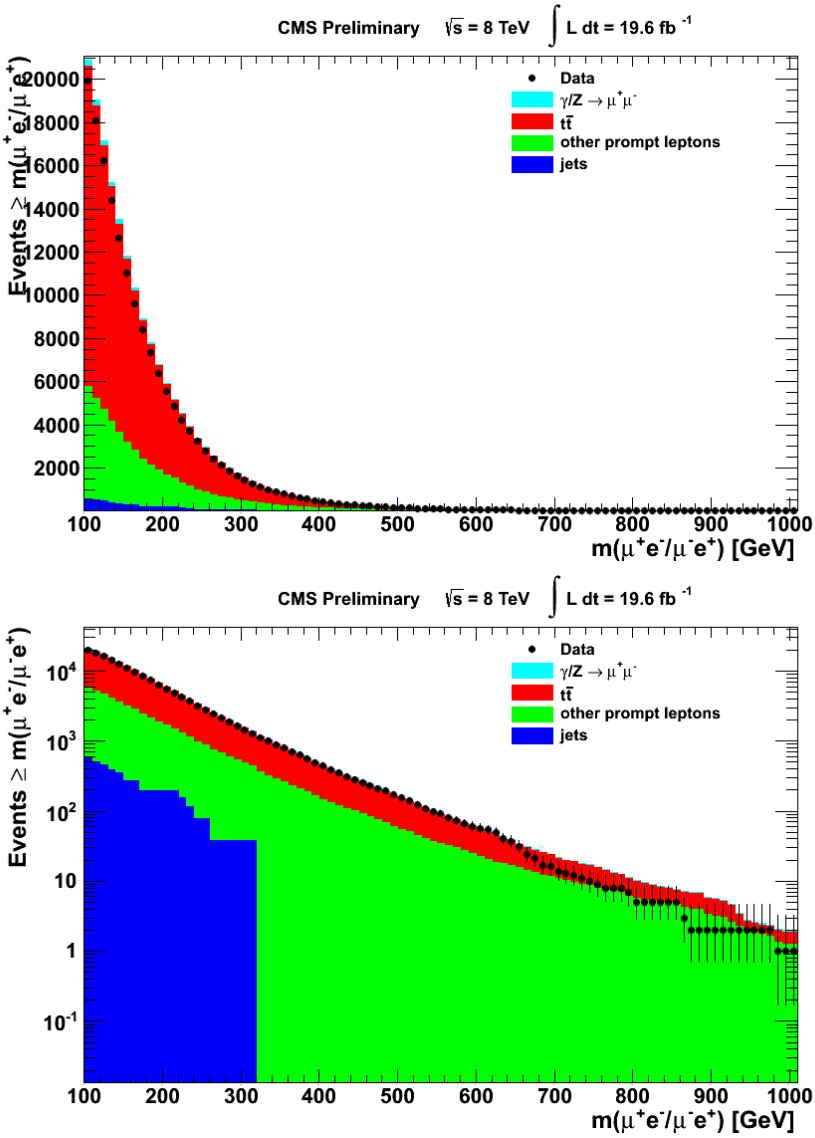

Figure 6.10: Number of $e^{\pm}\mu^{\mp}$ dileptons with invariant mass greater than the given value, overlaid on the prediction from simulation, in linear (top) and log (bottom) scale. "Other prompt leptons" and "Jets" are as described in Figure 6.9 .

contribution is from $t\bar{t}$ sample. The scale factors for the next largest contribution from WW are close to those from $t\bar{t}$ as shown by the blue histogram and error bars in Figure 6.11 (b).

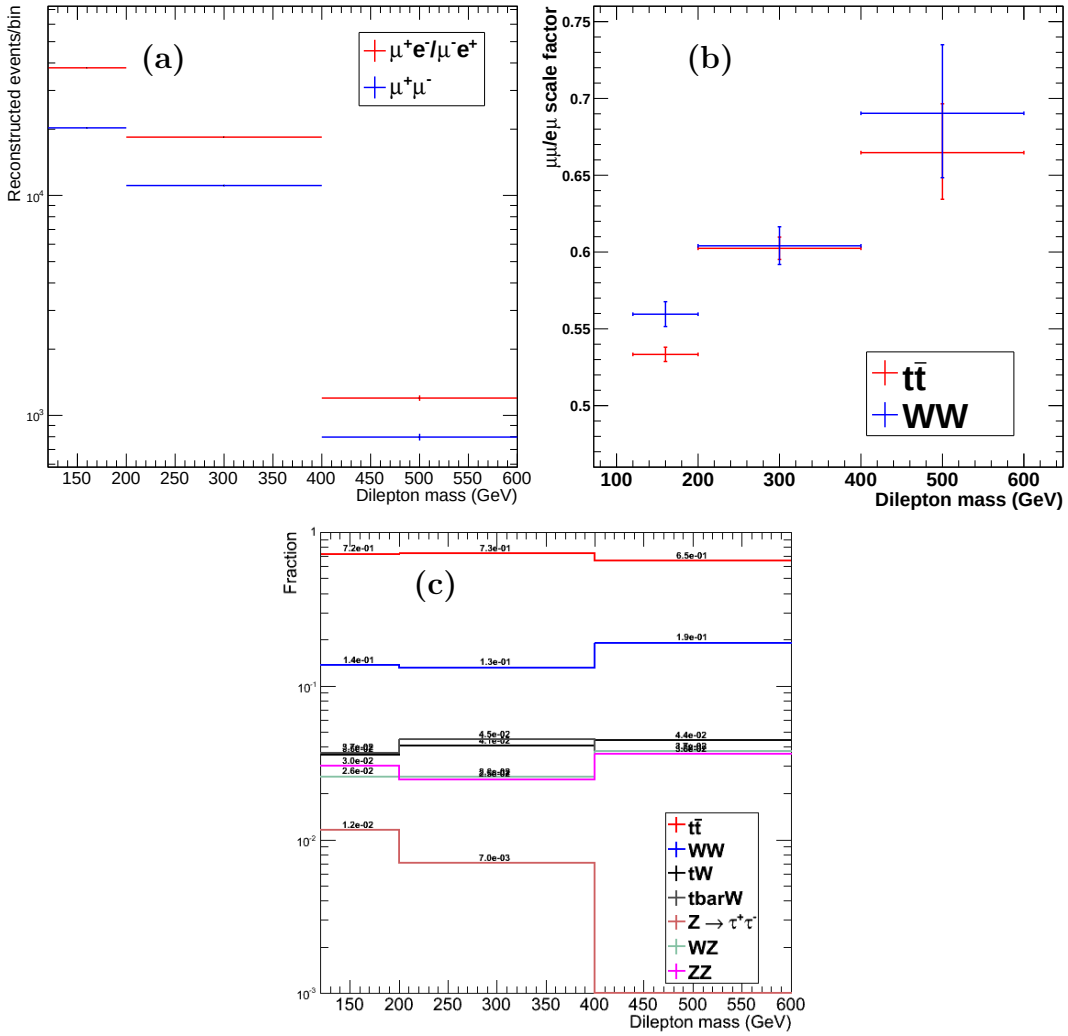

Figure 6.11: (a) The number of simulated $t\bar{t}$ events used to derive the $\mu\mu/e\mu$ scale factors with the binning representing the dilepton mass ranges considered. (b) The $\mu\mu/e\mu$ scale factors derived separately from $t\bar{t}$ and WW simulated samples; the error bars represent statistical uncertainties for ratios of Poisson means. (c) The relative contributions to each reconstructed dimuon mass bin for all simulated processes considered that contribute to both the eμ dilepton and dimuon mass spectra.

Table 6.4 gives the result of applying these scale factors to the numbers of observed $e^{\pm}\mu^{\mp}$ dileptons in the above mentioned mass bins. The numbers of opposite-sign dimuon events from non DY ($t\bar{t}$-like) of prompt muons predicted by the eμ method are in good agreement with the results from the simulation. For example, in the mass range (400-600 GeV) in which we are searching for a resonance signal, the eμ method predicts 253 ± 18 dimuon events, while the simulation predicts 257 ± 18 events. The uncertainty in the former is statistical only, while the uncertainty in the latter includes the uncertainty in the theoretical values of the cross sections for $t\bar{t}$ [96] and other processes, and a luminosity uncertainty of 4.4%.

Mass range	$N(e^{\pm}\mu^{\mp})$ observed	$\mu\mu/e\mu$ scale factor	$N(\mu^+\mu^-)$, eμ prediction	$N(\mu^+\mu^-)$, sim. prediction
120-200 GeV	10684	0.533 ± 0.005	5695 ± 77	5912 ± 391
200-400 GeV	5111	0.602 ± 0.007	3077 ± 56	3223 ± 214
400-600 GeV	381	0.665 ± 0.031	253 ± 18	257 ± 18

Table 6.4: The comparison of numbers of dimuon events predicted using the eμ method to the values from simulation of the relevant processes for few different invariant mass ranges scaled to data. The uncertainties given are the combination of the statistical and systematic uncertainties

6.8.3 Events with misidentified and non-prompt leptons

Another background contribution to this analysis is due to the objects falsely identified as prompt muons. The main source of such background is the misidentification of jets as muons. We estimate the jet related backgrounds using the same strategy used in the analysis of the 2010 and 2011 datasets. We use the "fake rate" method where we define the fake rate as the fraction of loosely isolated muons, which pass the final isolation requirement. This fake rate is derived from a sample of single muons. The difficulty in measuring the fake rate is that the single muon sample has a large contamination from

electroweak sources, such as W, Z, and $t\bar{t}$ decays. We correct for the sample contamination due to EWK sources based on the single muon composition fraction predictions from simulation. To estimate the QCD dijet background contribution, the fake rate measured in bins of p_T and η is applied to a sample of dimuons in which both muons fail isolation. Only a couple of events from the available QCD MC samples pass the isolation requirements; a comparison of the predicted shapes between the data-driven method and the QCD MC is not useful. To estimate the W+jets background, we apply the measured fake rate to a sample of dimuons in which one muon passes and the other fails the isolation requirement. This study was done by others in CMS and is presented in Section 5.5 of [97].

6.8.4 Cosmic ray muon backgrounds

Cosmic ray muons passing the detector near the interaction point with a collision event can be reconstructed as a pair of opposite-sign muons. This background is suppressed by applying cuts on the muon's impact parameters and the 3D angle between muons, and by requiring the presence of a reconstructed primary vertex in the event. Our selection cuts is designed to remove dimuons from cosmic ray muons passing the center of the detector, which requires a primary vertex constructed from other tracks in the event and, not just from the two muon tracks from the cosmic ray muon. At least one of the two muon's transverse impact parameter with respect to the beam must be less than 0.2 cm, and the 3D angle between the two muon's momenta must be less than π- 0.02 radians.

The 3D angle between muons (α) is defined as the difference of π and the angle

between muon tracks in the 3D space. The largest value of α observed in events which could be identified as cosmic muon events by examining the muon timing and impact parameter values, is 2.5 mrad. To estimate the background contribution from the cosmic muon events to our final data sample, we use the fact that the majority of the cosmic events have $\alpha < 0.002$. This background is then reduced to a negligible level by applying the cut on α, which is 99% efficient at rejecting cosmic ray muons [58]. This study was done by others in CMS and presented in Section 5.6 of [97].

6.8.5 Same sign dimuon events as a control sample

Figures 6.12 and 6.13 show comparisons of the observed same-sign dimuon invariant mass spectrum with that expected from the SM processes. All contributions to the expected spectrum are estimated using simulations except for the contribution from multi-jets and W+jets, which are evaluated from the data (negligible contributions using MC samples). The expected distribution is normalized using the observed number of opposite-sign events in the Z peak region with masses in the range $60 < m < 120$GeV. Table 6.5 compares the event count in data to the expected number of events for a few specific invariant mass ranges.

Mass range (GeV)	N($\mu^{\pm}\mu^{\pm}$), observed	N($\mu^{\pm}\mu^{\pm}$), expected
120-200	212	235 ± 35
200-400	114	155 ± 23
> 400	21	18 ± 2

Table 6.5: The comparison of observed and expected numbers of same-sign dimuon events for few different invariant mass ranges. The uncertainties given are the combination of the statistical and systematic uncertainties.

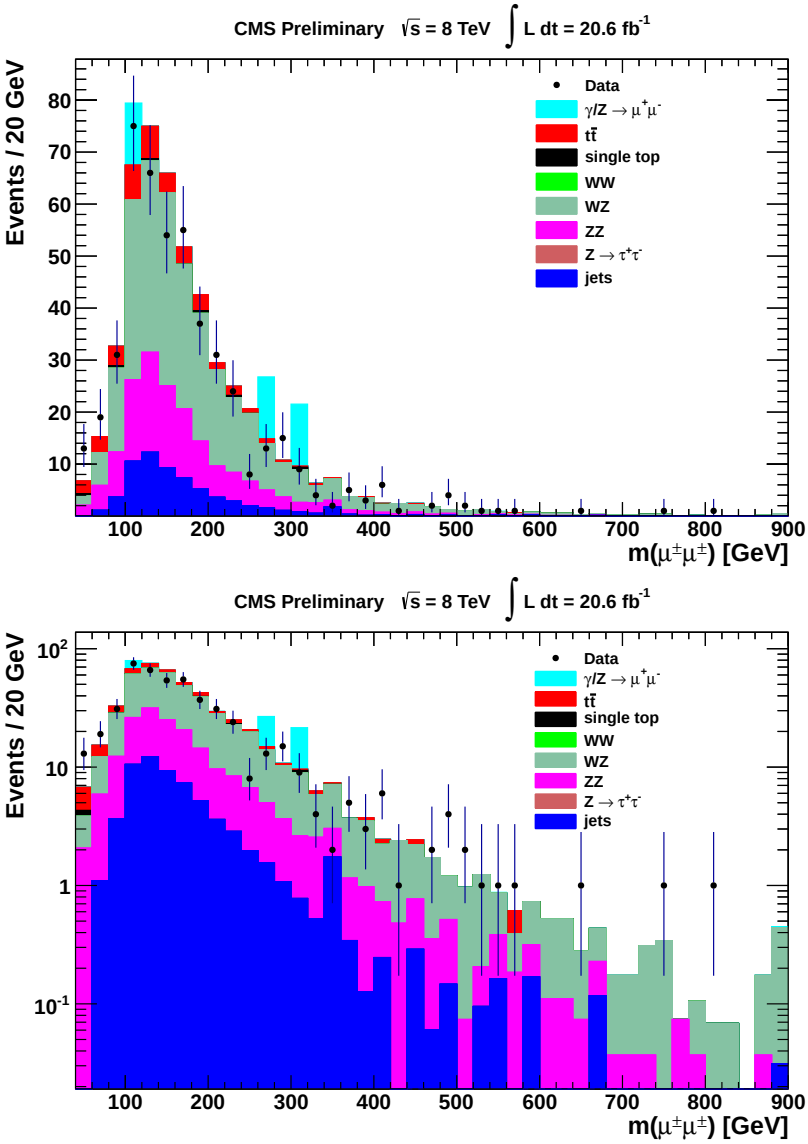

Figure 6.12: The observed same-sign dimuon invariant mass spectrum overlaid on the expected spectrum in linear (top) and log (bottom) scale. Contributions from the diboson, Drell-Yan, $t\bar{t}$, and single top processes are estimated using simulations; "Jets" show contributions from QCD multi-jets and W+jets evaluated from the data.

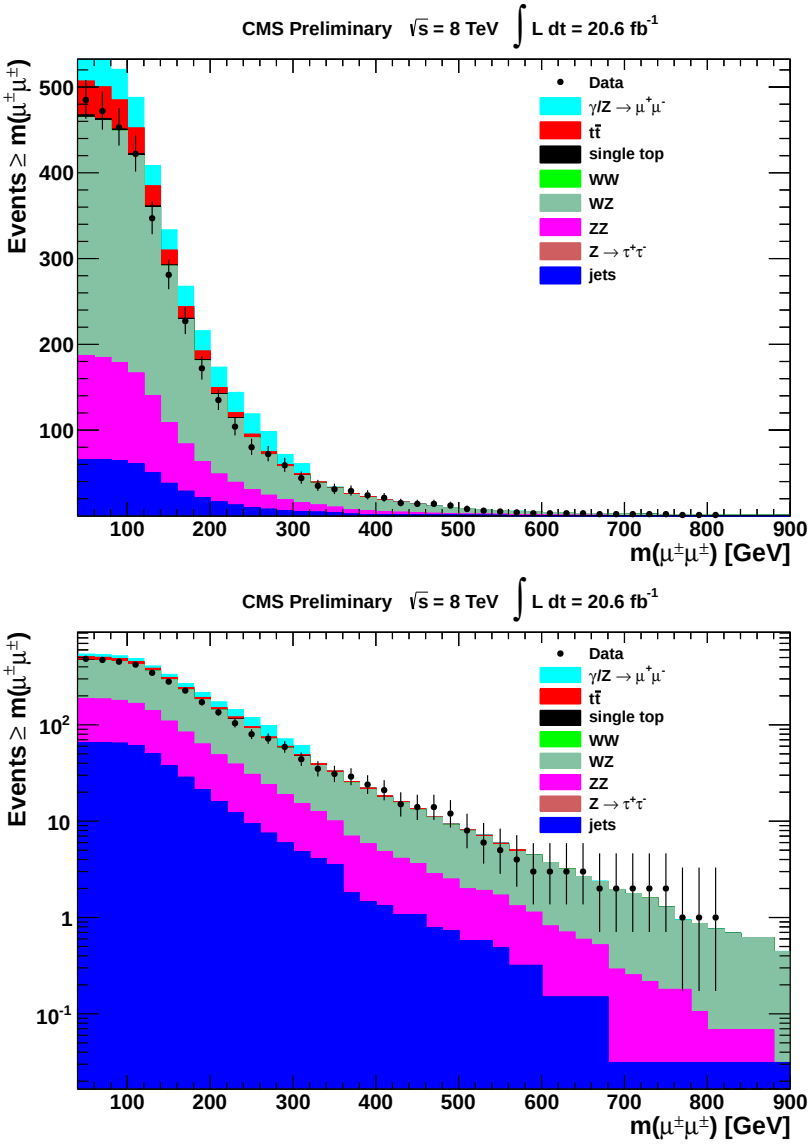

Figure 6.13: Number of same-sign dimuons with invariant mass greater than the given value, overlaid on the corresponding distribution for the expected number of same-sign dimuons in linear (top) and log (bottom) scale. All contributions to the expected spectrum are estimated as described in Figure 6.12.

According to the predictions, the most important contributions to the same-sign sample of events are from WZ and ZZ and from jet related backgrounds. The counts tabulated above show good agreement between the data and prediction. The uncertainties in these measurements is dominated by statistical errors and jet related backgrounds. This agreement indicates our evaluation of the backgrounds from dibosons and misidentified jets is accurate. As the expected and observed contribution from these backgrounds are small, it does not affect the opposite-sign dimuon events and the results of our studies.

6.9 Data/MC comparisons

In this section, we compare distributions of the analysis related variables between the data and the prediction from the MC simulation of the contributing SM processes. Our main focus is on the dimuon mass spectrum where we expect a signal. We also compare basic distributions, such as those of muon/dimuon kinematic variables. The results presented here are based on the full 2012 dataset that correspond to the integrated luminosity of 20.6 fb^{-1}. The distribution from each simulated sample is scaled by weights derived from the information in Table 6.2.

The total simulated background contribution is normalized to the data in the region of Z peak $60 < m < 120$ GeV. The $\text{p}_\text{T} > 45$ GeV selection requirement on the muons removes most of the events in this mass range and the mass distribution of the remaining events is shaped by this cut. Therefore for the normalization, a prescaled trigger identical to the main muon trigger except for a lower p_T cut is used to select events, which is 27 GeV. The rescale factor due to this normalization is equal to 0.9956.

Figure 6.14 shows the comparison of the observed opposite-sign dimuon invariant

mass spectrum with that expected from the SM processes. All contributions to the expected spectrum are estimated using MC simulations except for the contribution from QCD multi-jets and W+jets, which are evaluated from the data because the contribution from MC samples is negligible. The observed and the expected spectra are in good agreement, shown by the cumulative distribution in Figure 6.15 and in the ratio of the observed and expected numbers of opposite-sign dimuons shown in Figure 6.16. Figure 6.17 shows the comparison of muon and dimuon kinematic variables between the data and simulation.

The observed and the expected numbers of events in the control region m = 120-200 GeV and in the search regions $m > 200$ GeV and $m > 400$ GeV are listed in Table 6.6 where the uncertainties include both statistical and systematic components added in quadrature. Systematic uncertainties in the dominant DY background are discussed in another section. The $t\bar{t}$ background uncertainty is taken to be 6.7% due to the uncertainty in the $t\bar{t}$ cross section [96]. The uncertainties in the predicted number of $t\bar{t}$-like background events are taken from uncertainties in the total cross sections and are in the range of 3-7%. In the high mass region, the cross sections are less well known and the uncertainties are small with respect to statistical uncertainties. The uncertainty in the jets backgrounds is taken to be 100%.

6.10 High mass dimuon events

The events with dimuons having mass above 900 GeV/c^2 are rare and it is important to check the response of the detector at these scales. The properties of the tracks detected in the muon chambers were examined to make sure they correspond to the expectation for high energy muons. Similarly, the energies in the ECAL and HCAL were

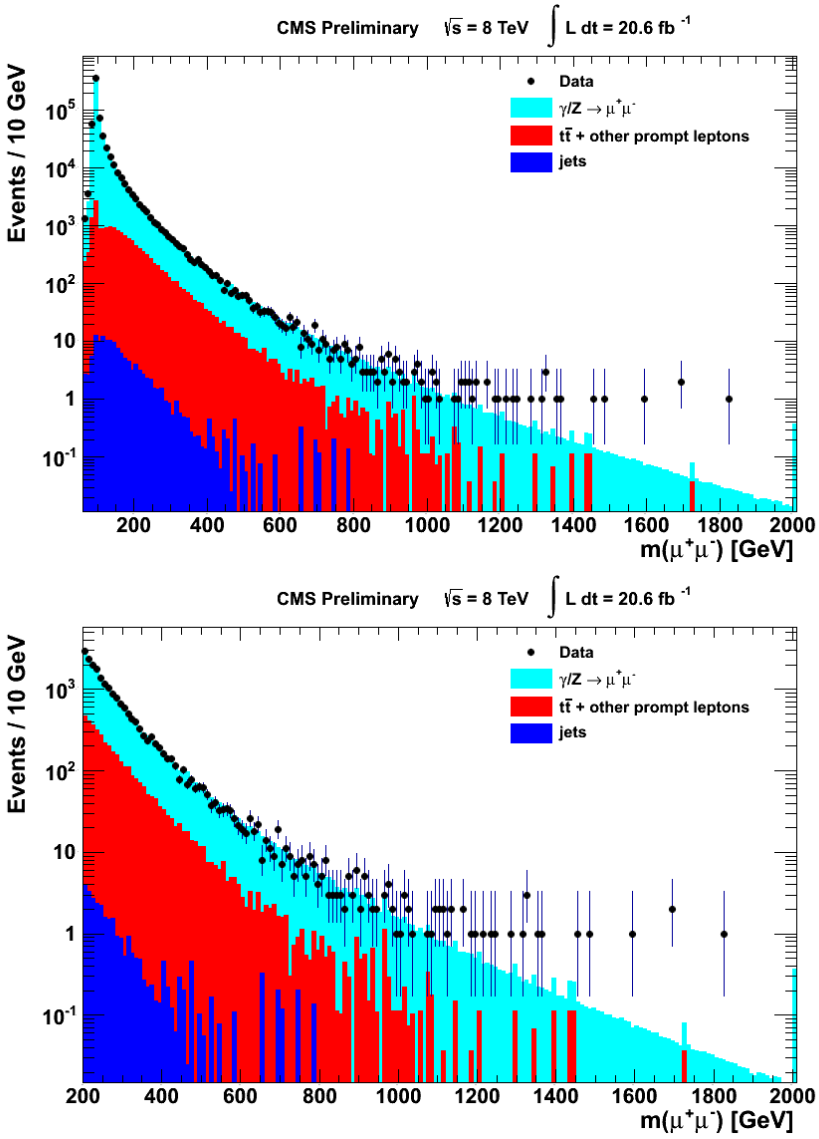

Figure 6.14: The observed opposite-sign dimuon invariant mass spectrum overlaid on the background prediction."Other prompt leptons" includes the contributions from $Z \to \tau\tau$, the diboson production WW, WZ, and ZZ, and single top tW , $\bar{t}W$. "Jets" includes contributions from QCD multi-jets and W+jets, estimated from the data. The bottom plot shows the dimuon invariant mass greater than 200 GeV to better see the high mass points.

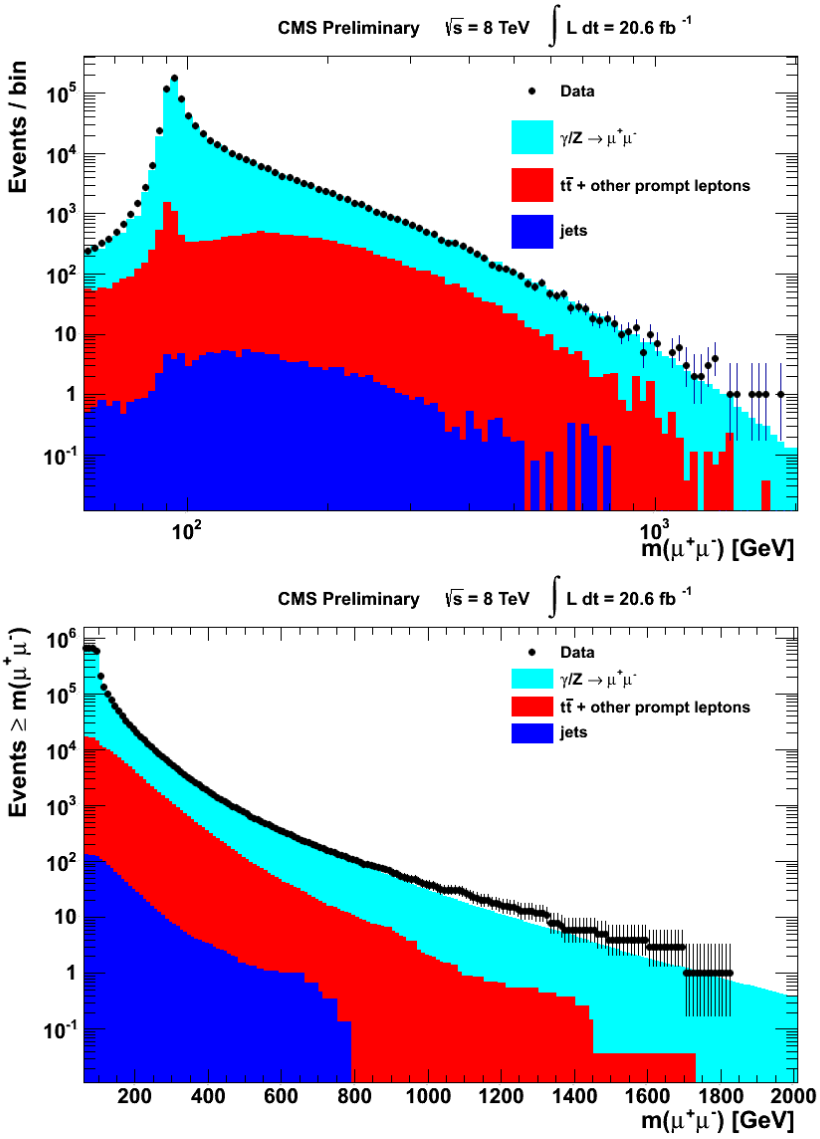

Figure 6.15: The observed opposite-sign dimuon invariant mass spectrum overlaid on the background prediction in logarithm scale (top) and the number of opposite sign dimuons with invariant mass greater than the given value overlaid on the background prediction (bottom). "Other prompt leptons" and "Jets" are as described in Fig. 6.12 .

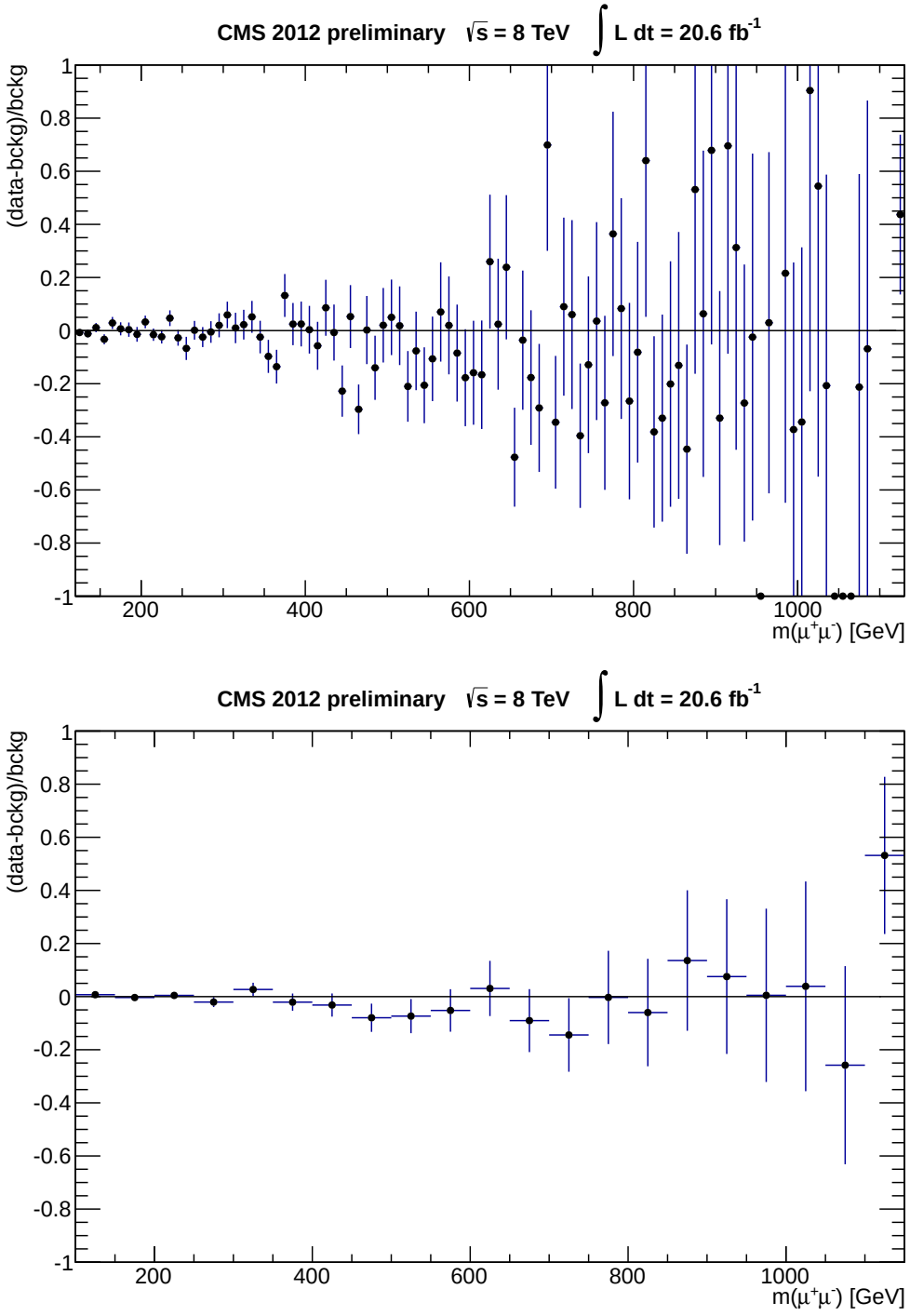

Figure 6.16: The ratio of the observed and expected numbers of opposite-sign dimuons minus unity shown as a function of the invariant mass in the mass range 120-1120 GeV, in 10 GeV (top) and in 50 GeV (bottom) bins. The error bars include statistical uncertainties only.

Source	Number of events		
	120-200 GeV	$>$ 200 GeV	$>$ 400 GeV
Data	78129	19982	1710
Total background	78505 ± 3515	20061 ± 793	1791 ± 55
Z/γ^*	72227 ± 3502	16329 ± 772	1477 ± 53
$t\bar{t}$	4502 ± 303	2655 ± 180	195 ± 15
Other prompt leptons	1718 ± 51	1048 ± 33	116 ± 5
Multi-jets and W+jets	58 ± 58	29 ± 29	3 ± 3

Table 6.6: Number of opposite-sign dimuon events with invariant mass in the control region 120-200 GeV and in the search regions $m > 200$ GeV and > 400 GeV. Monte Carlo simulation is used for all backgrounds except for multi-jets and W+jets, which were evaluated from the data."Other prompt leptons" includes the contributions from $Z \to \tau^+\tau^-$; the diboson production WW, WZ, and ZZ; and the single top (tW) events. Uncertainties include both statistical and systematic components added in quadrature.

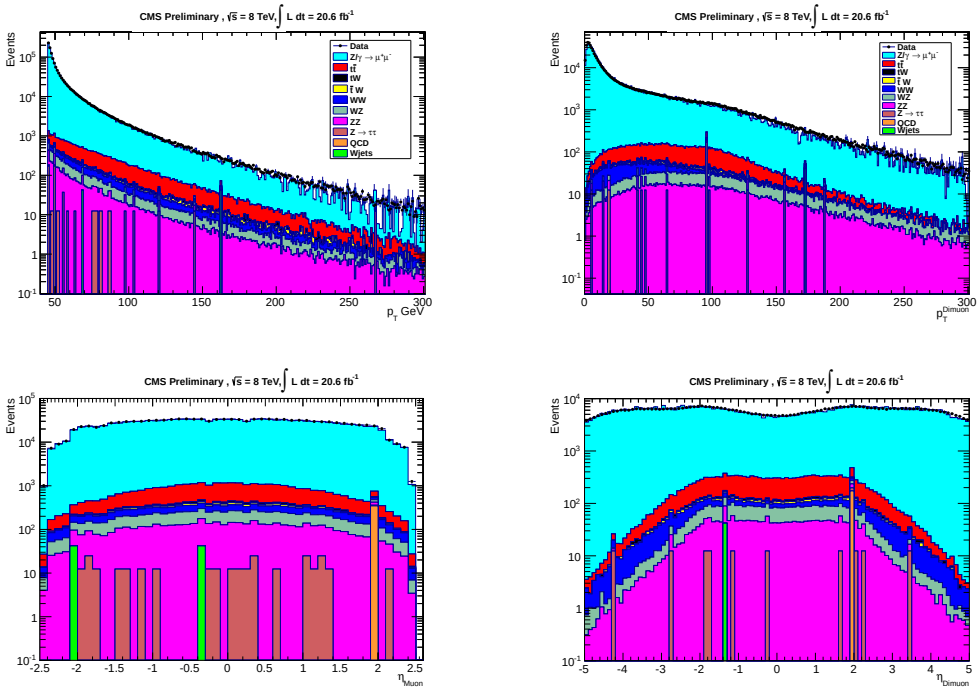

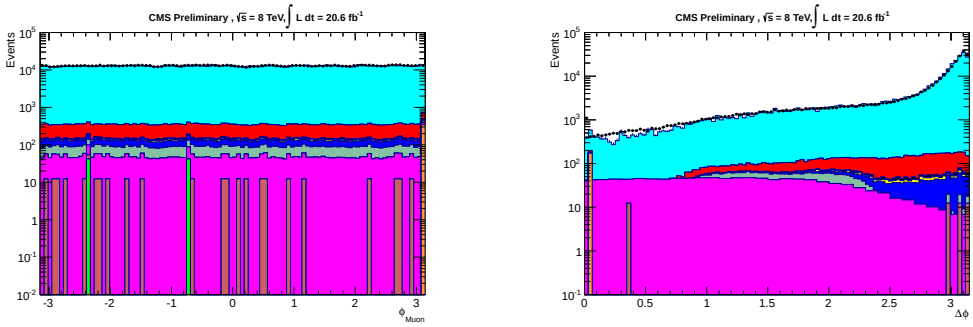

Figure 6.17: Comparison between the data and simulation for kinematic quantities of muons. In the top and middle plots, the variables are transverse momentum pT and pseudorapidity η for muon and dimuons; in the bottom plots, these are azimuthal angle ϕ for muons and the difference in the two muons azimuthal angles, $\Delta\phi$.

checked in order to exclude the possibility of a high energy hadron punching through the calorimeter. Further checks against cosmic ray muons were performed based on the distribution of the impact parameter and timing of the muon signals with respect to other tracks in the event. These checks confirm a negligible contribution from cosmic ray muons. The quality of the tracks in the silicon tracker was scrutinized and all tracks found to be of good quality. Similarly the vertices formed by the two muon tracks were found to be good. There is no evidence of any defect in the events at high mass.

Table 6.7 and 6.8 give the dimuon events with mass of above 900 GeV/c^2. There are 62 dimuon pairs with mass exceeding 900 GeV/c^2; out of these, 38 events have dimuon mass above 1.0 TeV/c^2. Event displays for the two highest mass dimuon events reconstructed in the CMS detector are shown in Figure 6.18.

6.11 Normalization to Z resonance

We count events in the mass range of 60-120 GeV and perform background subtraction using the event counts from non-Z MC samples rescaled by the data simulation

Run Number	Event number	Lumi section	$M_{\mu\mu}$ (GeV/c^2)
199409	676990060	553	1824
202178	1100609921	931	1697
205694	416479300	398	1694
206207	186909124	153	1592
207924	209747123	215	1486
195378	225870452	193	1453
199409	654043540	531	1367
204601	12780117291	1215	1357
196433	39187003	77	1327
199833	1136357968	1054	1325
194050	936530164	995	1322
199812	636694094	541	1319
196431	66057632	90	1290
208391	845554877	666	1248
207492	65524201	78	1232
198969	779619791	641	1212
202087	421813187	323	1192
204563	499818262	368	1188
194912	739866334	444	1168
199571	109753290	97	1166
199753	42023310	40	1136
202237	509578194	327	1130
198487	1150495912	1075	1125
202504	919226848	733	1114
194225	14353212	13	1112
206869	629195087	685	1109
191718	211765901	171	1106
193621	1067285891	1359	1097
198271	802097775	699	1095
201624	250169307	194	1083
194424	909915359	654	1077
207922	55833120	50	1030
204563	272281825	221	1029
208487	170918748	96	1023
194150	302855323	244	1018
204601	252896431	186	1017
195915	836688041	556	1014
207273	47981615	39	1006

Table 6.7: List of dimuon events in the data with masses above 1.0 TeV/c^2 in full 2012 data.

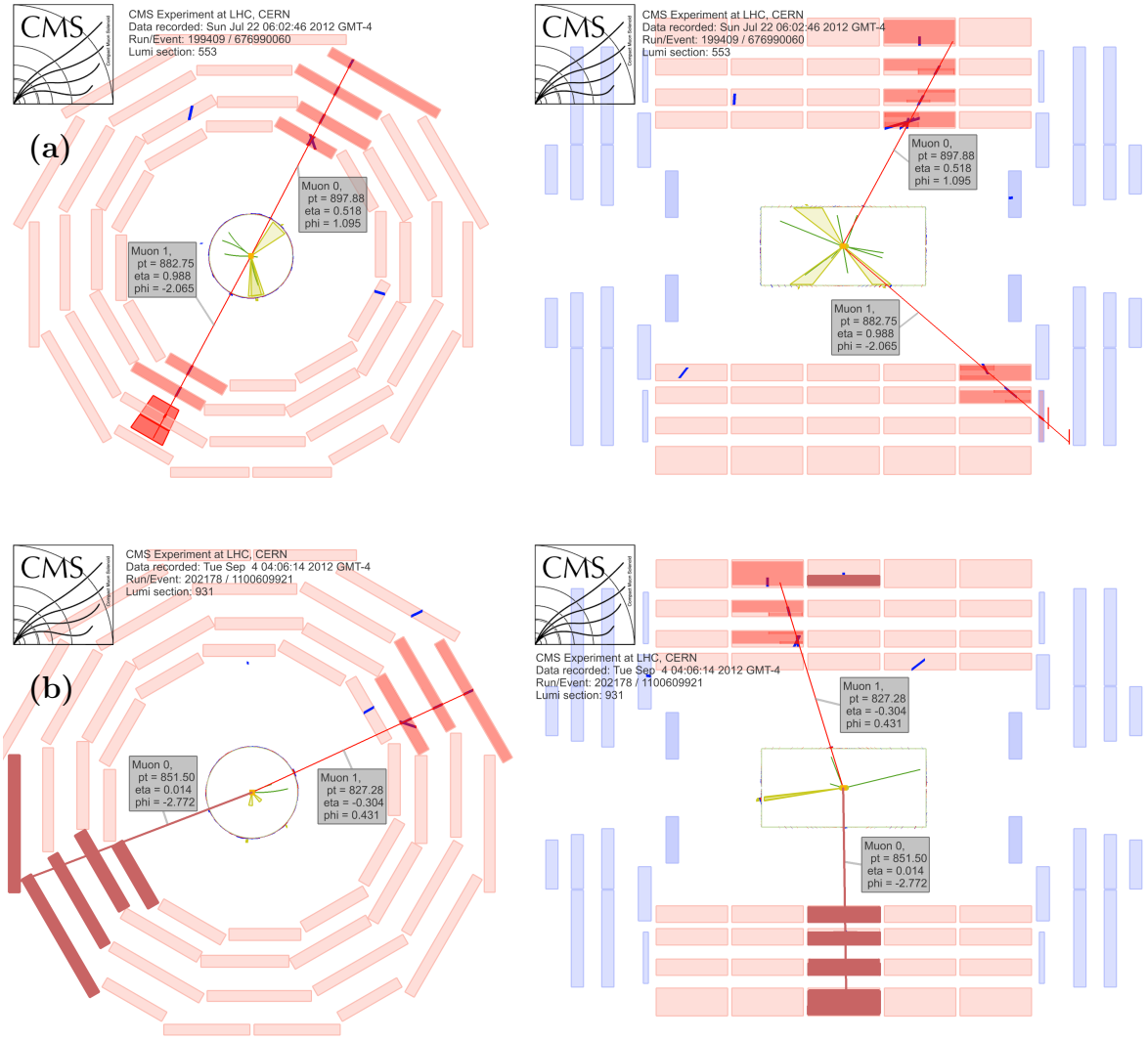

Figure 6.18: Event displays of the two highest-mass $\mu^+\mu^-$ events: Left (right) side of figures (a) and (b) show the transverse (longitudinal) view. (a) This display corresponds to the highest mass (1.824 TeV/c^2) dimuon event with muon kinematic variables: p_T = (898,883) GeV/c, η = (0.52, 1.10), and ϕ = (0.99, -2.07). (b) This display corresponds to the next highest mass (1.697 TeV/c^2) dimuon event with muon kinematic variables p_T = (851, 827) GeV/c, η = (0.01, -2.77), and ϕ = (-0.30, 0.43), which is also shown in the display.

Run Number	Event number	Lumi section	$M_{\mu\mu}$ (GeV/c^2)
207884	4187119	4	995
202328	589121740	394	986
206187	274374421	215	983
199008	179760542	160	976
194115	257882341	280	974
205667	42407203	39	974
201173	145943466	167	974
199436	119847245	166	965
196027	153238373	99	964
202060	527655267	413	961
201669	104849581	57	946
206243	974886749	676	945
195774	94924923	48	938
206744	605265207	431	934
199574	60631621	79	928
194533	85367726	82	927
195397	673031590	472	923
196218	860336640	591	918
198230	738690849	802	918
194050	1391733189	1568	916
199008	721792661	591	913
201202	312065562	341	911
195552	1774851027	1611	908
202060	1016136621	847	906

Table 6.8: List of dimuon events in the data with masses in the range 900-1000 GeV/c^2 in full 2012 data.

scale factor on the Z peak. We use the single muon trigger with the p_T threshold of 40 GeV, which requires the offline muon p_T of at least 45 GeV and has low efficiency for events in the Z peak normalization window. Therefore, we use a prescaled trigger path, HLT_Mu24_eta2p1, with corresponding offline p_T threshold of 27 GeV to select events in the Z peak normalization window using the selection identical to our primary. The efficiency times acceptance for the combination of such prescaled trigger and the selection used is estimated from the simulation to be 32.6%. The data

to simulation efficiency scale factor for both the online and the offline event selections is 0.987 ± 0.011. The largest overall (L1+ HLT) prescale factor of the trigger HLT_Mu24_eta2p1 used during the 2012 data collection is 300. In the samples of data collected with the prescale factor smaller than 300, we remove events at random to achieve an overall prescale factor of 300. By doing so, we found 24502 events in the Z mass window in the data. The estimated contribution from non-Z sources is equal to $\approx 0.5\%$, leading to a subtraction of 114 events. We calculate the cross section of Z events, which is found to be $1.101 \pm 0.008(\text{stat.}) \pm 0.012(\text{syst.}) \pm 0.044(\text{lumi})$ nb, consistent with both the theoretical (NNLO) cross section of 1.117 ± 0.053 nb and the value of $1.12 \pm 0.01(\text{stat.}) \pm 0.02(\text{syst.}) \pm 0.05(\text{lumi})$ nb measured by the Standard Model Physics (SMP) group [98].

The dominant uncertainty on the ratio of the geometrical acceptances and other related theoretical considerations is that the acceptance of Z bosons is much smaller than that of heavier mass. The uncertainty in the acceptance of the Z boson has been studied by VBTF and SMP groups. The analysis [99] estimated this uncertainty to be 1.9%, which has a similar definition of acceptance as ours. We assign this uncertainty to the ratio of acceptances $A(Z)/A(Z')$. The evolution of the triggering and reconstruction efficiency from the Z peak to higher masses is taken from the simulation as in the 2010, 2011 analyses. The overall variation in the ratio of efficiencies, due to the increasing probability of muons showering, is of the order of 2.5%, which we consider as the systematic uncertainty on the ratio of efficiencies. Considering these two uncertainties, we assign an overall normalization-related systematic uncertainty of 3%.

6.12 Statistical analysis

6.12.1 Signal and background shapes

As discussed in Section 6.6, the dominant background comes from the DY process. The rest of the backgrounds is from $t\bar{t}$, single top, dibosons and jets (QCD multi-jets, W+jets). We perform a shape analysis using an unbinned maximum likelihood fit of dimuon invariant mass to differentiate between the smooth background and a resonant peak. As in previous iterations of the analysis, the probability density function for the signal, $p_s(m \mid \Gamma, M, w)$ is modeled as a convolution of a Breit-Wigner of width Γ and mass M with a Gaussian of width w accounting for mass resolution smearing. The shape of the background dimuon mass spectrum is parameterized as:

$$p_b(m \mid a, b, k) = e^{-am+bm^2} m^{-k} \tag{6.2}$$

where a, b and k are fit parameters of the background shape. In previous analyses (2010, 2011, and ICHEP 2012), we parameterized the shape of the dimuon spectrum from the DY background alone. In this analysis, we consider all the contributing SM backgrounds including DY as suggested by the Exotica group. We use the parameterization obtained from the fits to the total expected background spectrum, which includes $t\bar{t}$ and other reducible backgrounds. Adding non-DY backgrounds to the fitted mass spectrum changes the background shape slightly, yielding parameterization that falls more steeply with the mass.

The parameters of the background shape are determined by a fit to the simulated dimuon mass spectrum in the mass range 200 - 3000 GeV as shown in Figure 6.19. We

have changed the fit function in this analysis as shown in Equation 6.2. A quadratic term in the exponential is added in order to improve the fit at very high invariant masses, $m \gtrsim 2500$ GeV. The parameters extracted from fits to the mass distribution representing a weighted sum of the DY backgrounds generated with the C1 misalignment scenario and all other contributing SM backgrounds are a = 0.002293, $b = 3.315 \times 10^{-8}$ and k=3.646. The results of the fits performed in different mass windows in the 200 - 3000 GeV range differ from those obtained for the entire mass range by less than 2%.

A comparison of the DY background mass spectra for the three available misalignment scenarios is shown in Figure 6.20. From the plots, we can see improvement in the momentum resolution with the background rate at $M_{\mu\mu} = 2$ TeV decreasing by 8-10% for the new alignments. This difference between C1 and C2 stays within 5% in the mass region up to 2 TeV. We assign this difference as a systematic uncertainty in the background shape due to alignment uncertainties.

6.12.2 Input to limit setting

As shown in the previous section, the observed invariant mass spectra agree with expectations based on SM processes. We do not see any significant excess in our invariant mass spectrum; limits are set on the possible contributions from narrow resonances. We use the shape based Bayesian limits procedure as was done previously in the 2010, 2011 and early 2012 analyses. In order to set limits, the background shape, the signal acceptance times efficiency, and the mass resolutions are parameterized as a function of mass. The input to the limit setting tool is summarized in Table 6.9. The number of Z events in the range of 60-120 GeV, the Z acceptance times efficiency, the data to

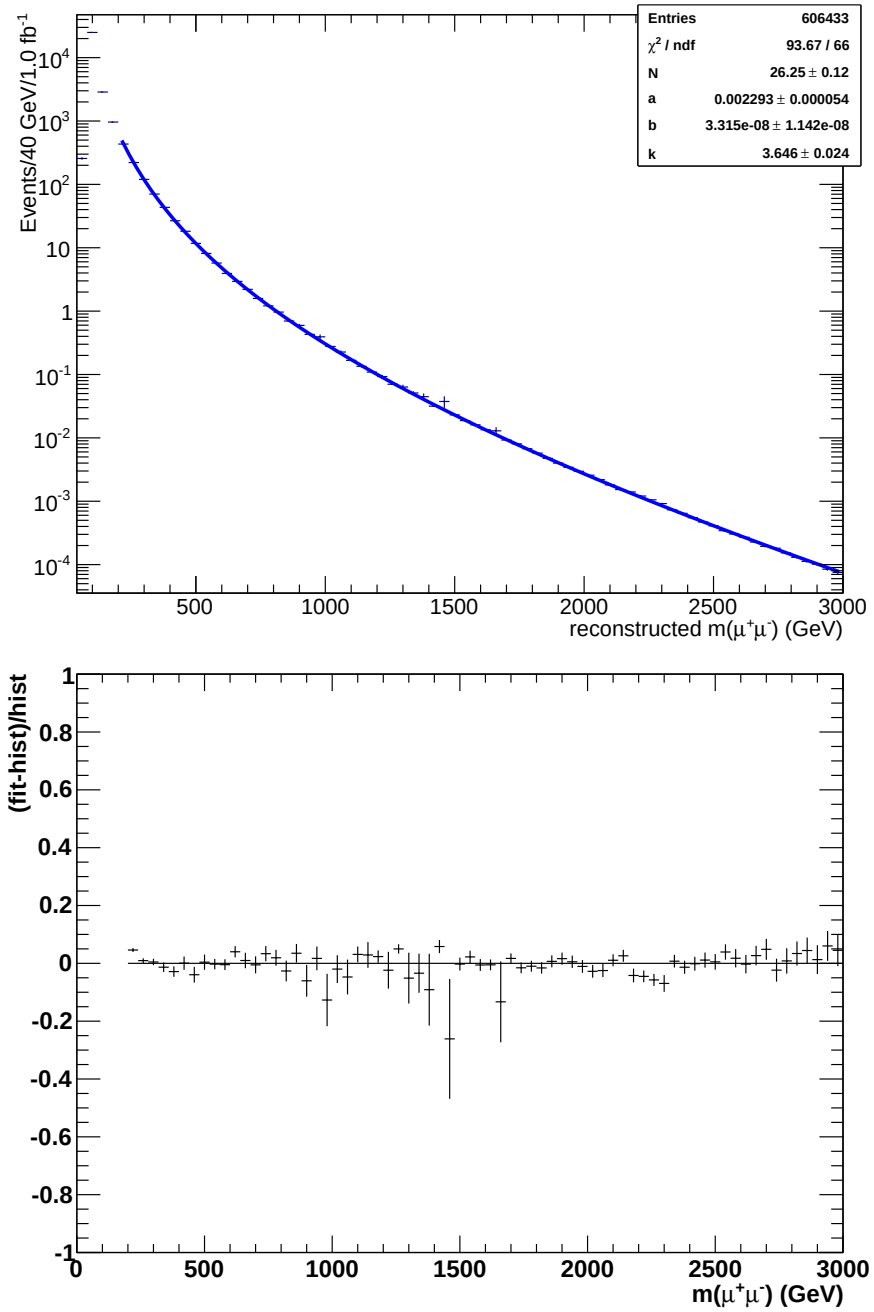

Figure 6.19: Fit to the simulated dimuon mass spectrum including DY and other SM backgrounds (top) and the residuals as a function of the invariant mass (bottom).

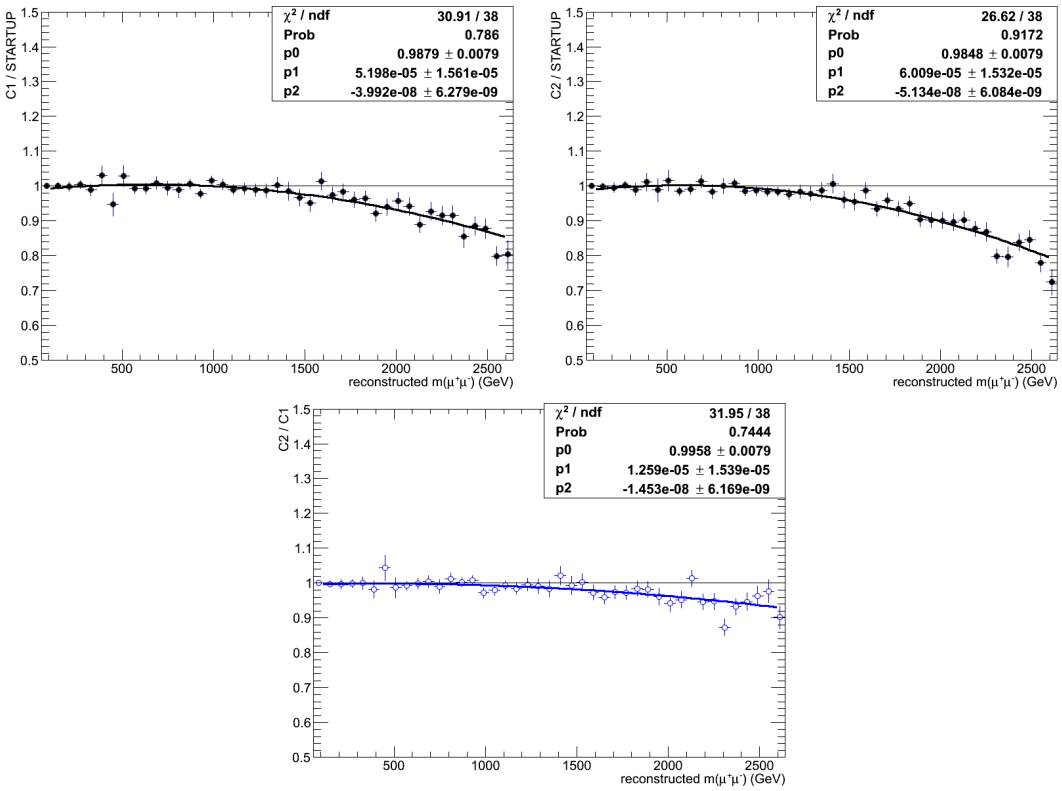

Figure 6.20: The impact of alignment on the background shape. The plots show ratios of event yields as a function of dimuon mass for different pairs of alignment scenarios considered. The two plots on the top show the ratios of C1 (left) and C2 (right) alignments over the old STARTUP; the bottom plot shows C2 over C1.

simulation efficiency scale factor, and the uncertainty in the Z′ to Z normalization are derived as described in the previous section. N_{data} and N_{bkg} are the number of events in the data; the estimated background in the specified mass range is reported in Table 6.6. The parameterization of Z′ acceptance times efficiency as a function of the dimuon invariant mass is taken from the fit in Figure 6.3 of Section 6, the mass resolution from Figure 6.8 of Section 7 and the background shape from Figure 6.19 of this section.

Input	Value
N_Z in 60-120 GeV from prescaled trigger (background subtracted)	24388
Zacc. $\times$ eff. in 60-120 GeV / prescale factor	0.326/300
Data/MC efficiency scale factor	0.987 ± 0.011
Z′acc. $\times$ eff./Zacc. $\times$ eff.uncertainty	3%
N_{data} in $m > 200$ GeV	19982
N_{bkg} in $m > 200$ GeV	20061
N_{bkg} uncertainty	20%
Z′acc. $\times$ eff.	$0.81 - 1.54\times10^{8}/\left(m+585\right)^{3}$
Mass resolution	$0.01675 + 2.575\times10^{-5}m - 2.862\times10^{-10}m^{2}$
Background shape	$\exp\left(-0.002293m + 3.315\times10^{-8}m^{2}\right)\cdot m^{-3.646}$

Table 6.9: The input parameters to the limit setting code. Masses m are in GeV.

6.12.3 Systematic uncertainties

The main sources of systematic uncertainties are theoretical uncertainties (parton distributions, higher-order corrections, etc.), uncertainties from an imperfect knowledge of the detector (alignment, calibration, magnetic field), and uncertainties in the fitting procedure (background shape, functional forms of pdfs, mass resolution, etc.). Since our analysis technique explores only the difference in shape between the mass spectra of the signal and the background and because the limits are set on the ratio R_σ of $\sigma\times$ BR for high mass resonances to that for the Z boson, a number of experimental and theoretical uncertainties have a negligible or small impact on the results. For example, only the mass dependence of the uncertainty in the muon reconstruction efficiency needs to be taken into account, not the absolute uncertainty. The same is true for the trigger efficiency and for the uncertainty in the mass scale. Among those uncertainties that do not cancel out in the ratio R_σ, the uncertainty in the background shape is potentially the most important.

As discussed above, the background shape is determined from fits to background mass spectrum predicted by the MC simulation. This MC based shape is found to agree

well with the observed background shape in the control region of low masses where the number of events observed in the data is sufficient for a quantitative comparison. The issue is then the reliability of the background prediction in the high mass signal region. The accuracy of the prediction depends, among other things, on how accurately the simulation models the extreme tails of the detector resolution function from low mass to high mass in the steeply falling background spectrum. As effects like these are much difficult to control, the statistical procedure used to quantify the results of our searches [100] is designed in such a way that minimizes the sensitivity of results to the uncertainties in the background shape. This is achieved by keeping the fit region relatively narrow so that the statistical uncertainty dominates and the results are insensitive to the functional form used to describe the background. Only events in a window of $\pm$ 6 times the mass resolution around the probed signal mass are included in the likelihood fit. At high masses, the lower edge of the window is adjusted so that there is a minimum of 400 events in the window, which effectively translates into a lower mass cut of $M_{\mu\mu} \gtrsim 600$ GeV. The systematics studies are performed by others in collaboartion, and the results are presented only here. The following sources of uncertainties in the background shape have been studied and taken into account:

- Mass dependent uncertainty in the triggering and reconstruction efficiency are taken from simulation as the full difference between the efficiency at M(Z) and at higher masses. It increases from about 1% at $M_{\mu\mu} = 1$ TeV to 3.5% at $M_{\mu\mu} = 3$ TeV.

- Uncertainty in the mass resolution, resulting mostly from alignment uncertainties, is evaluated as the difference between the background shapes predicted by the C1

and C2 misalignment scenarios as discussed in Section 6.11. It varies from 0.6% at $M_{\mu\mu}$ = 1 TeV to about 10% at $M_{\mu\mu}$ = 3 TeV.

- The impact of PDF uncertainties on the cross section of the dominant DY background is evaluated using FEWZ [93] following the recommendations from the PDF4LHC group [101]. The estimates are based on the MSTW2008 [102], CTEQ12 [103], and NNPDF21 [104] NLO PDF sets. The overall uncertainty from the three PDF sets combined varies from 7% at $M_{\mu\mu}$ = 1 TeV to about 30% at $M_{\mu\mu}$ = 3 TeV [105].

- Uncertainty due to higher order electroweak (EWK) effects is taken as the full size of the mass-dependent corrections for the DY background derived in [106]. This corresponds to 3.2% at $M_{\mu\mu}$ = 1 TeV and 12% at $M_{\mu\mu}$ = 3 TeV.

- Uncertainty due to residual mass-dependent NNLO QCD corrections not taken into account by the rescaling of the DY background described in Section 6.7.1 is believed not to exceed 2-3% in the mass range up to $M_{\mu\mu}$ = 2 TeV [105] and is neglected.

Systematic uncertainties explicitly modeled in the limit calculations [100] are uncertainty in the ratio of acceptance times selection efficiency for signal to acceptance times selection efficiency for the Z boson in Equation 6.1 and uncertainty in the background yield. The former is estimated to be 3% as discussed in Section 6.10. The latter is used solely in a Bayesian prior pdf, not as a factor in the likelihood function, and therefore, is expected not to affect the results. It is currently set to 20%; changing this

value to any other values does not affect the limits. The systematic uncertainties used in the limit calculations are summarized in Table 6.10.

Observable	Origin	Uncertainty
Z'acc. $\times$ eff./Z^0acc. $\times$ eff.	Variation of energies. PDF uncertainties	3%
Background Yield	PDF uncertainties, N(N)LO corrections, etc	20%

Table 6.10: The systematic uncertainties on input parameters for the limits.

6.12.4 Likelihood function

We use probability density function (pdf) to model event data and to define the observable. We use the reconstructed lepton pair invariant mass as the observable and model for our data with a combination of signal and background events as:

$$f(m|\theta,\nu) = q \cdot f_{\mathrm{S}}(m|\theta,\nu) + (1-q) \cdot f_{\mathrm{B}}(m|\theta,\nu) \tag{6.3}$$

where θ is a vector of the parameter of interest and ν is a vector of the nuisance parameter, q is the probability of a signal event, f_{S} is the pdf for signal events, and f_{B} is the pdf for background events. The signal pdf for the reconstructed mass of a lepton pair is a convolution of the non-relativistic Breit-Wigner shape convoluted with a Gaussian resolution function as:

$$f_{\mathrm{S}}(m|\Gamma,\mathrm{M},\mathrm{w}) = \mathrm{BW}(\mathrm{m}|\Gamma,\mathrm{M}) \otimes \mathrm{Gauss}(\mathrm{m}|\mathrm{w}) \tag{6.4}$$

where Γ, M and w are the Breit-Wigner width, mass and the Gausssian width, repectively. The Breit-Wigner shape models the resonance width while the Gaussian describes

the detector resolution. Our benchmark models, the SSM (Z'_{SSM}) and the grand unification motivated (Z'_{ψ}) have a linear dependence of the resonance width with the resonance mass. The Z'_{SSM} model width is 3% of the mass and the Z'_{ψ} model width is 0.6%. We take the resonance width of the Z'_{ψ}, which is small and is dominated by the detector resolution. The Gaussian width, which describes the mass resolution of the dimuon pairs, is modeled as $\sigma_{\mu^+\mu^-}(m) = p_0 + p_1 m + p_2 m^2$ where p_0, p_1, p_2 are fit parameters as shown in Figure 6.8.

We use the likelihood formalism beginning with a pdf set used in Equation 6.3. The likelihood is the model computed for a particular dataset x. Assuming the events in dataset as independent, an unbinned likelihood is defined as:

$$\mathcal{L}(x|\theta,\nu) = \prod_{i=1}^{N} f(x_i|\theta,\nu) \tag{6.5}$$

where N is the number of events in the dataset, and f is the pdf shown in Equation 6.3. A dataset in our analysis contains the value of the reconstructed invariant mass of a muon pair for each selected event starting from 200 GeV and higher. In order to obtain a robust experimental result, we parameterize the signal contribution to the Poisson mean of the event yield using the ratio of the Z′ and Z cross sections (R_σ)

$$\mu_S = R_\sigma \frac{\epsilon_{Z'}}{\epsilon_Z} \mu_Z = R_\sigma R_\epsilon \mu_Z \tag{6.6}$$

where $\epsilon_{Z'}$ and ϵ_Z are the total selection efficiencies times acceptance for Z′ and Z, respectively. R_ϵ is the ratio of $\epsilon_{Z'}$ and ϵ_Z; μ_Z is the poisson mean of the number of $Z \to \mu^+\mu^-$ events and is estimated by counting the number of events in the Z peak mass region

where the background contamination is predicted to be small (0.4% by MC simulation).

We use R_σ as our parameter of interest which is expressed as:

$$R_\sigma = \frac{\sigma(pp \to \mathrm{Z}' + \mathrm{X} \to \mu^+\mu^- + \mathrm{X})}{\sigma(pp \to \mathrm{Z}' + \mathrm{X} \to \mu^+\mu^- + \mathrm{X})} = \frac{\sigma_{\mathrm{Z}'}}{\sigma_{\mathrm{Z}}}. \tag{6.7}$$

where $\sigma_{\mathrm{Z}'}$ and σ_{Z} are the Z' and the Z cross sections, respectively. Using this ratio, a number of known systematic uncertainties (e.g. the uncertainty on the integrated luminosity), as well as possible unknown systematic effects, cancel out. We model the total efficiency and acceptance for the muon pair as $\epsilon_{\mathrm{Z}'}^{\mu^+\mu^-}(m) = A + \frac{B}{(m+C)^3}$ as shown in Figure 6.3.

We choose background pdf f_B and its shape parameters by fitting to the full SM backgrounds in the mass range $200 < m < 3500$ GeV. The functional form used for the background is $e^{-am+bm^2}\, m^{-k}$. Compared to our previous analysis results, we have added the m^2 term in the fit function to describe the background prediction well across the entire range of fit. For the dimuon channel a, b, and k were determined to be 0.00229, 3.32E-8, and 3.646, respectively as shown in Figure 6.19. The background shape is normalized to the observed number of data events above 200 GeV in order to throw toys to obtain the expected limits.

We use an extended form of unbinned likelihood function for the spectrum of $\mu^+\mu^-$ invariant mass values above 200 GeV based on a sum of pdfs for the signal and background shapes as:

$$\mathcal{L}(m|R_\sigma, M, \Gamma, w, a, b, k, \mu_{\mathrm{B}}) = \frac{\mu^N e^{-\mu}}{N!} \prod_{i=1}^{N} \left(\frac{\mu_S(R_\sigma)}{\mu} f_{\mathrm{S}}(m_i|M, \Gamma, w) + \frac{\mu_{\mathrm{B}}}{\mu} f_{\mathrm{B}}(m_i|a, b, k) \right) \tag{6.8}$$

where m denotes the dataset in which the observables are the invariant mass values of the lepton pairs, m_i; N denotes the total number of events observed in the mass window the likelihood is evaluated; μ_B is the poisson mean of the total background yield; and $\mu = \mu_{\rm S} + \mu_{\rm B}$ is the mean of the Poisson distribution from which N is an observation.

6.12.5 Limits

The limits are set using the same procedure as in the 2010, 2011 and early 2012 analyses on the ratio of the production cross section times branching ratio to dimuons for Z and Z$'$ bosons. We use a Bayesian technique, using the RooStats [75] implementation of the MCMC method [76] to perform the integration. The limit calculation procedure is described in [100]. We only consider events in a window of $\pm$ 6 times the mass resolution although the lower edge of the window is adjusted for minimum of 400 events in the mass window. The normalization of the background pdf is set from the the number of observed events above 200 GeV. Log normal priors are used for the systematic uncertainties and are integrated using the Metropolis-Hastings algorithm [107]. The observed limits have been found to be robust and do not significantly change for reasonable variations of the limit setting procedure, such as varying the window of events being included in the likelihood and changes in the background normalization and shape.

Figure 6.21 shows the observed and expected upper limits on the ratio R_σ of the production cross section times branching fraction of a Z$'$ boson to that for a Z boson in our dimuon channel. The observed and expected limits agree within the uncertainties. The figure also shows the predicted cross section times branching fraction ratios for the

benchmark Z'_{SSM} [108] and Z'_{ψ} [6] models. The leading order cross section predictions for Z_{SSM} and Z'_{ψ} from PYTHIA are corrected by a mass-dependent K factor obtained using ZWPRODP [7, 77, 78], to account for the NNLO QCD contributions. The calculated Z′ cross sections include generated dileptons with masses only within ±40% of the nominal resonance mass to approximate a narrow width resonance. The NNLO prediction used for the Z/γ^* production cross section in the mass window of 60-120 GeV is 1.117 nb as calculated using FEWZ [93]. The uncertainties on cross sections for the theoretical Z′ models are not included in limit determination. For the dimuon channel, the 95% CL lower limits on the mass of a Z′ resonance are 2770 GeV for Z'_{SSM} and 2430 GeV for Z'_{ψ} . Table 6.11 below summarizes the 95% CL lower mass limits for the benchmark models considered for dimuon channel and combined (dilpeton) channel.

Model	$M_{\mu\mu}$(GeV)	M_{ll} (GeV), combined
Z'_{SSM}	2770	2960
Z'_{ψ}	2430	2600

Table 6.11: 95% CL lower mass limits for the benchmark models considered with theoretical uncertainties included. Dimuon-only limits and limits from the combined (dilepton) channels are given. The mass limit is in GeV.

6.13 Summary

We performed a search for a narrow high mass resonance decaying to opposite-sign dimuons using 20.6 fb^{-1} of the 2012 pp collision data from the LHC at $\sqrt{s} = 8$ TeV. All cross checks and systematic studies show that the detector is well understood and that the non-DY backgrounds are under control. The spectra are consistent with expectations from the SM and upper limits have been set on the cross section times branching ratio for Z′ into muon pairs relative to the SM Z boson production and decay.

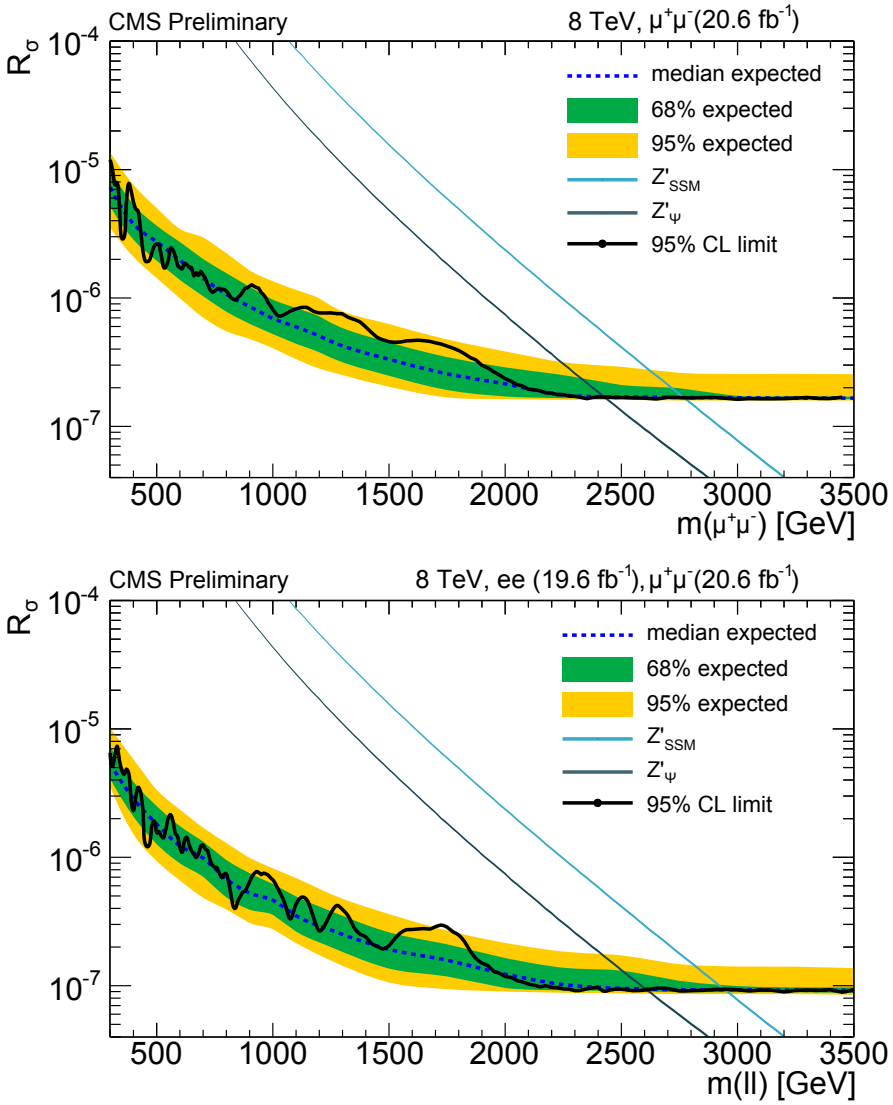

Figure 6.21: Upper limit as a function of the resonance mass M on the production ratio R_σ of cross section times branching fraction into lepton pairs for Z'_{SSM}, Z'_ψ and other production to the same quantity for Z bosons. The limits are shown for the $\mu^+\mu^-$ final state (top) and the combined dilepton result (bottom). Shaded green and yellow bands correspond to the 68% and 95% quantiles for the expected limits. The predicted cross section ratios are shown as bands with widths indicating the theoretical uncertainties.

At 95% CL, for the dimuon channel, Z'_{SSM} can be excluded below 2770 GeV and Z'_{ψ} below 2430 GeV, while for the combined (dilepton) channel, Z'_{SSM} can be excluded below 2960 GeV and Z'_{ψ} below 2600 GeV.

CHAPTER 7

TTbar MC Sample Production and Studies

As studied in the previous chapters, the largest background of our analysis is the DY production where Z/γ^* decays to a pair of leptons (e, μ, τ). Another largest background after DY is a pair of top quarks ($t\bar{t}$) production from a pp collision decaying to leptons. In our dimuon invariant mass spectrum, the high mass dimuon events from the $t\bar{t}$ samples produced by the CMS MC production team and analyzed using our selection are less than one TeV. Using the different versions of the $t\bar{t}$ samples (for e.g, leptonic, semi-leptonic etc.) in 2012, we found similar results. We were unable to see the high mass dimuon events from the $t\bar{t}$ samples produced by the CMS. Therefore, MC production of $t\bar{t}$ events was performed with the PYTHIA event generator using the method where all the channels in the decay of W boson and hadrons from $t\bar{t}$ are switched off allowing decay only to muons. We call this method "Forced Decay" because the decay was forced only to muons in the final states. The purpose of this study is to see whether or not we can generate high mass dimuon events from this method.

7.1 Introduction

The top quark is the heaviest elementary particle discovered so far. It has an electric charge of (2/3)e and 1/2 spin with a mass of 173 GeV [109]. At LHC, the top quark is produced as a single top as well as the top antitop pairs. The top quark interacts primarily by the strong interaction, but decays through the weak force. It decays almost exclusively to a W boson and a bottom quark with a branching fraction of 100%. The SM predicts its mean lifetime to be 5 $\times 10^{-25}$s, which is shorter than the time scale for strong interactions. Therefore, it does not form hadrons, which gives a unique opportunity to study a "bare" quark. All other quarks hadronize so they can only be found in hadrons. It was discovered in 1995 by the CDF and D0 experiments at FNAL.

7.2 Top quark production and decay

Because top quarks are massive, large amounts of energy are needed to create them. The only way to achieve such high energy is through high energy collisions. After the shut down of the CDF and D0 experiments at FNAL in 2011, the only accelerator that could generate a beam of sufficient energy to produce top quarks is the LHC at CERN, which already operated with a center-of-mass energy of 7 TeV and 8 TeV and produced thousands of top quarks. The LHC is an excellent tool for measuring the properties of the top quark and exploring new models which could contribute to the top physics as well as beyond SM. The LHC is a "top factory" because of its rate of top quark production due to its high energy and luminosity beam. Several processes can lead the production of a top quark, but the common one is the production of a top antitop pair through strong interactions. In a collision, a highly energetic gluon is created, which

subsequently decays into top and antitop quarks. This process is responsible for the majority of the top events at the LHC.

In hadron collisions, top quarks are produced dominantly in pairs through the QCD processes $q\bar{q} \rightarrow t\bar{t}$ and $gg \rightarrow t\bar{t}$. At the LHC, top quarks are primarily produced in pairs through the gluon fusion; at the Tevatron, top quark pairs are predominantly produced through the quark antiquark annihilation. In the process of its production, the q and $\bar{q}$ fuse into a gluon and then rematerialize as t and $\bar{t}$ quarks in opposite directions. Top quarks have a very short life time (about 10^{-24} seconds) and always decay into a W boson and b quark as $t \rightarrow W^{+}b; \bar{t} \rightarrow W^{-}\bar{b}$. The b quark evolves as jets. The W^{+} and W^{-} have several decay possibilities: $W^{\pm} \rightarrow e^{\pm}\nu_e$ (branching fraction = 1/9), $W^{\pm} \rightarrow \mu^{\pm}\nu_\mu$ (branching fraction = 1/9), $W^{\pm} \rightarrow \tau^{\pm}\nu_\tau$ (branching fraction = 1/9), $W^{\pm} \rightarrow q\bar{q}$ (branching fraction = 2/3). The q and $\bar{q}$ from W decays appear as jets. The final states containing (τ) s are difficult to isolate and were not sought in the experiments. Figure 7.1 shows the leading order Feynmann diagram for the production of top quark pairs at the LHC via gluon fusion and quark antiquark annihilation.

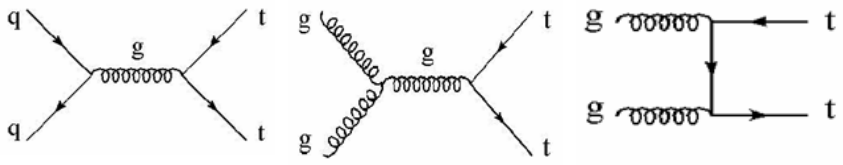

Figure 7.1: The LO Feynmann diagram for the $t\bar{t}$ production at the LHC via quark antiquark annihilation and gluon fusion.

According to the SM, top quarks exclusively decay via $t \rightarrow Wb$. The final states of $t\bar{t}$ events depend on the decay modes of the W bosons. In approximately 65% of $t\bar{t}$ events, both the W bosons decay hadronically via $W \rightarrow jj$, or at least one W decays via

$W \rightarrow \tau\nu_\tau$. The leptonic events, which account for approximately 35% of all $t\bar{t}$ events, can be subdivided into a "single lepton plus jets" and a "dilepton" sample depending on whether one or both the W bosons decay leptonically. There are three different channels through which the W boson from top quarks decay; (semi-leptonic, leptonic and hadronic), which are briefly explained below.

- Dilepton channel: both the W bosons decay into lepton (electron, muon, tau) and neutrino, $t\bar{t} \rightarrow W^+bW^-\bar{b} \rightarrow \ell\bar{\nu}_\ell b\bar{\ell}\nu_\ell\bar{b}$. The branching ratio is BR= 11.2% ($\sim$ 9/81). Considering only decays to the electrons or muons, the branching fraction is BR = 6.45% ($\sim$ 4/81).

- Lepton+ jets channel: one W boson decays into lepton and neutrino and the other into a quark antiquark pair, $t\bar{t} \rightarrow W^+bW^-b \rightarrow q\bar{q}\ b\ell\nu_{\bar{\ell}}\bar{b}$. The branching fraction is BR= 44.4% ($\sim$ 36/81).

- Hadronic channel: both the W bosons decay into a quark antiquark pair, $t\bar{t} \rightarrow W^+bW^-\bar{b} \rightarrow q\bar{q}bq\bar{q}\bar{b}$. The branching fraction is BR =44.4% ($\sim$ 36/81).

For all these three decay modes, the LO Feynmann diagram of $t\bar{t}$ events are shown in Figure 7.2. Out of these $t\bar{t}$ decay channels, the leptonic (dilepton) channel, $t\bar{t} \rightarrow (l^+\nu_l b)(l^-\bar{\nu_l}\bar{b})$, in which both the W bosons decay to charged leptons (l = e, μ, including leptonic τ decays) and neutrinos, has the smallest branching fraction, which is about 11% and has low statistics and background. Figure 7.3 shows the branching fraction of ttbar decay into several different final states.

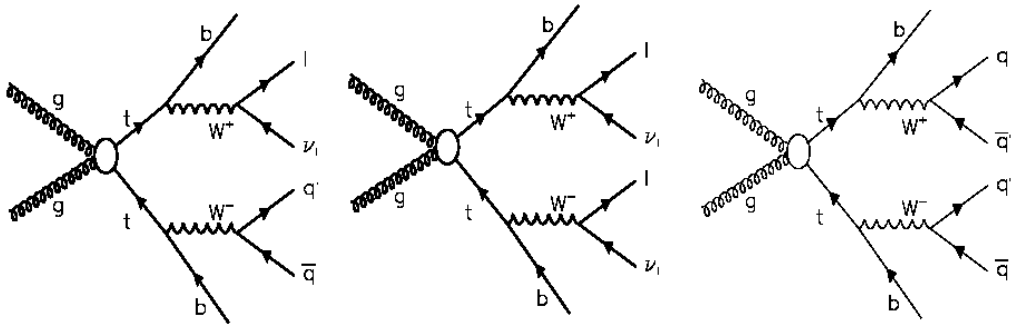

Figure 7.2: LO Feynmann diagram of ttbar decay in three different modes: semileptonic, leptonic and hadronic (from left to right).

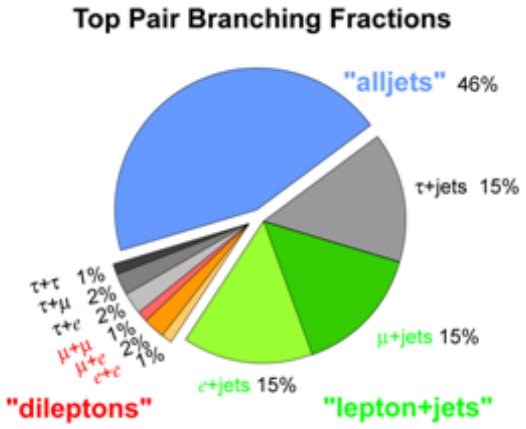

Figure 7.3: The branching ratio of the ttbar decay into several final states.

7.3 $t\bar{t}$ MC samples

The $t\bar{t}$ samples analyzed in this chapter were generated with the MADGRAPH and POWHEG event generators. Table 7.1 lists the generators, cross sections and the number of events for the various $t\bar{t}$ samples produced with the MC simulation used in this analysis; Table 7.2 lists the dataset used for the events used in Table 7.1. The V7A tags in the datasets refer to muon misalignment scenario used in the MC production. The LO, NLO and NNLO listed in the table refers to the leading order, next-to-leading-order, next-next-to-leading-order QCD corrections applied to the simulated samples. The

dataset listed in Table 7.2 are of different types. It consists of samples of events, which decay semi-leptonically and leptonically. The sample with the name MassiveBinDECAY refers to the sample where there is a massive B quark, which decay to jets; and the sample M_{tt}-7000to1000 refers to the sample where the mass of the $t\bar{t}$ is in the range of 700 to 1000 GeV. The POWHEG samples are produced at NNLO and used in our main analysis.

SN	Program	σ (pb)	Events
1	POWHEG	234 (NNLO)	21675970
2	POWHEG	234 (NNLO)	6474753
3	MADGRAPH	225 (NLO)	6923750
4	MADGRAPH	225 (NLO)	12119013
5	MADGRAPH	225 (NLO)	4246444
6	MADGRAPH	225 (NLO)	11229902
7	POWHEG	234 (NNLO)	3082812

Table 7.1: Summary of the simulated $t\bar{t}$ background samples used in this analysis. The SN indicates the dataset paths in Table 7.2 .

SN	Dataset path
1	TT_CT10_TuneZ2star_8TeV-powheg-tauola/Summer12_DR53X-PU_S10_START53_V7A-v2
2	TT_CT10_TuneZ2star_8TeV-powheg-tauola/Summer12_DR53X-PU_S10_START53_V7A-v1
3	TTJets_MassiveBinDECAY_TuneZ2star_8TeV-madgraph-tauola/Summer12_DR53X-PU_S10_START53_V7A-v1
4	TTJets_FullLeptMGDecays_8TeV-madgraph/Summer12_DR53X-PU_S10_START53_V7A-v2
5	TTJets_FullLeptMGDecays_8TeV-madgraph/Summer12_DR53X-PU_S10_START53_V7A-v1
6	TTJets_SemiLeptMGDecays_8TeV-madgraph/Summer12_DR53X-PU_S10_START53_V7A-ext-v1
7	TT_Mtt-700to1000_CT10_TuneZ2star_8TeV-powheg-tauola/Summer12_DR53X-PU_S10_START53_V7A-v1

Table 7.2: Dataset paths for the simulated $t\bar{t}$ background samples produced by the CMS MC production in the 2012 run and used in this analysis.

7.4 Dimuon invariant mass spectrum

Using the dataset in Table 7.2 and our selection, we count the number of events in the different mass bins. The number of events yielded from these samples are tabulated in Table 7.3. The numbers listed in the table indicates that the full leptonic sample gives the higher number of dimuon events after passing our selection criteria, whereas

the semi-leptonic gives the lower number, which is negligible compared to that of full leptonic version. Figure 7.4 shows the opposite-sign dimuon invariant mass spectrum for the dataset listed in Table 7.2. The shape of the spectrum are similar except for the number of events in mass bins.

Dataset	0-60	61-120	121-200	201-500	501-800	801-1000	1000-2000
Powheg-v2	1943	10316	20291	11696	255	14	2
Powheg-v1	594	3101	6001	3535	76	3	0
MassiveB-v1	538	3544	7336	4004	84	7	0
FullLeptonic-v2	10331	55766	107337	60211	1239	63	21
FullLeptonic-v1	6388	35058	67024	37662	787	43	9
SemiLeptonic-v1	15	90	27	13	0	0	0
Mtt-700to1000-v1	18	690	5638	13800	352	0	0

Table 7.3: Number of events in different mass bins for the simulated $t\bar{t}$ samples produced by the CMS for the dataset listed in Table 7.2. The masses are in GeV.

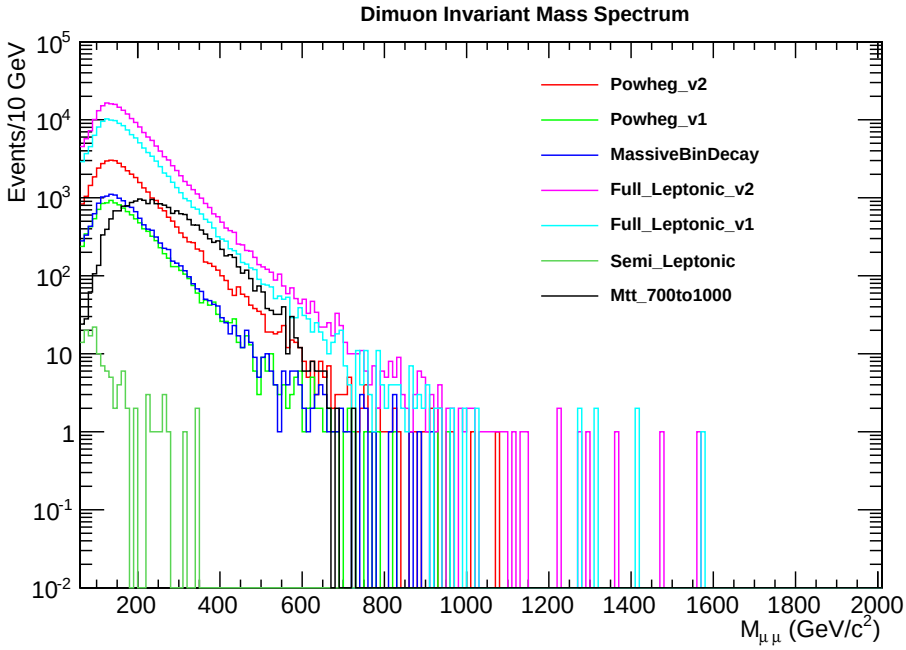

Figure 7.4: The opposite-sign dimuon invariant mass spectrum for the $t\bar{t}$ samples produced by the CMS 2012 run.

7.5 Monte Carlo production of $t\bar{t}$ sample

The Pythia program [67] is frequently used for the event generation in high energy physics focusing on multi-particle production in collisions between elementary particles. The program is intended to generate complete events in detail as experimentally observed within the limits of our current understanding of the underlying physics. The Pythia contains a wider selection of hundreds of different hard processes, which are classified in different ways. One of which is according to the number of final state objects and another according to a physics scenario. In Pythia, we generally speak of $2 \rightarrow 1$, $2 \rightarrow 2$, $2 \rightarrow 3$ processes. The more particles in the final state, the more complicated the phase space and therefore, the whole generation procedure. Infact, Pythia is optimized for $2 \rightarrow 1$ and $2 \rightarrow 2$ processes. There is no treatment for three or more particles in the final state. Another classification is according to the physics scenario, which includes hard QCD processes $qg \rightarrow qg$, W/Z production such as $e^+e^- \rightarrow \gamma^*/Z^0$ or $q\bar{q} \rightarrow W^+W^-$, heavy flavor production such as $gg \rightarrow t\bar{t}$ and $gg \rightarrow J/\psi g$, and the production of new gauge bosons, such as Z' and W'.

We use Pythia Monte Carlo version 6.4 [67] to simulate the $t\bar{t}$ sample first at the generator level. The sample is then simulated, digitized and finally reconstructed to get the output in the Analysis Object Data (AOD) format. Besides the common blocks and other common parameters used for the submission of pythia job for $t\bar{t}$ sample, few extra parameters were added in the configuration file. Those extra parameters are responsible for the forced decay of W bosons into muons only. The extra parameters and its description is explained below:

'MSEL = 6', ! top quark production

'PMAS(6,1) = 172.5', ! top quark mass

'CKIN(1) = 2000.0', ! mass cut value chosen

'24:ALLOFF', ! W decay off

'24:ONIFMATCH 13 14', ! W decay on if decay to muon and muon neutrino

The description of job options are as follows:

- MSEL = 0 lets the user defined process. We set MSEL = 6, which is the process for top quark production.
- PMAS command sets the mass of the particles produced. We set the mass of the top quark as 172.5 GeV.
- CKIN variables is used to set desired mass range of the particle produced in the process. We set 2000 GeV as a default value.
- The numbers 24 is the PDG particle code for $W^{\pm}$ boson, 13 for μ and 14 for μ_{ν}.

We have used different mass cut off variables to find out which one gives the higher numbers of dimuon events in the TeV range. We started with 500 GeV, then 1000, 1500, 2000, 2500 GeV, respectively. Using the common parameters of pythia with each of these mass cut off variables and switch on/off parameters, we have generated the MC samples with 50,000 events on each. The cross section of the MC samples generated with these mass cut off variables are tabulated in Table 7.4. As shown in the table, the cross section of the samples generated decreases with the increase of mass cut off variables.

Similar to the previous section, we have also counted the number of events in the different mass bins. The number of events yielded from these samples are tabulated

CKIN Parameter(GeV)	σ (mb)	Events
500	5.547E-10 (LO)	50000
1000	1.793E-11 (LO)	50000
1500	1.244E-12 (LO)	50000
2000	1.300E-13 (LO)	50000
2500	1.573E-14 (LO)	50000
3000	2.067E-15 (LO)	50000

Table 7.4: The cross sections of the simulated $t\bar{t}$ samples generated with different mass cut off (CKIN) parameters.

in Table 7.5. The numbers listed on the table indicates that the samples with a CKIN parameter of 2000 GeV gives the better result in TeV mass range compared to other samples with different CKIN parameters. Therefore, we have considerd 2000 GeV as a default mass cut off value and generated more samples with 50,000 events on each. In total, we have generated 10 samples with 500,000 events. Figure 7.5 shows the opposite-sign dimuon invariant mass spectrum for the dataset listed in Table 7.2 for different mass cut off values.

CKIN Parameter	0-60	61-120	121-200	201-500	501-800	801-1000	1000-2000
500	55	1002	4956	5284	131	5	0
1000	1	116	1460	10799	2274	151	35
1500	1	23	521	6898	4717	974	363
2000	3	14	224	3996	4207	1516	1256
2500	2	8	134	2200	3080	1478	2007
3000	2	6	75	1298	2117	1182	2250

Table 7.5: Number of events in different mass bins for our private simulated $t\bar{t}$ samples with different CKIN parameters. The masses are in GeV.

We also generated the dimuon invariant mass spectrum for all the datasets for the default mass cut off value (CKIN = 2000 GeV) to check whether the samples generated using the same condition is consistent to each other or not. The histogram shows that they are all consistent with each other as shown in Figure 7.6.

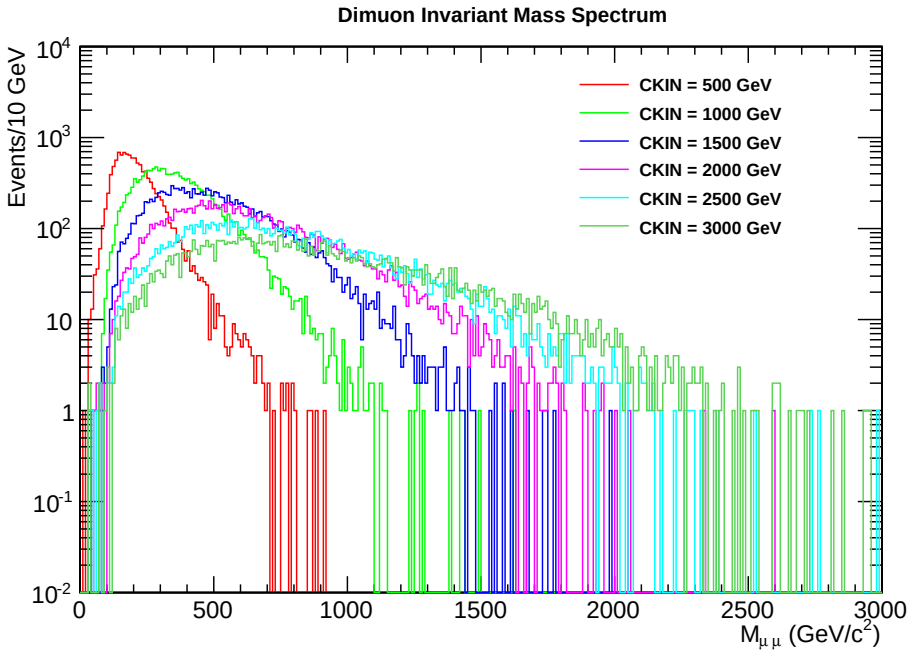

Figure 7.5: The opposite-sign dimuon invariant mass spectrum for our private $t\bar{t}$ samples for datasets with different mass cut off parameters tabulated in Table 7.5.

7.6 Dimuon mass spectrum comparison

In our search, the dominant, irreducible SM background from the DY process together with the smaller, reducible backgrounds from $t\bar{t}$ and other SM processes, predict a smoothly falling mass spectrum above the Z peak. We perform a shape analysis on the measured spectrum to find the resonance peak from new physics. The contribution on the shape of the spectrum from $t\bar{t}$ and other smaller SM backgrounds are neglisible compared to the DY backgrounds. Therefore, we consider the DY mass spectrum shape as a default shape.

As shown in Figure 7.4, we can only consider one of the dimuon invariant mass spectrum as backgrounds for our Z′ search. The dataset, which gives the genuine dimuon

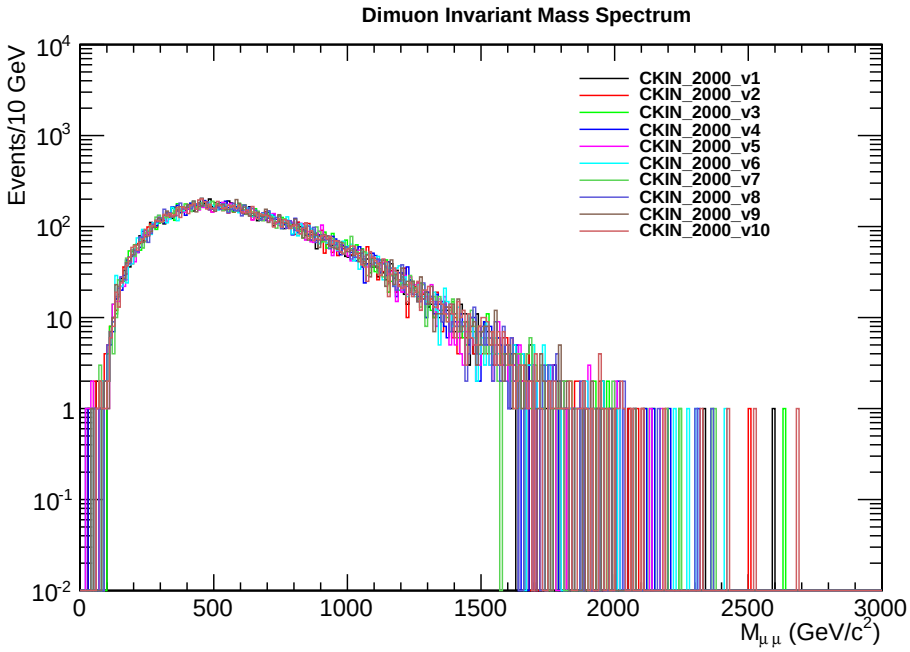

Figure 7.6: The opposite-sign dimuon invariant mass spectrum for our private $t\bar{t}$ samples for the datasets with default mass cut off value, CKIN= 2000 GeV, tabulated in Table 7.5.

mass spectrum with the higher yield are full leptonic and POWHEG samples as listed in Table 7.2. The contribution from the semi-leptonic, MassiveBinDecay, and M_{tt}-700to1000 samples is poor so they can be ignored. Our recent analysis note [97] uses POWHEG version 2 sample as default. However, we can replace the existing $t\bar{t}$ dimuon mass spectrum by the one from the full leptonic version 2 sample, which yields a higher number of high mass events. The dimuon invariant mass spectrum obtained from the CMS MC samples (POWHEG and full leptonic) were compared. Figure 7.7 shows the comparison of dimuon mass spectrum for these samples produced by the CMS. There are two versions v1 and v2 samples each of which are produced under similar conditions and differ only with the number of events. The shape of the dimuon mass spectrum from

these samples are similar and smoothly falling, following the shape of the DY background as in our dimuon mass spectrum.

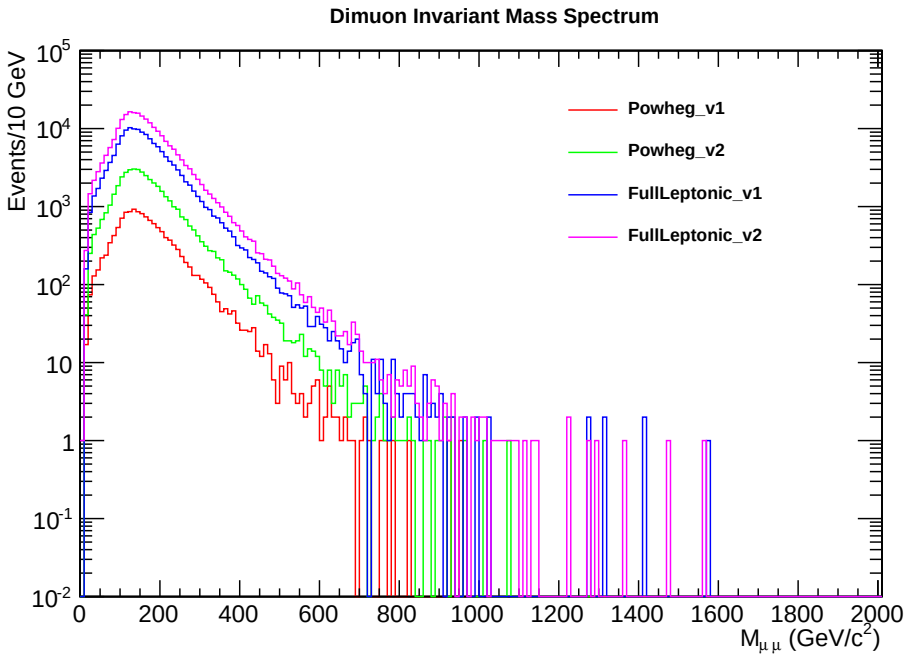

Figure 7.7: Comparison of opposite-sign dimuon invariant mass spectrum for POWHEG and full leptonic versions of $t\bar{t}$ samples produced by the CMS MC team as listed in Table 7.5.

The dimuon invariant mass spectrum obtained with the CMS MC samples and our forced decay samples were also compared. The shape of the dimuon mass spectrum from the CMS samples are smoothly falling in similar shape as the DY. The spectrum from our sample with CKIN value 2000 GeV is wider, flat, and is completely overlapping the spectrum from the DY samples; although it has generated high mass dimuon events. However, the samples with the CKIN value of 500 GeV follow exactly the similar pattern of the CMS samples. Therefore, it seems impossible to replace the dimuon mass spectrum of the $t\bar{t}$ samples with the dimuon mass spectrum from our forced decay samples. Figure

7.8 shows the comparison between the dimuon invariant mass spectrum of the CMS samples with our private forced decay samples.

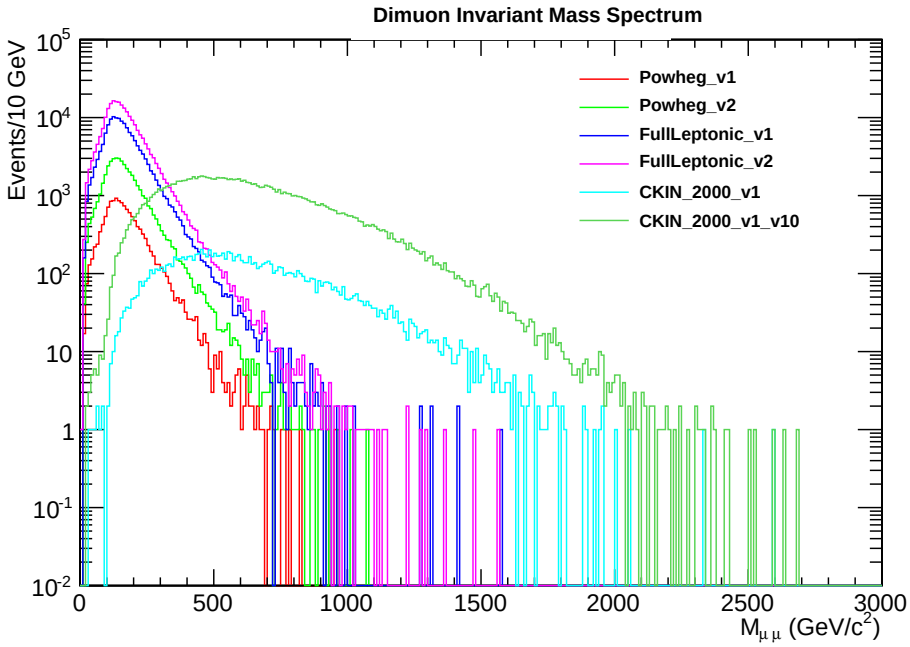

Figure 7.8: Comparison of opposite-sign dimuon invariant mass spectrum of the CMS MC samples and our private $t\bar{t}$ samples.

7.7 Summary

We performed the analysis of the $t\bar{t}$ samples generated by the CMS MC production team for the 2012 run listed in Table 7.2. The shape of the dimuon invariant mass spectrum generated are similar except for the semi-leptonic and Mtt-700to1000 samples. The full leptonic samples generated with the MADGRAPH event generator, yielded higher number of dimuon events. The samples generated with the POWHEG event generator has similar dimuon mass spectrum shape, but a lower yield compared to the full leptonic samples. Our collaboration has considered the POWHEG version 2

(with higher events) samples as a default for our anaylsis as the QCD correction applied to these samples is NNLO. To find the high mass dimuon events, MC samples with the PYTHIA event generator using the force decay method were also generated where W was forced to decay only into muons in final states. It has been found that the samples generated with the CKIN value of 2000 GeV produces a better estimate of the high mass dimuon events in TeV scale. It concludes that the force decay method applied works well. However, the shape of the spectrum is different compared to the CMS MC samples which is wider and seems overlapping with the DY invariant mass spectrum in the high mass regions. Therefore, we are unable to use these samples in our analysis for resonance search as a background.

CHAPTER 8

Conclusion

The SM of particle physics is a theoretical framework, which explains most of the phenomena occurring in the nature. However, there are several experimental evidence that require new theoretical models. Many extensions of the SM have been evolved to explain such experimental observations. The LHC has been designed to explore the SM physics as well as the new physics beyond the SM. It started to work in 2009 by colliding proton beams at center-of-mass energy of 0.9 TeV and then at 2.36 TeV with the excellent performance of the machine and its detectors. After the success of its performance, it continued its operation and reached center-of-mass energy of 7 TeV in 2010, the highest energy achieved by a particle in any particle collider and marked the start of the new era of research in experimental high energy physics.

The basic strategy of the Muon Endcap Alignment system is to reconstruct DCOPS and CSC positions for all SLMs for all Muon Endcaps at B= 0T and 3.8 T using COCOA (CMS Object-oriented Code for Optical Alignment), validate the reconstructed results for all SLMs against photogrammetry (PG) measurements and finally quantify discrepancies and residuals. The detector geometry at B =3.8T is provided in the form of alignment constant for reprocessing 2010 data. For the first time, we provided alignment constant in rϕ plane to CMS for the track reconstruction of the pp collision for the 2010 STARTUP. We also validated ME-2.-3,-4 results with the track-based (Beam

Halo) data for the accuracy of the alignment procedure. The inclinometer results from Magent Test and Cosmic Challenge (MTCC, Aug 2006) and Cosmic Ray at Four Tesla (CRAFT, Oct 2008) are also studied for comparison; the results are consistent with each other.

The Muon Endcap Alignment system has successfully recorded data during the year 2010. For the CSCs, all monitored chambers are aligned in X_{CMS},Y_{CMS}. An aligned detector geometry at B = 3.8 T is provided in the form of alignment constants which can be used for muon track reconstruction. The resolution for all ME+2,3,4 in rϕ is 168 μm and 143 μm for all ME-2,-3,-4. The systematic error associated with the reconstruction is estimated to be 116 μm for ME+2,3,4 and 149 μm for ME-2,-3,-4 from a comparison with PG. The alignment constants for the 2010 STARTUP is provided in SQlite database and is available at the CERN Analysis Facility (CAF).

The CMS detector at the LHC collected data at 7 TeV, which corresponds to an integrated luminosity of 40 pb^{-1} during 2010 and 5.28 fb^{-1} during 2011. The 2011 run had 100 times more data than in 2010 with the same center-of-mass energy of 7 TeV for the physics analyses. During the LHC 2012 run, the energy of the collision was increased to 8 TeV and the CMS collected 20.6 fb^{-1} of data. In this dissertation, we have performed the search for new, heavy, neutral gauge bosons, Z$'$, with SM like couplings using the LHC data of the 2011 and 2012 runs collected with the CMS detector. The discovery of such new gauge bosons is one among the potential discoveries expected at the LHC. The Z$'$ boson is expected to appear as a resonance in the high mass region of the DY process.

Assuming the SSM as a benchmark model, a search for $Z' \to \mu^+\mu^-$ is performed

with the LHC data of 2010 run corresponding to an integrated luminosity of 40 pb^{-1} and did not reveal any excess of observed events above the SM background predictions. Therefore, upper limit on the Z' production cross section was set as a function of Z' mass. We excluded Z' mass less than 1027 GeV/c^2 at 95% CL [58]. We also performed this search with the LHC data of 2011 run corresponding to an integrated luminosity of 5.28 fb^{-1} assuming the SSM and E6 models as benchmarks. Again, we found no excess of events above the SM background predictions. Therefore, we set upper limit on the $Z' \to \mu^+\mu^-$ production cross section as a function of Z' mass. We excluded Z'_{SSM} and E6 model Z'_{ψ} below masses 2.15 TeV and 1.82 TeV, respectively, at 95% CL. In 2012, we performed this search with the LHC data of 2012 run at center-of-mass energy of 8 TeV with four times more data than in the 2011 run, corresponding to the integrated luminosity of 20.6 fb^{-1}. The studies performed for this 2012 data also did not reveal any excess of observed events in the data above the SM background expectations. We again set the limit on $Z' \to \mu^+\mu^-$ production cross section as a function of Z' mass. We excluded the SSM resonance Z'_{SSM} and E6 model resonance Z'_{ψ} below masses 2.77 TeV and 2.43 TeV, respectively, at 95% CL. Search with more data will enable us to either find potential excess of events above the SM background expectations or to set more stringent limits on the Z' mass. The most stringent limits on SSM resonance Z'_{SSM} at 8 TeV in the dimuon decay channel is 2.77 TeV, combined dilepton (dimuon+ dielectron) channel is 2.96 TeV and E6 model resonance is 2.6 TeV.

In summary, searches for the dimuon resonance were performed at 40 pb^{-1} and 5.28 fb^{-1} at 7 TeV and 20.6 fb^{-1} of integrated luminosity at 8 TeV from the LHC. In all the searches, no evidence of events above the expected SM sources was seen. Limits

were set on the production cross section times branching ratio of a high mass particle decaying to $\mu\mu$. This study covered the first three years of the LHC run during which the instantaneous luminosity increased by more than double recorded at Tevatron. The improvement of this analysis could be possible when more data is available in the future as the limits become stronger and higher mass ranges will become accessible. Further potential improvements could come from more advanced statistical techniques, better understanding of the detector, or improved event selection. The proposed increase in collision energy of 13 TeV that will start in 2015 will provide another avenue for improving the results presented in this analysis. Any collider experiments in the future with higher energies and better resolution could reveal the existance of the heavy neutral gauge boson, Z'.

Finally, we highlight once more the main accomplishments presented in this dissertation:

- As one of the responsibles for the Muon Endcap Alignment system of CMS, I have successfully analyzed the alignment data from the 2008, 2009, and 2010 LHC cosmic runs and delivered corresponding alignment constants to the CMS collaboration. The results are published in the Journal of Instrumentation (JINST).

- I have provided alignment constants in the rϕ plane to CMS for muon track reconstruction for the 2010 LHC Startup. The result is available in the CMS Analysis Facility (CAF). It was the first time, such data were provided to CMS.

- I have successfully analyzed the collision data of 2010, 2011 and 2012 LHC runs and presented to the CMS collaboration.

- We have performed a first search for a Z' boson with the LHC data of 2010 run at center-of-mass energy of 7 TeV corresponding to an integrated luminosity of 40 pb^{-1} using the SSM as a benchmark. We set the limit on Z' mass at 95% CL. For the dimuon channel, we excluded Z' mass below 1.027 TeV/c^2, which is comparable to the previous limit 1.071 TeV/c^2 set by CDF experiment at FNAL corresponding to an integrated luminosity of 4.6 fb^{-1}.

- We have continued the search with the LHC data of 2011 run at center-of-mass energy of 7 TeV corresponding to an integrated luminosity of 5.28 fb^{-1} assuming the SSM and E6 models as benchmarks. We again set limit on Z' mass at 95% CL. For the dimuon channel, we excluded Z'_{SSM} and Z'_{ψ} masses below 2.15 TeV and 1.82 TeV, while in the combined (dilepton) channel, they are excluded below 2.3 TeV and 2.0 TeV, respectively. Our results are comparable to the ATLAS results, which excluded Z'_{SSM} mass below 1.99 TeV in the dimuon channel and 2.22 TeV in the combined (dilepton) channel.

- We have continued the search with the LHC data of 2012 run at center-of-mass energy of 8 TeV corresponding to an integrated luminosity of 20.6 fb^{-1} using the SSM and E6 models as benchmarks. We again set the limit on Z' mass at 95% CL. For the dimuon channel, we excluded Z'_{SSM} and Z'_{ψ} masses below 2.77 TeV and 2.43 TeV, while in the combined (dilepton) channel, they are excluded below 2.96 TeV and 2.6 TeV, respectively. Our results are comparable to the ATLAS results, which excluded Z'_{SSM} mass below 2.53 TeV in the dimuon channel and 2.9 TeV in the combined (dilepton) channel.

References

[1] M. Cvetic and S. Godfrey, "Discovery and identifcation of extra gauge bosons", hep-ph/9504216v1, 1995.

[2] David J. Griffiths, " Introduction to Elementary Particles", Harper and Row Publisher Inc., 1987.

[3] D. H. Perkins, "Introduction to High Energy Physics", 4th edition, Cambridge University Press, 2000.

[4] F. Halzen and A. D. Martin, "Quark and Leptons: an Introductory Course in Modern Particle Physics", John Wiley and Sons Inc., 1984.

[5] P. Langacker, "The physics of heavy Z′ gauge bosons", Rev. Mod. Phys, volume 81(2009), 1199.

[6] A. Leike, "The phenomenology of extra neutral gauge bosons", Phys. Rept, volume 317 (1999), 143.

[7] E. Accomando et.al, "Z′ physics with early LHC data", Phys. Rev., volume D 83 075012, 2011.

[8] Universitat Hamburg, "Schmidt Group Research Activities", `http://www.emmynoethercms.uni-hamburg.de/en/Research.html`.

[9] T. Y. Wu and W. Y. Pauchy Hwang, "Relativistic quantum mechanics and quantum fields", World Scientific, 1991.

[10] S. L. Glashow, "Partial symmetries of weak interactions", Nucl. Phys., volume 22 (1961), 579-588.

[11] S. Weinberg, "A model of leptons", Phys. Rev. Lett., volume 19 (1967), 1264-1266.

[12] A. Salam, "Weak and Electromagnetic Interactions, Elementary Particle Theory", Proceedings of the Nobel Symposium at Lerum, Sweden, volume C680519 (1968), 367-377.

[13] J. L. Hewett and T. G. Rizzo, "Low Energy Phenomenology of Superstring Inspired E(6) Models", Phys. Rept., volume 183 (1989), 193.

[14] P. Langacker, "Grand unified theories and proton decay", Phys. Rept., 72 (1981).

[15] P. Langacker, "The Physics of heavy Z′ gauge bosons", Rev. Mod. Phys., volume 81 (2009), 1199.

[16] M. Cvetic et.al, "Electroweak Symmetry Breaking and New Physics at the TeV scale", World Scientific, 1995, 383.

[17] R. W. Robinett and J. L. Rosner, "Mass scales in grand unified theories", Phys. Rev., volume D 26 (1982), 2396.

[18] P. Langacker, "Bounds on mixing between light and heavy gauge bosons", Phys. Rev., volume D 30 (1984), 2008.

[19] ATLAS Collaboration, " Search for high mass dilepton resonances in pp collisions at $\sqrt{s} = 7$ TeV with the ATLAS experiment", Phys. Lett., volume B700 (2011), 163.

[20] CMS Collaboration, " Search for Resonances in the Dilepton Mass Distribution in pp Collisions at $\sqrt{s} = 7$ TeV, JHEP, volume 5 (2011), 93.

[21] CDF Collaboration, " Search for High Mass Resonances decaying to Muon Pairs in $\sqrt{s} = 1.96$ TeV $p\bar{p}$ Collisions", Phys. Rev. Lett., volume 106 (2011).

[22] D0 Collaboration, " Search for heavy neutral gauge boson in the dielectron channel with 5.4 fb^{-1} of $p\bar{p}$ collisions at $\sqrt{s} = 1.96$ TeV", Phys. Lett., volume B695 (2011), 88-94.

[23] C. Hays et al., " New Techniques in the Search for Z′ Bosons and Other Neutral Resonances", Mod. Phys. Lett., volume A24 (2009), 2387.

[24] L. Evans and P. Bryant, " LHC machine", JINST, volume 03 (2008), S08001.

[25] CERN Public results, "The LHC accelerator complex", `http://public.web.cern.ch/public/en/research/AccelComplex-en.html`.

[26] ATLAS Collaboration, " The ATLAS experiment at the CERN LHC", JINST, volume 03 (2008), S08003.

[27] CMS Collaboration, " The CMS experiment at the CERN LHC", JINST, volume 04 (2008), S08004.

[28] LHCB Collaboration, " The LHCB experiment at the CERN LHC", JINST, volume 05 (2008), S08005.

[29] ALICE Collaboration, " The ALICE experiment at the CERN LHC", JINST, volume 02 (2008), S08002.

[30] TOTEM Collaboration, " The TOTEM experiment at the CERN LHC", JINST, volume 07 (2008), S08007.

[31] LHCF Collaboration, " The LHCF experiment at the CERN LHC", JINST, volume 06 (2008), S08006.

[32] CMS Public Website, " First high energy collisions at 7 TeV", http://cms.cern.ch/CMSLinks/Photoes/Physicsevents/Realevents.

[33] CERN Twiki, "Lumi Public Results", http://twiki.cern.ch/twiki/bin/view/CMSPublic/LumiPublicResults.

[34] The CMS Collaboration, "CMS Physics Technical Design Report ", Volume I, Detector Performance and Software, CMS TDR, CERN/LHCC 2006 001.

[35] Srivastava et.al, "Silicon detector research at DESY", http://www.iexp.desy.de/users/srivastava/RESEARCH-INTEREST.htm.

[36] Wikimedia Commons, "Transverse Slice of CMS", http://commons.wikimedia.org/wiki/CMSSlice.

[37] The CMS Collaboration, "The Tracker Project Technical Design Report", CERN/LHCC 98-006, CMS TDR 5, April 1998.

[38] The CMS Collaboration, "Addendum to the CMS Tracker TDR", CERN/LHCC 2000-016, CMS TDR 5 Addendum 1, April 2000.

[39] R. Bellan, "Muon Reconstruction with the CMS Detector", http://oldsite.to.infn.it/activities/schedules/congr2008/Bellancms.pdf.

[40] The CMS Collaboration, "The CMS Electromagnetic Calorimeter Project: Technical Design Report", CERN, CMS-TDR-004, 1997.

[41] The CMS Collaboration, "The CMS Hadron Calorimeter Project: Technical Design Report", CERN, CMS-TDR-002, 1997.

[42] The CMS Collaboration, "The Magnet Project: Technical Design Report", CERN/LHCC 97-010 (1997). CMS TDR 1.

[43] The CMS Collaboration, "The Muon Project: Technical Design Report", CERN/LHCC 97-32 (1997). CMS TDR 3.

[44] CMS Collaboration, "Performance of the CMS Drift Tube Chambers with Cosmic Rays", JINST 5 (2010) T03015.

[45] CMS Public Website, `http://cms.web.cern.ch/news/muondrifttubes`.

[46] CMS Collaboration, "Efficiency of finding muon track trigger primitives in CMS cathode strip chambers", Nuclear Instruments and Methods in Physics Research Section A, volume 592 (2008), 2637.

[47] The CMS Collaboration, "Performance of CMS Muon Reconstruction in Cosmic-Ray Events", JINST 5 (2010) T03022.

[48] The CMS Collaboration, "The TriDAS project, technical design report, Volume 1, The level-1 trigger", CERN/LHCC 2000-038, (2000).

[49] The CMS Collaboration, "The TriDAS project, technical design report", Volume 2, Data acquisition and high-level trigger technical design report, CERN/LHCC 2002-026, (2002).

[50] The CMS Collaboration, "Aligning the CMS muon chambers with the muon alignment system during an extended cosmic ray run", J. Inst, 2010, T03019.

[51] M. Hohlmann et.al, " Design and Performance of the Alignment System for the CMS Muon Endcaps", Proc. of IEEE Nucl. Sci. Symp. 2006, San Diego, `http://cdsweb.cern.ch/record/1110519`, CR (2008) 016.

[52] M. Hohlmann et.al, " Aligning the CMS Muon Endcap Detector with a System of Optical Sensors", Proc. of IEEE Nucl. Sci. Symp. 2007, Honolulu, `http://cdsweb.cern.ch/record/1110518`, CR (2008) 015.

[53] B. G. Bylsma et.al, "The Cathode Strip Chamber Data Acquisition System for CMS", The Ohio State University, Columbus, OH, USA.

[54] A. Behrens et al., " CMS Yoke Endcaps position after closure", Survey Report, EDMS 1 062 665, CMS SG UR 0160.

[55] CERN Analysis Facility (CAF), `http://afs/cern.ch/cms/CAF/HWAlignment/AlignmentDB/DB20100629/CSC-HWgeometry-Oct-13-2010-final.xml`.

[56] I. Belotelov et.al, "Simulation of Misalignment Scenarios for CMS Tracking Devices", CMS Note 2006-008.

[57] I. Belotelov et.al , "Influence of Misalignment Scenarios on Muon Reconstruction", CMS Note 2006-017.

[58] D. Acosta et al., "Search for high mass resonances decaying to muon pairs with 40 pb^{-1} of collisions gathered at $\sqrt{s} = 7$ TeV", CMS AN-2010-317.

[59] J. Hegeman et al., "Luminosity Method Based on Pixel Cluster Counting", CMS AN-12-056.

[60] G. Alverson et.al, "Search for High Mass Resonances Decaying to Muon Pairs with Collisions Gathered at $\sqrt{s} = 7$ TeV", CMS AN-2011-278.

[61] Muon POG, "Performance of muon identification in 2010 data", CMS PAS, MUO-10-004.

[62] R. E. Kalman, "Kalman filter for vertex fitting", `http://twiki.cern.ch/twiki/bin/view/CMSPublic/SWGuideKalmanVertexFitter`.

[63] F. Maltoni et al., "MadEvent: Automatic event generation with MadGraph", JHEP, volume 02 (2003), 027.

[64] S. Alioli et al., "NLO vector boson production matched with shower in POWHEG", JHEP, volume 07 (2008), 060.

[65] P. Nason, "A new method for combining NLO QCD with shower Monte Carlo algorithms", JHEP, volume 11 (2004), 040.

[66] S. Frixione et al., "Matching NLO QCD computations with Parton Shower simulations, the POWHEG method", JHEP, volume 11 (2007), 070.

[67] T. Sjostrand et al., "PYTHIA 6.4 physics and manual" , JHEP, volume 05 (2006), 026.

[68] J. Pumplin et al., "New generation of parton distributions with uncertainties from global QCD analysis", JHEP, volume 07 (2002), 012.

[69] H. L. Lai et al., "New parton distributions for collider physics", Phys. Rev., volume D 82 (2010), 074024.

[70] GEANT4 Collaboration, "GEANT4, a simulation toolkit", Nucl. Instrum. Meth. A 506(2003).

[71] D. Bandurin et al., "Study of backgrounds to high mass dielectron (Drell-Yan) final states", CMS AN-2008-044.

[72] J. Alcaraz Maestre et al., "Updated Measurements of the Inclusive W and Z Cross Sections at 7 TeV", CMS AN-2010-264 (2010).

[73] G. Alverson et.al , "Search for High-Mass Resonances Decaying to Muon Pairs with Collisions gathered at $\sqrt{s} = 7$ TeV", CMS AN-2011-472 (2012).

[74] B. Clerbaux et al., "Statistical analysis of a resonant signal search in multiple final state modes", CMS AN-2010-312 (2010).

[75] L. Moneta et al., "The RooStats project", arXiv:1009.1003v1.

[76] B. Berg, "Markov Chain Monte Carlo Simulations and their Statistical Analysis", World Scientific (2004).

[77] R. Hamberg et.al, "A complete calculation of the order ${\alpha_S}^2$ correction to the Drell-Yan K-factor", Nucl. Phys., volume B 359 (1991), 343.

[78] W. L. van Neerven et.al, "The O(${\alpha_S}^2$) corrected Drell-Yan K-factor in the DIS and MS schemes", Nucl. Phys., volume B 382 (1992), 11.

[79] CMS Twiki, " CMS Physics Results", `http://twiki.cern.ch/twiki/bin/view/CMSPublic/PhysicsResults/EXO-11-019`.

[80] CMS Twiki, "Physics Data and Monte Carlo Validation for 2012 Analysis", http://twiki.cern.ch/twiki/bin/viewauth/CMS/PdmV2012Analysis.

[81] M. Grothe et.al , "CMS Luminosity Based on Pixel Cluster Counting, Summer 2013 Update", CMS PAS, LUM-13-001(2013).

[82] CMS Twiki, "Luminosity Physics Object Group", http://twiki.cern.ch/twiki/bin/view/CMS/TWikiLUM.

[83] CMS Twiki, "Muon Tag and Probe for the Higgs Analysis", http://twiki.cern.ch/twiki/bin/viewauth/CMS/TagAndProbeForHIG.

[84] E. Martino, "Single Muon Trigger Efficiencies", http://indico.cern.ch/getFile.py/access?contribId=2&resId=0&materialId=slides&confId=228197.

[85] CMS Collaboration, "Search for Narrow Resonances in Dilepton Mass Spectra in pp collisions at $\sqrt{s} = 7$ TeV", Phys. Lett., volume B 714 (2012), 158.

[86] CMS Collaboration, "Search for Heavy Narrow Dilepton Resonances in pp collisions at $\sqrt{s} = 7$ TeV and $= 8$ TeV", Phys. Lett., volume B 720 (2012), 63.

[87] G. Alverson et al., "Search for High Mass Resonances Decaying to Muon Pairs at $\sqrt{s} = 8$ TeV", CMS AN-2012-182.

[88] P. Traczyk, "Muon Object Review for Moriond 2013", http://indico.cern.ch/conferenceDisplay.py?confId=172473.

[89] CMS Twiki, " Muon Reference Efficiencies", http://twiki.cern.ch/twiki/pub/CMS/MuonReferenceEffs/muoneff/NewHighPt/Run/2012ABCD.

[90] E. Martino, "Muon ID and Reconstruction Efficiencies", http://indico.cern.ch/getFile.py/access?contribId=2&resId=0&materialId=slides&confId=233592.

[91] CMS Collaboration, "Performance of CMS Muon Reconstruction in pp Collision Events at $\sqrt{s} = 7$ TeV", JINST, volume 7 (2012)

[92] G. Abbiendi et al., "Muon Reconstruction in the CMS Detector", CMS AN 2008-097, 813 (2008).

[93] R. Gavin et al., "FEWZ 2.0, A code for hadronic Z production at next-next-to-leading order", Comp. Phys. Comm. 182 (2011), 11, 2388.

[94] CMS Twiki, " HEEP Electron ID and Isolation", http://twiki.cern.ch/twiki/bin/viewauth/CMS/HEEPElectronID.

[95] S. Baffioni et al., "Electron Identification in CMS", CMS AN 2009-178.

[96] N. Kidonakis, "Differential and total cross sections for top pair and single top production", arXiv:1205.3453.

[97] G. Alverson et al., "Search for High-Mass Resonances Decaying to Muon Pairs in pp Collisions at $\sqrt{s} = 8$ TeV", CMS AN-2012-422.

[98] CMS Collaboration, "Measurement of Inclusive W and Z Boson Cross Sections at $\sqrt{s} = 8$ TeV", CMS PAS, SMP-12-011, (2012).

[99] A. Apyan et al., "Measurements of Inclusive W and Z Boson Cross Section in pp Collisions at $\sqrt{s} = 8$ TeV", CMS AN-2012-67.

[100] S. Schmitz et al., "Statistical Inference in a Search for a Narrow Resonance", CMS AN-2012-185.

[101] M. Botje et al.,"The PDF4LHCWorking Group Interim Recommendations", (2011). arXiv:1101.0538.

[102] A. Martin et al. , "Parton distributions for the LHC", Eur. Phys. J. C 63 (2009), 189.

[103] H. L. Lai et al., "New parton distributions for collider physics", Phys. Rev., voulme D 82 (2010), 074024.

[104] R. D. Ball et al., "A first unbiased global NLO determination of parton distributions and their uncertainties", Nucl. Phys. B838 (2010), 136.

[105] D. Bourilkov et al., "PDF Uncertainties for Z′ searches at 8 TeV", CMS AN-2012-348.

[106] M. Brodsky et al., "Search for large extra dimensions in dimuon events in pp collisions at $\sqrt{s} = 8$ TeV", CMS AN-2012-496.

[107] W. Hastings, "Monte Carlo sampling methods using Markov chains and their applications", Biometrika 57 (1970) 9709.

[108] G. Altarelli et al., "Searching for new heavy vector bosons in pp colliders", Z. Phys. C 45 (1989), 109.

[109] J. Beringer et al., "PDGLive Particle Summary ". Particle Data Group. Retrieved 2013-07-23.